Manufacturing Methods for Magnetic Resonance Microscopy Tools with Application to Neuroscience

KIT
Karlsruher Institut für Technologie

M.Sc. Robert Kamberger

Fakultät für Maschinenbau
Karlsruher Institut für Technologie

Genehmigte **Dissertation**
zur Erlangung des akademischen Grades
Doktor der Ingenieurswissenschaften

Autor	Robert Kamberger
Adresse	Karlsruhe Institut für Technologie
	Institut für Mikrostrukturtechnik
	Hermann-von-Helmholtzplatz 1
	76344 Eggenstein-Leopoldshafen

Hauptreferent	Prof. Dr. Jan G. Korvink
	Institut für Mikrostrukturtechnik,
	Karlsruhe Institut für Technologie
Korreferent	Prof. Dr. Dr. h.c. Jürgen Hennig
	Klinik für Radiologie - Medizin Physik
	Universitätsklinikum Freiburg
Prüfungsvorsitzender	Prof. Dr. Volker Schulze
	Institut für Fertigungs- und Werkstofftechnik
	Karlsruhe Institut für Technologie
Datum der Disputation	4. April 2017

Zusammenfassung

Magnetresonanztomographie (MR) ist ein unverzichtbares nicht-invases und hochselektives bildgebendes Verfahren in der Medizin. MR Tomographie wird kommerziell in der klinischen Diagnostik und der Forschung für Gehirnkrankheit, z.B. Epilepsie, Alzheimer und Parkinson, angewandt. In den Neurowissenschaften haben sich Kleintiere als biologische Modelle für die grundlegenden Studien zur diesen Gehirnkrankheiten etabliert. MR Methoden sind ein wertvolles Werkzeug um die Morphologie und den Metabolismus von Kleintieren zu untersuchen. Die Modelle für die Untersuchung von Gehirnkrankheiten schließen Zellen/Zellkulturen und organotypische hippocampale Schnittkulturen (OHSC) mit ein. Obwohl die MR Mikroskopie für die Untersuchung von OHSC schon angewandt wurde fehlt eine effektive Plattform für umfangreiche longitudinale Studien an OHSC wie sie in den Neurowissenschaften üblich sind.

Zwei Detektorkonzepte für die MR Mikroskopie inklusive ihrer Auslegung, der Herstellung und der Charakterisierung, werden in dieser Arbeit beschrieben. Beide Konzepte basieren auf Herstellungsmethoden welche hohe Fertigungsgenauigkeiten zulassen und in ihrem Herstellungsvolumen skalierbar sind. Hohle solenoide Mikrospulen welche für hochauflösende Untersuchung von Zell und Zellanhäufungen geeignet sind werden eingeführt. Die Herstellung basiert auf dem automatisierten wickeln von Mikrospulen, eine skalierbare und hochpräzise Fertigungsmethode der Mikrotechnologie. Zudem werde induktiv gekoppelte Oberflächenspulen eingeführt. Diese Oberflächenspulen fokussieren den magnetischen Fluss und werden deshalb Lenz Linsen genannt. Die Lenz Linsen werden mit kabelgebundenen und induktiv gekoppelten Spulen verglichen. Ihre Breitband-Fähigkeit machen sie zu einem idealen Kandidaten für die Nutzung in verschiedensten MR Tomographie Systemen.

Die Lenz Linsen wurden für den Einsatz in einer MR kompatiblen Inkubationsplattform ausgelegt, welche in dieser Arbeit entwickelt wurde. Der MR Inkubator erweitert die Funktionalität eines MR Tomographen um neurologische Gewebe (z.B. OHSC) über mehrere Stunden andauernde MR Messungen am Leben zu erhalten. Der MR Inkubator erlaubt longitudinale Studien an OHSC und bietet damit eine Plattform für umfangreiche Studien in den Neurowissenschaften.

Die Lenz Linsen wurden zusammen mit dem MR Inkubator für MR Mikroskopie Messung von akuten/fixierten hippocampalen Schnitten und OHSC genutzt. Die Resultate dieser MR Mikoskopie Messungen zeigen dass in OHSC die grobe Zytoarchitektur sichtbar ist, ohne dass die OHSC während der Messungen sterben. Somit ist das eingeführte System bereit für longitudinale Studien an OHSC, welche bereits für die Aufklärung der Epilepsieprogression begonnen wurden.

Abstract

Magnetic Resonance (MR) is an indispensable non-invasive and highly selective medical imaging technique. MR imaging is commercially used for clinical diagnostics and research on brain diseases such as epilepsy, Alzheimer's and Parkinson's disease. In fundamental neuroscience small animals are established as biological models for gaining a detailed understanding of these diseases. MR is a valuable tool to study morphology and metabolism of small animals, but suffers from low resolution. The models for studying brain diseases include cells/cell clusters and organotypic hippocampal slice cultures (OHSC). Although MR microscopy was used to study OHSC, an effective screening platform for voluminous longitudinal studies of OHSC is missing.

Two MR microscopy detector concepts, their design, manufacturing and characterisation, are described in this thesis. Both concepts are based on manufacturing methods that allow high accuracy and are scalable in manufacturing volume. Hollow solenoidal micro coils that can be used for high-resolution cell and cell cluster studies are introduced. The manufacturing is based on wire winding micro coils, a scalable and high precision micro manufacturing method. Additionally, inductively coupled magnetic field focussing surface coils, termed Lenz lenses are introduced. The Lenz lenses are compared to wired and inductively coupled coils. Their broadband capability make them an ideal candidate to be used in different MR scanners.

The Lenz lenses were designed to fit into an MR compatible incubation platform developed in this thesis. The MR incubator is designed to expand the MR scanner with the capability to maintain neurological tissue (i.e. OHSC) viable throughout long MR scan times of several hours. The MR incubator allows longitudinal studies of OHSC, therefore offering a screening platform for neuroscience.

The Lenz lenses with the MR incubator were used for MR microscopy on fixed/acute hippocampal slices and on OHSC. The results from the MR microscopy measurements show that in OHSC the crude cytoarchitecture is visible while the OSHC are kept viable. Therefore, the introduced system is ready to be used for longitudinal studies of OHSC which is ongoing for studying the progression of epilepsy.

Table of contents

1

The Bigger Picture

1.1 Motivation

Brain diseases, such as Epilepsy, Alzheimer's, Parkinson's or chronic depression are inherently difficult to study, since it is challenging to isolate the causes of certain diseases, with just relying on symptoms, or in many cases the patients description of these symptoms. Treatment then is only reducing symptoms of the diseases rather than a cure. It remains a challenge to pinpoint the spatial origin of certain defects. One treatment option is the use of medical drugs, but even the effect of these drugs often remain concealed, and drugs only relieve some patients of their symptoms, but typically not every patient. Additionally drug-related treatment is spatially non-targeted, which can lead to severe side effects [1–3].

Non-drug related treatment methods are on the rise, i.e. deep brain stimulation (DBS), which can significantly reduce symptoms of some diseases, such as Parkinson [4, 5] and chronic depression [6, 7], where the spatial source of the disease is known and it is possible to place DBS electrodes accurately enough. Localising malfunctioning brain matter is also interesting for Epilepsy treatment, where an intra-cortical array of electrodes can be used for presurgical evaluation to decide which parts of the brain to be surgically removed of the brain matter [8]. Recent developments in brain implants make better localisation of such brain regions possible [9], but are still very invasive.

A technology to complement these methods is the use of magnetic resonance imaging (MRI) and magnetic resonance spectroscopy (MRS) methods. MRS is capable of resolving metabolic changes in the brain, while brain morphology can be represented by MRI and to some extend functional MRI (fMRI) can illustrate the brain activity. Another method is the use of tractography (or fibertracking) which indicates connectivity within the brain. However, these MR methods inherently suffer from low spatio-temporal resolution, usually in

the lower millimetre range in clinical settings. The relationship between MR signal and the underlying tissue microstructure additionally remains unclear, and this relationship needs to be elucidated to interpret diagnostic results. The onset of brain diseases can be detected by a change in these type of signals. Usually patients will only step forward once the disease has already altered the brain significantly and great effort is undertaken to find pathological patterns in the signal indicating the onset of such diseases [10–15].

Magnetic Resonance Microscopy (MRM) increases spatio-temporal resolution, using dedicated hardware, advanced pulse-sequences and post-processing [16–27]. *In vivo* MRM measurements of epileptic mice indicate that a change in the tractography signal and the MR spectrum can predict the development of Status Epilepticus towards Epilepsy, and can quantify to some extend how strong the epilepsy will be [28–31]. With *in vivo* measurements it is often not possible to differentiate the smaller sub-regions of the brain, such as the sub-regions in the hippocampus (a key structure i.e. in mesial temporal lobe epilepsy), and therefore can only give an estimate. Higher resolution tractography connectomes down to $43\,\mu m^3$ isotropic resolution have been recorded on perfusion-fixed dead rats with MR contrast agent [32, 33], but measurements on fixed tissue have different properties than viable tissue [34] and can thus not be used as a reference for MR signal change induced by the onset of diseases.

One way to combine high-resolution MR images while maintaining relatively short scan times, is to get the specimen, or the biological sample as close to the application specific detector coil as possible. This type of high resolution MR imaging has already been done in single neuronal cell experiments [35–39], but single cells are not representative for the complexity of this neuronal circuitry. Thus it is impossible to predict neurological diseases based on single cell experiments. This trade-off between high spatio-temporal resolution and maintaining the neuronal connectivity of the brain can be met by using physical brain slices and brain slice cultures which are established as biological model organisms for such diseases [40–42]. The Blackband group used MRM to acquire MR images, MR spectra and diffusion weighted images of fixed and accute brain slices [43–47]. However, to reveal the changes induced by neurological diseases requires to study the brain tissue longitudinally during maturation of the corresponding disease which even mouse models takes weeks to months.

Brain slices and brain slice cultures have long been established as model organism for diseases and in drug development [48]. In recent years, a variety of technological devices and systems have been developed to accommodate for the environment the brain slices need to survive, and to manipulate, record or use certain characteristics of the slices [49]. A number of brain slice nurturing and handling devices for electrophysiological [50–52],

chemical [53] or optical [54] manipulation and measurements were published, that are not MR compatible. Using brain slices and slice cultures in magnetic resonance microscopy has not yet made it's way to a larger community. There are MR compatible incubators or nurturing devices, i.e. for tissue engineering [55, 56], cells and cell cultures [57–61], optical nerves [62, 63] and extracted cultured tissue [64], but these do not accommodate for the special requirements imposed by brain slice culturing.

Few publications deal with brain slices and magnetic resonance. Bai *et. al.* published a system based on the NMR mouse [65]. A very appealing feature of this open low field system, is the possibility of simultaneous MR, optical and electrosphysiological measurements. The measurement setup was hence used to correlate neuronal activity to diffusion MR imaging [66]. Although it offers some considerable advantages for fundamental research, it is not fitted for imaging experiments, since it does not encorporate a gradient system. Additionally due to the low field of 0.32 T, some experimental findings are not transferable to clinical imaging systems. The system by Flint *et al.* is designed for vertical small bore MR spectrometers [67, 68]. *Acute* brain slices are nurtured and kept viable by supplying oxygenated artificial cerebrospinal fluid (aCSF). The slices are stabilised by a nylon net, ensuring close proximity to the detector coil and orthogonal orientation towards the 14 T static magnetic field. Both of these systems use acute brain slices, but no brain slice cultures, and are therefore not fitted to for translational studies of brain tissue for monitoring disease progression.

Most publications on high resolution MR microscopy use readily available surface micro coils or hand wound solenoidal micro coils for their measurements. There are some disadvantages accompanied with these coils. For example micro surface coils will not always cover the whole sample, especially when hippocampal slices are used [47]. With hand-wound solenoids, the used coils are unique, and therefore the measurements are not easily reproducible due to the lack of reliable hardware. Additionally with miniaturisation of solenoids, winding by hand lacks precision. Other manufacturing methods have been suggested, e.g. laser-lathe lithography, where a copper conductor is directly structured onto a glass capillary [69]. This method shows the potential to structure micro solenoids, but the integration with other manufacturing methods is difficult and miniaturisation is limited by the capillary wall thicknesses (filling factor decreases).

The mentioned challenges lead the following research hypotheses:

1. Can we design and build magnetic resonance microscopy detectors with the potential of automated manufacturing and miniaturisation to close the gap between single cell experiments and studies on complex neuronal networks?

2. Can we perform magnetic resonance microscopy on mouse brain slices with an animal magnetic resonance imaging system, and how can we optimise it?

3. Can we design and manufacture a platform to hyphenate brain slice culturing and magnetic resonance microscopy?

4. Can we resolve specific sub-regions within brain slices *in vitro* that are associated with a significant brain disease and monitor its pathological progression using magnetic resonance microscopy methods?

1.2 Scope of this thesis

This thesis is organised in 5 main chapters:

- Chapter 2 provides an introduction to the theory of magnetic resonance. The basic principles from nuclear spin to magnetic resonance imaging, are explained. A special focus is placed on diffusion in MRI, e.g. diffusion weighted imaging and diffusion tensor imaging. The concept of magnetic resonance microscopy is introduced and the principal figures of merit for characterising MRM detectors are explained. The chapter closes with a brief introduction to the brain structure, the hippocampus and organotypic hippocampal slice cultures (OHSC), which are used as biological model for brain diseases.

- Chapter 3 introduces three different types of MRM detectors, Magnetic resonance force microscopy (MRFM) coils, hollow solenoidal micro coils and Lenz lenses. For all detector types, MRFM coils, hollow solenoidal microcoils and flexible lenz lenses, the development, manufacturing and characterisation procedure is described.

- Chapter 4 describes the implementation of an MR compatible nurturing platform for organotypic hippocampal slice cultures. A state of the art on magnetic resonance of brain slices is given. A technical characterisation of the platform and brain slice survival tests conclude the chapter.

- In chapter 5 the method of virtual staining as a tool in neurological research is introduced and applied to fixed brain slices of healthy and epileptic mice. Brain tissue measurements obtained with the Lenz lenses and the MR compatible nurturing platform are presented.

- The thesis is concluded in chapter 6 by a critical review of the obtained results and their present and potential implication for the scientific community.

1.3 Key Results

This thesis mainly contributed to the field of magnetic resonance microscopy and the posed hypotheses with the following key results:

1. Hollow solenoidal micro coils with an optimised filling factor were built. Thus their signal-to-noise ratio is increased to maximise signal strength in neuronal single to multi-cell experiments.
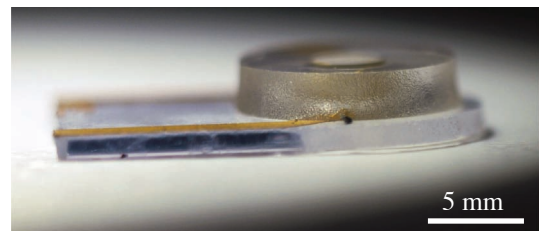
Fig. 1.1 Hollow micro coil on glass.

Fig. 1.2 Lenz Lens.

2. Flexible Lenz lens detectors were designed and built to fit into small animal magnetic resonance scanners. These detectors increase signal strength for experiments on hippocampal slices. The lenses can be used to increase the performance in magnetic resonance microscopy setups in small animal scanners.

3. An MR compatible platform that can facilitate common biological protocols to culture brain slice cultures was designed and built. It brings the necessary environment, such as gas control, temperature control and culturing plates into the MR scanner, while maintaining MR compatibility. Thus magnetic resonance microscopy and brain slice culturing is merged to support a new method of studying and screening brain slice cultures towards changes induces by neurological diseases or induced by drug treatment.

Fig. 1.3 MR Incubator.
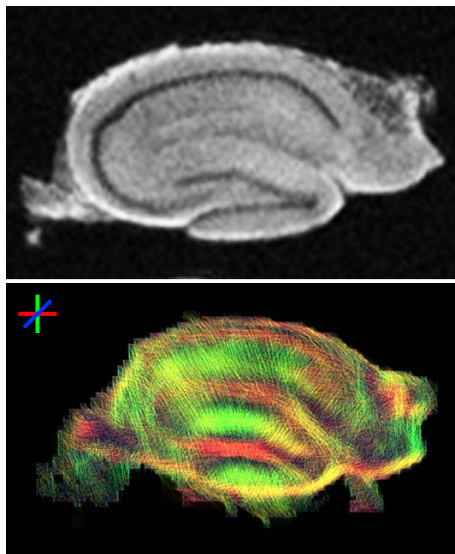
Fig. 1.4 FLASH/DTI of OHSC.

4. In a joined project within the BrainLinks-BrainTools Cluster of Excellence at the University of Freiburg, the method of virtual staining of brain slices was developed in strong collaboration with the University Hospital Freiburg[a]. This method uses magnetic resonance microscopy, specifically diffusion tensor imaging and tractography, to resolve changes induced by epilepsy in the sub-regions of the hippocampus.

[a]Hardware development and testing by Robert Kamberger. MR image acquisition and DTI processing by Katharina Goebel-Guéniot, Medical Physics, Department of Radiology. Brain tissue cultivation, stainings and data intepretation by Johannes Gerlach, Experimental Epilepsy Lab, Department of Neurosurgery

2

Theory

This chapter provides an overview of the theory of magnetic resonance. The basic principles, from nuclear spin to diffusion tensor imaging, are briefly explained. The concept of magnetic resonance microscopy and characteristics are introduced. For orientation, the brain, the hippocampus and organotypic hippocampal slice cultures are introduced.

2.1 Magnetic Resonance

2.1.1 Magnetic Resonance Basics

It is well known, that magnetic fields influence the intrinsic atomic spin. A constant magnetic field B_0 forces the spins to align parallel or antiparallel to the magnetic field vector, slightly favouring the parallel, lower energy state. Spins precess within the B_0 field, due to the spins inherent angular momentum. Their precession frequency, the Larmor frequency ω_{L}, can be directly correlated to the magnetic field strength B_0 by the nuclei dependent gyromagnetic ratio γ as shown in equation 2.1 [70].

$$\omega_{\mathrm{L}} = -\gamma \cdot B_0 \tag{2.1}$$

The sum of the spin magnetisation, which results from the excess of spins in the lower energy state, is called the net magnetisation M_0. The net magnetisation determines the maximum MR signal [71].
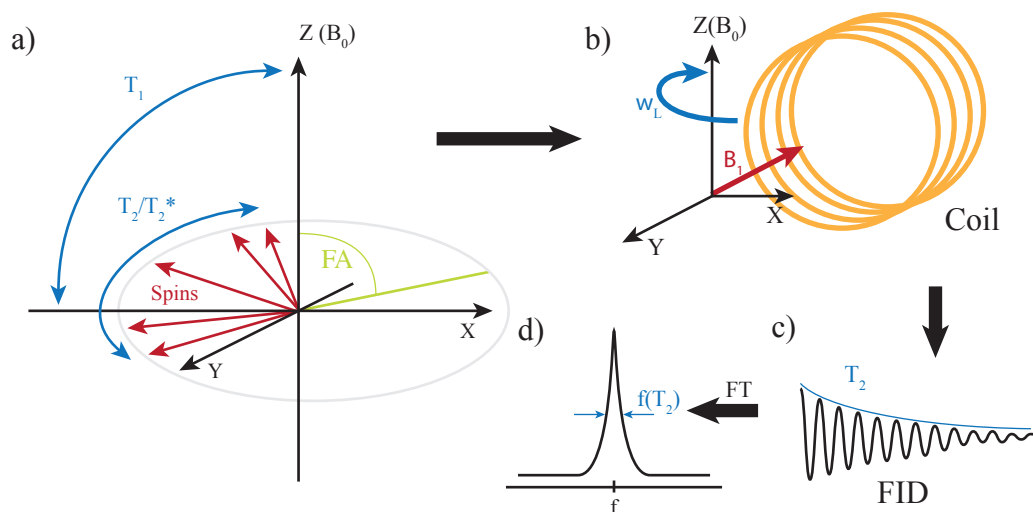
Fig. 2.1 a) Theoretically the NMR signal decays for two reasons: After being flipped by the flip angle (FA), the net magnetisation realigns with B_0 in Z–direction, which is called the spin–lattice–relaxation with its decay constant T_1. Furthermore, the spins are dephasing, decreasing the net magnetization. This process is called spin–spin–relaxation, with its decay constant T_2. b) When a coil is placed around the sample, the net magnetisation induces a voltage in the coil, which can be recorded, and is termed the free induction decay (FID) c). The Fourier Transformation (FT) of the FID is the common illustration of the NMR spectrum d). Image adapted from [72].

Acquiring a magnetic resonance signal from specific nuclei requires the spins to be excited by an electromagnetic radio frequency (r.f.) pulse B_1 of specified length and power at the corresponding Larmor frequency. The r.f. pulse tips the net magnetisation from their equilibrium state towards the transverse plane by the flip angle (FA). After the r.f. pulse passes, the net magnetisation realigns along the B_0 field to their equilibrium in a precessing motion. The signal is derived from the net magnetisation of the spins, which decreases with time mainly for two reasons. The first reason is M_0 realigns with the magnetic field B_0 to its thermal equilibrium. This process is termed spin–lattice–relaxation with its decay constant T_1. Secondly, M_0 is reduced by a dephasing of the spins, due to random local fluctuations in the B_0 field, causing the spins to precess at different frequencies. The dephasing is known as spin–spin–relaxation, with its time decay constant T_2. In reality the dephasing of the spins happens even faster, since the chemical difference in the immediate vicinity leads to local inhomogeneities of B_0. This very fast process is present in almost every experiment, and its quasi decay constant is T_2^*. Since the spins, and therefore their net magnetisation, decay to their equilibrium freely, the induced oscillating current is known as free-induction decay (FID). The precession of the

net magnetisation induces a voltage V_{ind} in the receiver coil that encloses the sample. The induced voltage follows Faradays law of induction [71, 73–75].

2.1.2 Magnetic Resonance Imaging

Acquiring spatial information of matter by magnetic resonance imaging (MRI) is possible through magnetic field gradients superimposed on B_0 which lead to a gradient in ω_0 and thus a different phase or frequency. This encoding scheme as introduced by Mansfield and Lauterbur [76, 77] and the introduction of the Fourier transformation for image reconstruction [78, 79] are the foundation of MR imaging. Recording images requires three magnetic field gradients.

The first gradient is applied while irradiating the sample with an r.f. pulse of defined bandwidth which has its centre at the Larmor frequency. Since the Larmor frequency directly depends on the static field strength, the change in magnetic field introduced by the magnetic field gradient causes only a slice of the volume to be excited by the r.f. pulse, thus it is called the slice selection gradient. The second gradient is applied after r.f. pulse excitation, and changes the phase of the spins, and is thus called the phase gradient. The last gradient is applied during the FID acquisition phase, which alters the Larmor frequency according to the voxel position, and thus is called the frequency gradient.

Recording an MR image and exploring different contrast mechanisms requires the magnetic field gradients to be switched with precise timings, which is called an imaging sequence. The main imaging sequences are gradient echo and spin echo sequences. More advanced sequences are typically based on one or both of these sequences [80].

Spin Echo Sequences - RARE

In a spin echo (SE) sequence the spins are first flipped by 90° and tipped into the transverse plane. Since the spins dephase directly (with time constants T2/T2*), the MR signal fades off. Then a 180° r.f. pulse is applied, to rephase the spins. When the spins are rephased completely, which is called the spin echo, the MR signal is acquired. The time from 90° pulse to the spin echo formation is called the echo time (TE), and the 180° pulse is applied at TE/2 (see fig. 2.2). The time one needs to wait before repeating the excitation pulse restarting the sequence is called the repetition time (TR). Since in the SE sequence TR is limited by the spins reaching their equilibrium state within the static magnetic field (with time constant T1), this method is inherently slow.

A method to speed up SE sequences is by using multiple 180° pulses, starting at TE/2 and equally spaced by TE, as depicted in fig. 2.2. These multiple 180° pulses make acquisi-

tion more rapid, since there is no need to wait for the spins to reach equilibrium, and the relaxation is enhanced. Thus this method is called rapid acquisition by relaxation enhancement (RARE) [81].

SE sequences are insensitive to field inhomogenieties introduced by local field variations (e.g. by different magnetic susceptibilities) or magnetic field gradients, since echo formation is forced by two r.f. pulses from the same coil, thus compensating for inhomogenieties.
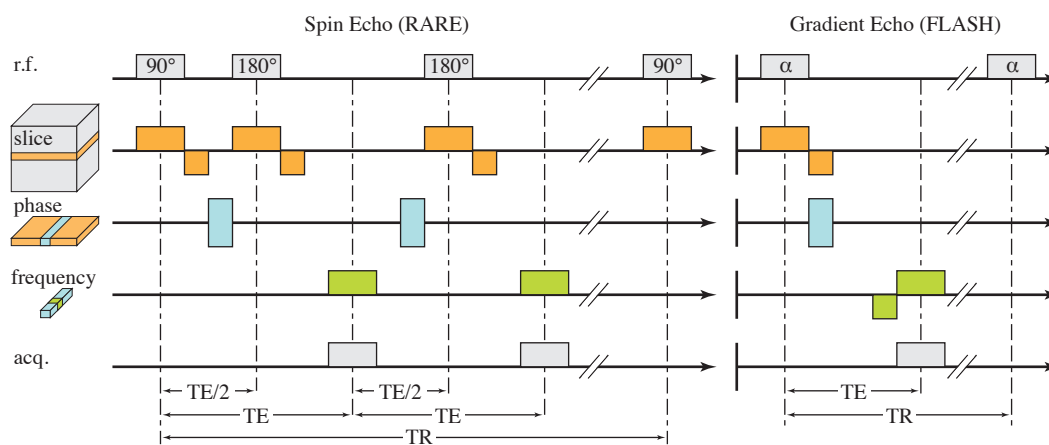
Fig. 2.2 Timing diagrams for gradient echo (FLASH) and (turbo) spin echo (RARE) imaging sequences.

Gradient Echo Sequences - FLASH

In a gradient echo (GRE) sequence, the spins are flipped only by a low angle (often between 15° and 60°). Dephasing and subsequent rephasing of the spins is achieved through application of a magnetic field gradient (negative gradient for dephasing, positive gradient for rephasing). This results in a forced echo due to the gradient, thus called a gradient echo. GRE sequences can be much faster than the SE sequences, since echo formation does not depend on T2/T2* times, but rather on gradient strength and switching times. Gradients can be switched rapidly after each other, and due to the combination with low spin angles, this method is called fast low shot angle (FLASH) [82]. GRE sequences are prone to field inhomogeneities, since the GRE signal is created by an r.f. pulse, and the echo is forced by a field gradient form another source.

2.1.3   Diffusion Magnetic Resonance Imaging

Most explanations in this section about Diffusion Magnetic Resonance Imaging are taken and complemented from the publications of Mori et al. [83] and Van Hecke et al. [84].

Classical magnetic resonance imaging can elucidate the structure of samples or specimen, but not dynamic processes. One way, to give MRI more functionality, is to make use of the diffusion of protons in the sample. The physical resolution of MR images is supposedly limited to about $10\,\mu$m, which is approximately the length water-molecules move in a typical scan time window of $10\,$ms-$100\,$ms [83]. However, by applying diffusion gradients (magnetic field gradients), one can use diffusion to retrieve additional information about the sample.

There is a variety of metrics that can be computed from these diffusion measurements useful for different applications. One great advantage over classical MR imaging is the possibility to gain quantitative rather than qualitative results, so as to compare different patient groups or specimen. Diffusion weighted imaging (DWI), encodes an additional contrast mechanism in MRI, which can highlight tissue damage and can be used to evaluate how long the tissue has been damaged (i.e. age of a stroke). The change in signal of DWI results from the underlying tissue microstructure. Thus from the change in signal it is typically possible to draw conclusions of how the tissue microstructure changed without actually seeing the change itself. However, the obtained results have to be handled with care, since the postprocessing of the data is a result of the underlying theory on how tissue microstructure influences the MR signal, which is a topic of current research and not yet fully understood [85].

Diffusion in MR imaging

The contrast in an MR image can be influenced by a number of parameters, i.e. echo time (TE) and repetition time (TR). The MR signal S can be expressed by these parameters and combined with diffusion (D) and the proton density (PD) to [83]:

$$S = PD \cdot (1 - e^{-\frac{TR}{T1}})\, e^{-\frac{TE}{T2}}\, e^{-bD} \tag{2.2}$$

By introducing diffusion gradients into the pulse sequence diffusion is visualised in an image. As can be seen from the pulse sequence in fig. 2.3, the diffusion gradients are applied before and after refocussing of the magnetisation with equal spacing to the refocussing pulse. If there is no proton diffusion between the diffusion gradient pulses, the diffusion gradients cancel each other out. When diffusion occurs, the voxel signal with

high diffusion gets attenuated the most [86, 87]. In tissue, the diffusion might be restricted or hindered anisotropically. The MR signal then depends on the direction of the diffusion gradient. With different gradient direction the obtained image therefore shows different image contrast. This fact is used to reconstruct the direction of the diffusion, which is used to compute fractional anisotropy maps (see subsection 2.1.3).

In equation 2.2 the b-value is the diffusion weighting factor and can be calculated from the Stejskal-Tanner equation [84][1]:

$$b = \gamma^2 G^2 \delta^2 (\Delta - \frac{\delta}{3}) \tag{2.3}$$

If the b-value is set to zero, the signal acquired does not depend on the diffusion, and is thus a static MR image. The easiest way to influence the b-value is by adapting the diffusion gradients spacing Δ. It is, however, also possible to change the diffusion gradient duration δ or the diffusion gradient strength G, where γ is the gyromagnetic ratio. It should be noted, that with choosing high b-values the DWI sequence sensitivity increases towards diffusion, but so does signal attenuation. An appropriate b-value needs to be chosen for a specific application (see fig. 2.3).
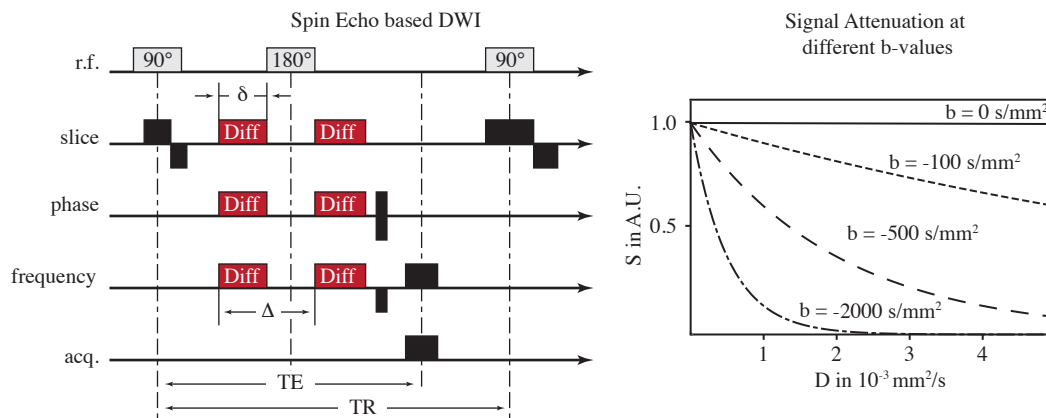
Fig. 2.3 Left: Spin echo based DWI sequence. Right: Signal attenuation of an diffusion MR signal for different b-values.

Diffusion Weighted Imaging - DWI

MR images can be influenced by changing the sequence parameters (TR, TE and b) to alter image contrast, thus acquiring weighted images. While PD images are determined by the amount of free water protons in a specific voxel, T1- and T2-weighted images are influenced by the environment (for example viscosity or close macromolecules, e.g. the

---

[1]A mathematical derivation of the Stejskal-Tanner equation can be found in [88]

Table 2.1 Weighted MR imaging.

	PD	**T2-weighted**	**T1-weighted**	**Diffusion-weighted**
TR	long	long	short	long
TE	short	long	short	long
b	small	small	small	large
Used for (e.g.)	Anatomy & Disease entity	Disease depiction	Anatomy	(Age of) stroke

tissue microstructure). A diffusion weighted image (DWI) is weighted by the b-value ($b \neq 0$) and therefore differs from other weighted images with $b = 0$. Image contrast depends on the diffusion in a voxel being restricted, hindered or free. The image appears brighter where there less diffusion occurs. The image depends on the diffusion gradient direction. By combining images from different diffusion gradient directions a mean DWI can be acquired. The influence parameters for weighted images are summarised in table 2.1 [80, 83, 89].

Apparent Diffusion Coefficient - ADC

By combining multiple images with different weightings, or contrasts, one can amongst other extract T1, T2, T2* or PD. This combination of contrasts is sometimes called quantitative MRI [85]. This can similarly be done by using different b-values and then combining these signals. A simplified version of the signal equation 2.2, where all parameters that are not related to diffusion are reduced to S_0 can be written as:

$$S = S_0 e^{-bD} \quad \text{or} \quad D = -\frac{\ln(\frac{S}{S_0})}{b} \tag{2.4}$$

And if different b-values are used, this can be combined to:

$$\begin{aligned} S_1 &= S_0 e^{-b_1 D} \\ S_2 &= S_0 e^{-b_2 D} \end{aligned} \tag{2.5}$$

and thus

$$\frac{S_2}{S_1} = e^{-(b_2-b_1)D}$$

$$D = -\frac{\ln\frac{S_2}{S_1}}{(b_2-b_1)} = ADC \tag{2.6}$$

This signal is referred to as the apparent diffusion coefficient (ADC)[2], at the point of signal generation. Combining these signals to an image is called an ADC map. Note that it is called apparent, since the actual diffusion of the protons does not change the physical property, but rather the diffusion is restricted by the physiological structure of the sample [90, 91]. Using different b-values and combining these images to acquire an ADC map is a representation of the mean diffusivity (MD) in the voxel, since it combines diffusion in all imaging directions recorded. Thus an ADC map it does not give information on the direction of the diffusion, but only on the diffusion strength in a specific voxel.

Fractional Anisotropy - FA

The ADCs depend on the direction of the diffusion gradient. If a diffusion gradient is applied along the X-axis, only diffusion motion in X direction reduces the signal intensity. By combining X-, Y- and Z-gradients, the direction of diffusion can be measured in any arbitrary direction. However, since measuring in an infinite number of directions is impractical the measurements along the different axes are fitted to 3D ellipsoids. Six values are needed to fit these ellipsoids: 3 values for the lengths of the axes of the ellipsoids (Eigenvalues) and the values for the direction of these axes (Eigenvectors). If normalised, the Eigenvalues can give a measure for the anisotropy of the ellipsoids. This measure is called fractional anisotropy (FA), and has values between 0 (isotrop) and 1 (anisotrop). Allocating an FA value to each voxel (direction and strength) is called an FA map and gives information on the direction of the diffusion [83, 92]. For better representation of the direction coloured FA maps are used in which the colours are assigned to the diffusion direction, thus these are called directionally encoded colour FA maps (DEC FA map). In this thesis the colours are encoded as red for x (left-right), green for y (bottom-top), and blue for z (back-front).

---

[2]sometimes also called the trace, since it is the mathematical trace of the diffusion tensor.

Diffusion Tensor Imaging - DTI

Fitting splines onto these FA maps, where the splines are connected in direction of the
ellipsoids main axes in each voxel, is called an diffusion tensor image (DTI). Fitting these
splines requires a seed pixel, and termination of such splines is achieved, when the FA
value falls below a certain threshold, such that isotropy is reached. Within the brain,
the directionality of the FA maps are a representation of the tissue microstructure, and
the strength of directionality is correlated to the axon count and density. It has been
demonstrated that these fitted splines can represent major axon-bundles in the brain, and
therefore can show how the connection in the brain (tractography or fibre tracking) [93,
94]. An illlustration of the described processing pipeline is given in fig. 2.4 [95, 96].
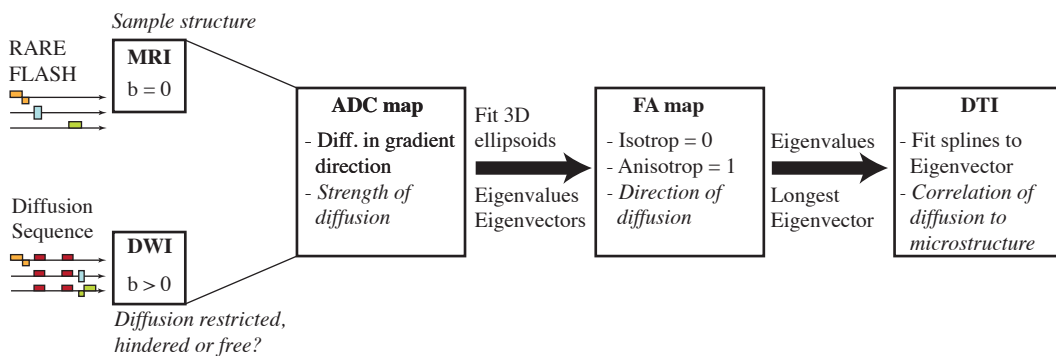
Fig. 2.4 Processing pipeline from DWI to DTI.

2.2   Magnetic Resonance Microscopy

In magnetic resonance imaging there is a trade-off between spatial resolution, signal-to-
noise and acquisition time. These interdependent quantities can be tailored to a specific
application, so as to push one of them while at least one of the other quantities suffers
[97]. In clinical MRI resolution down to below the mm regime is possible. However, it is
still difficult to study the underlying microscopic structure of the brain and correlate it to
the MR signal. Diffusion MR methods relate to a certain extent to the underlying tissue
microstructure, but the relationship between MR signal/contrast and the underlying
microstructure is not completely understood due to the lack of MR signal that has been
correlated independently to the underlying anatomical cytoarchitecture of the brain [98].
Magnetic resonance microscopy (MRM) are MR methods with sub-millimetre resolution
in at least one dimension. A goal of MRM is to push resolution to cover the lack of
correlation between MR signal and tissue microstructure. Therefore, with long scan times

and dedicated custom hardware at high field strengths, single cell resolution in the lower micrometre range is possible [36, 99, 100].

2.2.1 Magnetic Resonance Microscopy and Sensitivity

Magnetic resonance has an inherently low signal strength. Therefore, hardware and software development has been pushed to achieve high signal strengths and low noise levels [101, 102]. A simplified signal-to-noise (SNR) equation was derived by Webb [71]:

$$\text{SNR} \propto \left(\gamma B_0\right) \cdot \left(\frac{\gamma^2 h^2 B_0 N_S}{16\pi^2 kT}\right) \cdot \left(\frac{1}{V_{\text{noise}}}\right) \cdot \left(\frac{B_1}{I}\right) \tag{2.7}$$

This equation brakes down the dependencies of the SNR into four terms.
The first term represents the magnetic field dependency. It includes the magnetic field strength B_0 and the gyromagnetic ratio.
The second term shows the dependency on the sample itself. It is derived from the samples net magnetisation, and includes the number of protons N_S, the Boltzmann's constant k, the Planck's constant h and the absolute temperature T of the sample.
The third term is the influence of the induced random noise voltage V_{Noise}. This term depends on the sample/specimen and the detector. When sample volume is large, and detectors can be large, the noise is dominated by the specimen. When scaling down, the noise is dominated by the detectors resistance, as is the case for magnetic resonance microscopy.
The last term depends on the detector, and how efficient the detector transmits the electromagnetic r.f. field B_1 per unit current I.
In magnetic resonance microscopy sample volumes can be in the lower nanolitre range to resolve for example single cell metabolites and dynamics. As described by the reciprocity principle [103], the detector sensitivity is at maximum, when the detector is as close to the sample as possible (high filling factor). Additionally, detector efficiency increases with decreasing coil size and thus the mass sensitivity increases. Miniaturisation however, comes with significant drawbacks, as for example noise is dominated by the detector, magnetic susceptibility mismatches gain in influence and manufacturing becomes challenging [104–106].

2.2.2 Figures of Merit

Most explanations in this section about figures of merit in MRM are taken and complemented from the publications of Baxan et al. [107] and Haase et al. [108].

According to the principle of reciprocity, the signal induced by a spin is largest, where the transmission signal is largest. This means, as Haase *et al.* write, "the important conclusion of this principle is that the B_1 field strength of a coil at any point in space at a fixed power during transmission is equivalent to the sensitivity during detection" [108]. Therefore, the goal of coil design for MR is to maximise B_1 per unit current. There are two principle things with which to achieve the maximum B_1. Firstly, the coil dimensions need to be matched to the sample dimensions, which is expressed by the filling factor η, where the sample volume V_{sample} is divided by the active coil volume V_{Coil}:

$$\eta = \frac{V_{sample}}{V_{Coil}} \tag{2.8}$$

It is desirable to maximise the filling factor, which becomes increasingly difficult with decreasing coil size, since the active coil volume might be occupied by support structures. The second measure to maximise B_1 is to reduce the losses in the coil. This is generally covered by the quality, or Q-factor. For a coil it is defined at the frequency ω multiplied by the coils inductance L, divided by the coils resistance R.

$$Q_L = \frac{\omega L}{R} \tag{2.9}$$

While this definition holds for a set-up where only a coil is used, we also need to consider other losses, that are not directly related to the B_1 itself. Since the induced MR signal needs to be transmitted optimal power transfer is a significant part of probehead characterisation and design. Since we do not want to reflect the power induced by the MR signal, the coil impedance Z_L needs to be matched to the characteristic impedance of the transmission line Z_0 at the larmor frequency ω_0, which is usually $50\,\Omega$. As we want to reduce ohmic losses, matching of the coil is achieved by operating the coil as a resonant circuit by attaching a tuning capacitor C_T and matching capacitors C_M[3]. The Q factor of this resonant circuitry, can be measured from its reflection curve, by dividing the resonance frequency ω_0 by the width of the resonance $\Delta\omega$ at half maximum (at -3 dB) :

$$Q = \frac{\omega_0}{\Delta\omega} \tag{2.10}$$

This Q factor covers losses, that are not only a result of interaction with the magnetic field. Since the r.f. field induces electric losses efficiently in conductive materials, one needs to carefully design the probehead. The electric near field of the coil induces displacement currents in dielectric materials. This property of a dielectric material is described by its

---

[3]For a general introduction to impedance tuning and matching see [109, 110]

loss tangent $\tan(\delta)$. The Q factor measured as described in equation 2.10, also covers losses induced by the sample in the r.f. field of the coil. The losses induced by the sample itself can not be avoided, since the the interaction of the sample with the r.f. field is at the core of the magnetic resonance experiment. In an ideal MR detector, the losses induced by the sample are the only ones reducing the Q factor. Measuring the Q factors with a sample loaded (Q_{loaded}) to the coil and without sample (Q_{unloaded}) can determine the loss mechanisms.

$$\frac{S}{S_0} = \sqrt{1 - \frac{Q_{\text{loaded}}}{Q_{\text{unloaded}}}} \tag{2.11}$$

Generally this is a good measure, to whether the coil is sensitive where it needs to be. If the Q-factor does not drop in the loaded case, the losses are not dominated by the sample, but either by a low conductivity or lossy materials. The coil does not generate the r.f. field in the sample, but elsewhere in the resonance circuitry, which can be determined by using pickup coils to locate r.f. leakage.

Since MR microscopy is inherently insensitive, due to the nature of the method having very low signal (see section 2.1.1), one measure is the mass sensitivity $S_m = \text{SNR}/\text{mol}$ and the concentration sensitivity $S_c = \text{SNR}/\text{C}$. As the sensitivity is the slope of the SNR calibration curve versus the amount of active sample volume, we need the time domain SNR_t, which is defined as [107]:

$$\text{SNR}_t = \frac{(B_1/i)\omega_0 M_0 V_s}{\underbrace{\sqrt{4k_B T_s R_{\text{noise}} \Delta f}}_{=V_{\text{noise}}}} \propto \frac{B_1/i}{\sqrt{R_{\text{noise}}}} \tag{2.12}$$

Here, B_1 is the r.f. field of the coil divided by the current i. The larmor frequency ω_0 depends on the main magnetic field and the nuclei, the net magnetisation is M_0 and the active sample volume is denoted as V_s. The whole term is devided by the square root of the Boltzmann constant k_b, the coil temperature T_s, the coil electrical resistance R_{noise} and the receiver bandwidth Δf. From the sensitivity, the limit of detection for concentration LOD_c and mass LOD_m is defined for the concentration in mol/l or the mass in mol required to achieve an SNR of 3.

$$\text{LOD}_c = \frac{3}{S_c} \quad \& \quad \text{LOD}_m = \frac{3}{S_m} \tag{2.13}$$

In a nutation spectrum, which is similar to a flip angle calibration, sample excitation is stepped through increasing excitation energy, by either prolonging excitation pulse length or ramping excitation pulse power (see fig. 2.5). At the signal amplitude maximum the flip angle is 90°. A detector is more efficient if the 90° flip angle requires less energy. In accordance with the principle of reciprocity, the sensitivity of a detector coil is characterised

by the generated B_1 field, the frequency of the flip angle calibrations envelope function normalised by the excitation pulse power P_{exc} is called the detector efficiency η_d. From equation 2.12, on can derive that the efficiency directly relates to the SNR.

$$\eta_d = \frac{B_1}{\sqrt{P_{exc}}} = \frac{B_1}{i\sqrt{R_{\text{noise}}}} \tag{2.14}$$

The B_1 field amplitude can be computed from the nutation frequency ω_{nut}, the gyromagnetic ratio and the tilt angle Θ of the detector towards the main magnetic field B_0 [70]:

$$\omega_{nut} = |\frac{1}{2}\gamma \cdot B_1 \cdot sin(\Theta)| \tag{2.15}$$

In case of linearly polarised r.f. radiation, the factor 1/2 needs to be considered. The amplitude ratio, A_{810}/A_{90}, at 90° and 810° increases with better field homogeneity and can thus be used as a measure for the homogeneity.

$$\frac{A_{810}}{A_{90}} \leq 1 \tag{2.16}$$
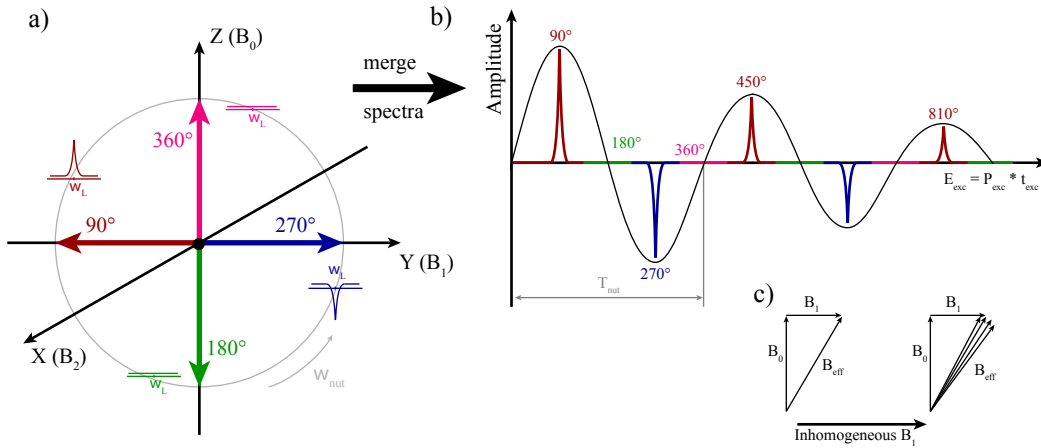
Fig. 2.5 The flip angle is a function of the excitation pulse energy E_{exc}. With different flip angles the the amplitudes of the recorded NMR spectra changes a). Multiple spectra are recorded with continuously increased excitation pulse energy and then combined b). The envelope function of these spectra oscillates at the nutation frequency. If the spins are excited with an inhomogeneous B_1, the spins are flipped by different angles, thus decreasing the net magnetization c). This effect is visible as the decay of the spectra's amplitudes at higher flip angles. Image taken from [72].

MR Image SNR and Geometric Distortion

Within this thesis, the MR image signal-to-noise ratio (SNR_{image}) and the 2 dimensional geometric distortion of MR images are computed as explained in the standards by the National Electrical Manufacturers Association (*Virginia, USA*) [111], with a few alterations due to size limitations of MR microscopy. To make a reproducible and comparable measurement, a few terms need to be defined (shown in fig. 2.6, adapted from [112]):

Measurement Region of Interest (MROI) is a centered, geometric area of regular shap (e.g. a square or a circle). It covers at least 75 % of the signal generating area of the phantom,

Image Signal (S_{image}) is the mean pixel value within the MROI of the original image.

Image Noise (S_{noise}) is the random variations in pixel intensity in the MROI.

Image signal-to-noise ratio (SNR_{image}) is a single number obtained by dividing S_{image} by S_{noise}.

Image artefact is an anomaly, or distortion, in the image, that excludes random noise, which does not represent the structure of the scanned object. It results from the chemistry or the structure of the scanned object, and its signal appears elsewhere as it is physically positioned.

As explained, the image signal is the mean pixel value within the MROI. To determine the signal noise within a single image, the noise is measured outside the signal generating area (the phantom), and afar from visible image artefacts. It is determined by drawing an MROI in the background region, away from the read and phase direction. This places the MROIs for the determination of the noise signal into the corner of the image. The noise in a single image can then be computed from the standard deviation σ_{noise} of the image noise S_{noise}, divided by a correction factor to compensate for the Rayleigh distribution:

$$S_{noise} = \frac{\sigma_{noise}}{0.66} \tag{2.17}$$

And thus the image signal-to-noise ratio can be calculated to be:

$$SNR_{image} = \frac{S_{image}}{S_{noise}} \tag{2.18}$$

To evaluate the geometric distortion of MR images, either a circular or a rectangular phantom is used. The physical dimensions of the phantom are compared to the MR image
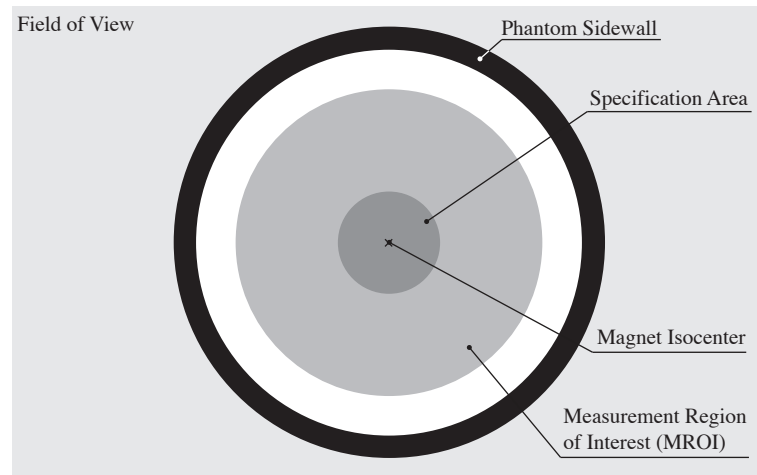
Fig. 2.6 Areas of interest in an MR image for computing the image SNR according to [112].

dimensions, by evaluating the lengths along the lines depicted in fig. 2.7. The geometric distortion is the maximum value of the difference of the actual physical dimensions of the phantom L_a and the dimensions measured from the MR image L_m, normalised by L_a in percent [112].

$$\text{Geometric Distortion} = \text{MAX}\left[100\frac{|L_m - L_a|}{L_a}\right] \qquad (2.19)$$
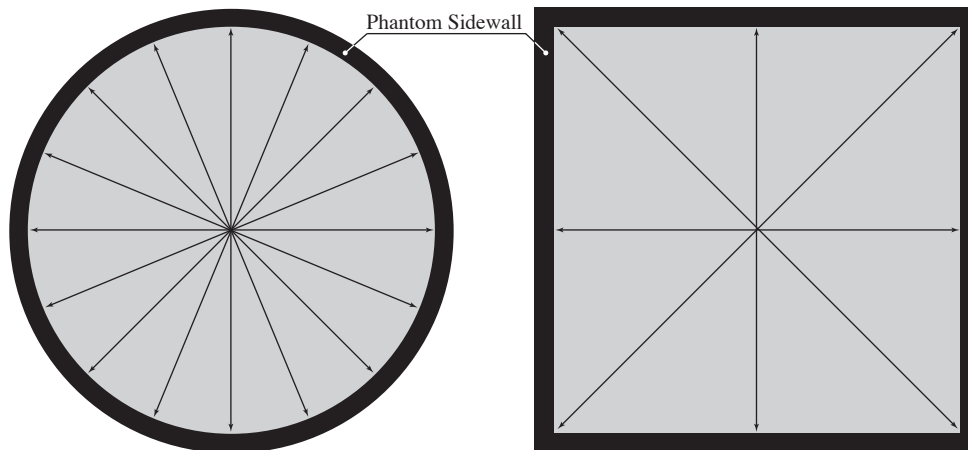
Fig. 2.7 Distances to be compared in a circular phantom (left) and a rectangular phantom (right) to compute the geometric distortion modified from [111].

2.3   Brain Slices and OHSC

2.3.1   The Brain

The human brain can be subdivided into 4 principle working units [113], as depicted in fig 2.8.

The spinal cord, which distributes the sensor and motor function to and from skeleton muscles.

The brain stem contains several important fiber pathways and nuclei. It acts as gateway to the spinal cord and connects the cerebellum to the rest of the brain. Furthermore, basic, life-sustaining body functions like cardiovascular control, respiration, consciousness, and sensorimotor functions of the head are provided by the brain stem nuclei.

The cerebellum, that coordinates complex motor control and carries approximately 50 % of all neurons.

Finally, the cerebrum, where the conscious perception of all sensory information and the generation of motor impulses are processed. The conscious mind and the intellect originate here, and long-term memories are processed and stored. The cerebrum can be subdivided into working units. The cerebral cortex, divided by the different lobes: frontal, parietal, occipital and temporal lobe. Beneath the cerebral cortex different brain nuclei are positioned. Buried under the temporal lobe the hippocampus is located [114, 115].
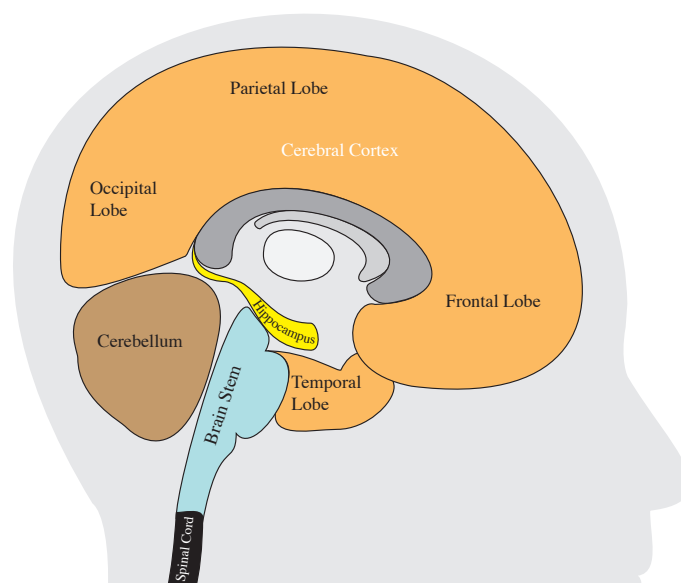

Fig. 2.8 Medial schematic of the brain.

2.3.2   Epilepsy

Epileptic seizures and Epilepsy have been defined by Fisher *et al.* as [116, 117]:

> "An **epileptic seizure** is a transient occurence of signs and/or symptoms due to abnormal excessive or synchronous neuronal activity in the brain."

> "**Epilepsy** is a disorder of the brain characterized by an enduring predisposition to generate epileptic seizures and by the neurobiologic, cognitive, psychological, and social consequences of this condition. This definition of epilepsy requires the occurence of at least one epileptic seizure."

Their definition for epilepsy includes to have a "history of at least one seizure" and "enduring alteration in the brain that increases the likelihood of future seizures". A single epileptic event might therefore be triggered by external factors, such as a trauma, but if the brain does not change from thereon no epilepsy was induced [118]. Enduring alterations affecting the brain's structure and connectivity, which increase the excitability and synchrony of respective neuronal networks, are able to lead to spontaneous, recurrent epileptic seizures. This process is referred to as epileptogenesis.

Epileptogenesis

Epileptogenesis as defined by Pitkänen is [119]:

> "The development and extension of tissue capable of generating spontaneous seizures, including development of an epileptic condition progression after the condition is established."

Epileptogenesis is not completely understood. Epileptogenesis is supposedly triggered by an initial event, i.e. brain injury, febrile seizures or genetic predisposition (see fig. 2.9) [120, 121]. After sufficient alterations in the brain, spontaneous and recurrent seizures develop which is called *chronic* epilepsy. However, epileptogenesis does not stop once chronic epilepsy is reached. The brain continuously alters such that the condition can worsen, for example to mental retardation or drug-resistant epilepsy [122]. Epileptogenesis normally requires several years in human patients to develop a chronic state of epilepsy. In contrast, epilepsy and its generation can also be studied in animal models, in which epileptogenesis takes only a few weeks. Epileptogenesis in these models is triggered artificially, and the brain only needs weeks to develop chronic epilepsy (see fig. 2.9) [123–127].
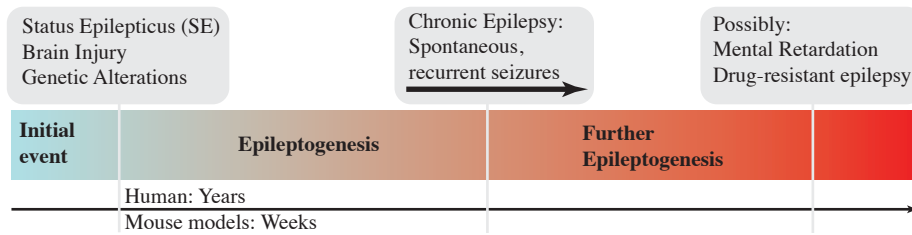
Fig. 2.9 Progression of epilepsy.

2.3.3 Hippocampus

Due to its structure and interconnection with other brain areas, the hippocampus provides spatial and episodic memory as important brain functions. Most of its functionality became evident from a bilateral damage in human patients, leading to anterograde amnesia (inability to form new memories). The dentate gyrus is one of two exclusive brain regions harbouring a neurogenic niche, in which new neurons are generated throughout life - a process which is called neurogenesis[4] [128–130].

The cytoarchitecture of the hippocampus is depicted in fig. 2.10.
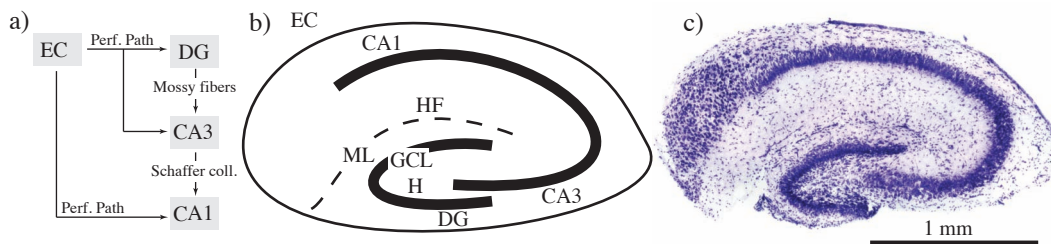
Fig. 2.10 a) Basic circuit, b) schematic and c) Nissl stained cross sectional view of a mouse hippocampus. Abbreviations: EC = Entorhinal cortex, CA = Cornu ammonis, HF = Hippocampal fissure, ML = Molecular layer, GCL = Granule cell layer, H = Hilus, DG = Dentate gyrus.

The hippocampus is organised in a laminar fashion and has a regular organisation of its principal cell layers. A feature of the hippocampus is that most connections are unidirectional. The main signal input is provided by the entorhinal cortex (EC) connected to the dentate gyrus (DG) by the perforant path. The dentate gyrus is presumably the signal gateway to the hippocampus. The dentate gyrus is organised in three layers [131]: 1. The fairly cell-free molecular layer (ML), which has a thickness of about 250 µm in the mouse brain. Dendritic projection of the granule cell dendrites and fibers of the perforant

---

[4]Neurogenesis has additionally been consistently shown in the lateral ventricle [128].

path from the entorhinal cortex are found in the molecular layer.

2. The densly packed granule cell layer (GCL), which has a thickness of approximately 60 μm (4 - 8 neuronal cell rows).

3. The Hilus (or polymorphic cell layer), which is made up of different cell types, including mossy cells.

The Cornu ammonis, which is seperated from the dentate gyrus by the hippocampal fissure (HF), devides the hippocampus into 4 different sectors (CA1 - CA4). CA1 and CA3 are connected via the Schaffer colleterals. The hilus and CA1 are the regions of the hippocampus most prominently affected by cell loss during Status Epilepticus [132, 133].

2.3.4   Organotypic hippocampal slice cultures (OHSC)

Over the last decades, hippocampal slice cultures have been established as biological model for studies of different brain pathologies, for example after brain damage [134, 135] or for neurovascular coupling [136]. An advantage of using hippocampal slices as model system, is that these slices can be cultivated, so that after an initial event, one can monitor the change in the hippocampus continuously over several weeks, which is not feasible with an *in vivo* approach, due to restricted accessibility. Therefore these type of samples are called organotypic hippocampal slice cultures (OHSC). Since it is possible to perform different experiments on each slice culture, or reproduce experiments, this method reduces the number of experiments that need to be done on animals w.r.t. *in vivo* experiments. Additionally organotypic slices have the advantage that they can be obtained from explanted human tissue, and subsequently cultured, to be examined closely [137, 138].

Although acute brain slices are frequently used [139–144], acute brain slices die after 6 h to 8 h, with survival shown for up to 36 h [51]. OHSC are therefore especially interesting for monitoring the epileptogenesis [41, 50]. Applying Kainate, either to the live mammal or, after dissection, to the in vitro brain slice, induces Status Epilepticus (SE), which provokes Epileptogenesis in OSHC (see section 2.3.2) [145–147], which is an established model for medial temporal lobe epilepsy (MTLE) [148]. OSHC are used to model temporal lobe epilepsy (TLE), which can be a result of brain lesion or insult in humans [149–154].

2.3.5 Neurological Staining Methods

The knowledge and skill how to make biological tissue durable for longer time periods, and how to make specific features of tissue, such as cell bodies or axons, visible, has been developed into a core field in biology and medicine over last century (an overview of the neuronal structure is given in fig. 2.11). Since histological staining techniques are a large field, this section will focus on the techniques used in this thesis, and put these techniques into context.

After the *in vitro* experiments and measurements are finished, the brain tissue is fixed, usually using aqueous solutions of 4 % paraformaldehyde (PFA). PFA prevents tissue degradation by creating cross-links on amino groups of proteins within the tissue, and is designed to keep tissue structure intact. To specifically stain certain structures, cellular subtypes or molecules, histological and immunohistochemical stainings methods are applied [155]. An overview of the stainings used in this thesis is given in table 2.2.
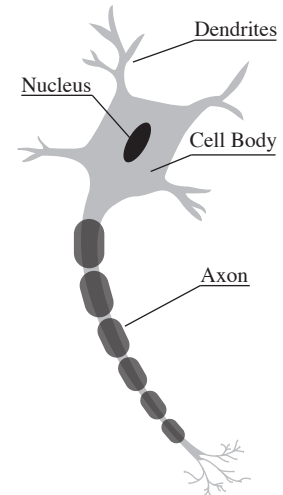
Fig. 2.11 Structure of a neuron.

Histological Stainings

Histological stainings are performed to highlight or to label certain structural features of the tissue. They are frequently used to get an overview of the tissue structure. Different histologic dyes have affinity to different cellular components, and will colourise them accordingly. Tissue, that has been stained this way, can be examined with a transmission light microscope. In this thesis, the Nissl and the Golgi stainings were used. The Nissl stain uses cresyl violet as dye, which binds into the DNA and RNA of the cells, thus staining particularly cellular nuclei and neuronal Nissl bodies violet [155]. The Golgi staining is based on tissue impregnation with silver or mercury salts, forming insoluble complexes which label entire cell bodies (including cell processes) of single cells. The Golgi method, although unspecific, randomly stains only some cells, to which the mechanism is still unknown. The Golgi method stains whole cells with their axons and dendrites. These two stainings methods can be combined to assess morphology and cytoarchitecture [156].

Immunohistochemical stainings

While Nissl and Golgi stainings are chemical dyes and label certain cellular components of all cells, immunohistochemical (IHC) stainings are based on antibody binding and target specific antigenes within tissue samples, i.e. cytoskeletal proteins, certain membrane

Table 2.2 Stainings and dyes used within this thesis.

Dye	Target	Specificity	Fluorescent?	Colour
Nissl	Cell nuclei and ribosomes	non-specific (all cells)	No	Violet
Golgi	Entire cells (e.g. axons)	non-specific (random cells)	No	Black
DAPI	Cell nuclei	Cell nuclei vs. Neuronal nuclei	Yes	Blue/green
PI	Cell nuclei	Injured (dead) cells	Yes	Red
DiI	Cell membrane	Entire neurons (DiI take up by physical contact), Time dependent	Yes	Red
ZnT3	granule cell layer	Axons (mossy fibers)	Yes	Red
NeuN	Neurons	Neuronal nuclei	Yes	Green

receptors, or enzymes. These IHC stainings can therefore highlight certain cell types or cell organelles. All IHC stainings used in this thesis are based on secondary antibodies coupled to certain fluorophores, which bind to the antigene-specific primary antibody, and are therfore fluorescent. Since fluorophores have specific wavelengths of absorbed and emitted light, several secondary antibodies coupled to different fluorophores can be used at once within the same tissue section. Hence, multiple antigenes can be detected simultaneously by different combinations of primary and secondary antibodies. This way different characteristics of the tissue fluoresces in different colours, and the different features can be highlighted by filtering the reflecting microscope images.

In this thesis five different stainings are used. The DAPI staining binds into the DNA, thus the cell nuclei are highlighted. However, it fluoresces differently for neuronal nuclei (NeuN) as for other cell nuclei. Thus, neuronal nuclei, reflecting in green, can be distinguished from other cell nuclei, relfecting in blue.

Propidium Iodide (PI) also binds into the DNA, but can only enter through injured cell membranes. Therefore, PI is used to stain the cell nuclei of injured and dead cells only, and is usually colourised in red in this thesis.

DiI is a lipophilic dye which can be used as a tracer to stain for example neuronal projections. In this thesis, DiI was placed as a single crystal into a specific target region to stain the projections into or extending from this region and it is possible to stain for example Schaffer colleterals. Since DiI spreads by passive diffusion throughout the membrane of

labeled cells, the staining of long-range projections is time-dependent [155].

The Zinc transporter 3 (ZnT3) is a specific marker for granule cell axons (the mossy fibers) [157]. NeuN is a protein that is localised in most of the neurons. The NeuN protein can be stained by antibodies such that the signal is only expressed in the neuronal nuclei of the tissue [158].
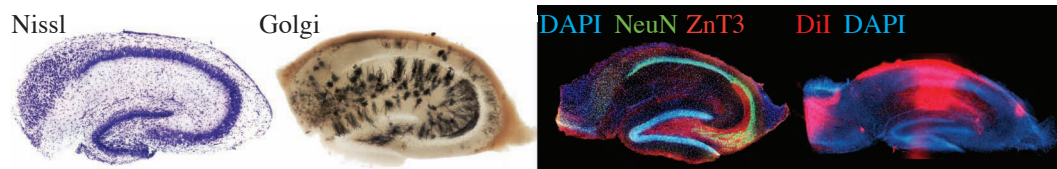

Fig. 2.12 Examples of the different stainings used in this thesis.

Magnetic Resonance Microscopy Detectors

This chapter introduces three different types of MRM detectors useful for resolving brain tissue microstructure and reflects the current state of the art of such detectors. For all detector types, magnetic resonance force micro coils, hollow solenoidal micro coils and Lenz lenses, the development, the manufacturing procedure and their characterisation is described.

3.1   Introduction

Since the beginning of magnetic resonance, increasing the signal-to-noise ratio and decreasing spectral linewidth has been one of the central challenges. Magnetic resonance at its core is very specific, but insensitive. High resolution for example to resolve single cell or cell cluster metabolism is not accessible with clinical scanner systems, since their B_0 field is too weak and their r.f. coils are by far too insensitive to access this kind of information. Small coils with with at least one dimension in the sub-millimetre range are termed micro coils. Micro coils of various dimensions have drawn attention due to their unique performance on multiple occasions in approximately the last two decades. Although their performance outmatches that of bigger coils in some specific applications, i.e. in magic angle spinning [159], reaction kinetics [160] and time critical measurements of mass-limited samples [161], their success is by large limited to a niche market.

3.2   Microcoils - State of the Art

As described in chapter 2.2.2, to obtain the optimal SNR, the coil design needs to meet two conditions. (i) The coil needs to be efficient in B_1 field transmission and (ii) a high

filling factor. In this thesis, by coil the pure inductance is meant without considering the tuning and matching circuitry. The coil needs to efficiently transmit the B_1 field, since according to the principle of reciprocity, where the B_1 field is optimal so is the sensitivity. For small samples, this is achieved by using micro coils [103, 162, 163]. A good overview of the current technology level is given in the papers by Webb [20] and Badilita *et al.* [22]. In principle there are two kinds of coils, surface coils and volume coils. While surface coils have very high local sensitivity, their B_1 field homogeneity is poor, while in general the B_1 field homogeneity of volume coils that surround the sample, i.e. solenoids, is significantly better, and thus having potentially better spatial resolution.
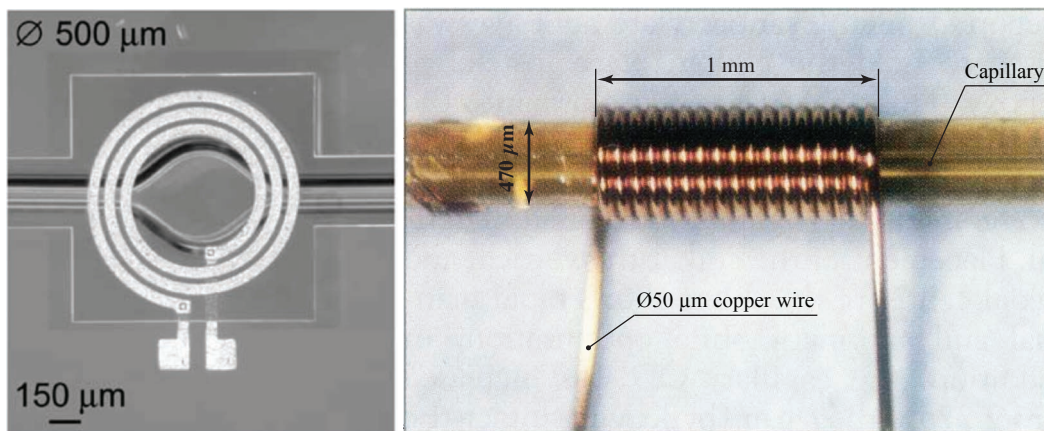
Fig. 3.1 Left: A spiral surface micro coil (image reprinted with permission from [164]). Right: Hand-wound solenoidal micro coil as introduced by Olson *et al,*. Reprinted with permission from [165]. The labels have been added.

From a manufacturing point of view, the manufacturing methods for 2D micro coils are far more mature than for solenoidal micro coils. Especially the use of classical MEMS manufacturing techniques, such as lithography, dry and wet etching were pushed by the semiconductor and sensor industry to reliable, high yield, high resolution and cost efficient technologies [166, 167]. A variety of MR and NMR micro coils were manufacturing using classical MEMS techniques. Surface micro coils can be manufactured using classic MEMS technology, with feature sizes in the single digit micrometre range. These type of spiral micro coils have been put forth by Massin *et al.* [164, 168], Eroglu *et al.* [169] and van Bentum *et al.* [101], with coil diameters down to 500 μm (see fig. 3.1) and feature sizes down to 30 μm . With these coils, MR microscopy down to 3 μm spatial resolution is possible [25], which lead to its commercialisation by Bruker BioSpin. Other micro coils manufactured similarly, have been used in Helmholtz configuration [170, 171] for better field homogeneity, on flexible substrates [172, 173] for more versatility, for on-chip

applications [19], and as described by Moore *et al.* [174] not only used as transceive coils, but additionally used as gradient coils. These coils allow for high integration levels, since they bare the potential to be directly merged with CMOS technology, which allows on chip data processing [175–177].

While surface micro coils have been made available widely for commercial MR systems, only few volume micro coils can be purchased commercially. One reason for volume coils being commercialised rarely, is their manufacturing and specifically the miniaturisation is a lot more tedious, than with surface micro coils. The manufacturing techniques for true 3D solenoidal micro coils did not benefit from the huge industry push as 2D micro coils did. Most solenoidal coils used in NMR and MRI are unique hand wound coils. It has been shown for volume micro coils, that miniaturising them, can increase the mass sensitivity of MR spectroscopy manifold. Probably the most prominent publication and demonstration of the usage of micro coils, especially for mass-limited and low volume samples, was published by Olson *et al.* [165, 178], as depicted in fig. 3.1. This publication showes a 130-fold increase in sensitivity over conventional 5 mm diameter MR coils. Hand made solenoidal micro coils were since used to record NMR spectra [36], high-resolution MR images [179] and functional MR images [39] of single cells. The type of volume micro coils used for these kind of measurements, are generally unique hand wound micro coils, that do not follow manufacturing technology transferable to high yields or mass production. It is also difficult to wind solenoidal micro coils with a defined interwinding pitch, which would open up the possibility of using some advanced MR spectroscopy methods, such as dynamic nuclear polarisation and could increase B_1 homogeneity further.

Especially for miniaturisation of micro coils, surface coils are easier to manufacture since they are essentially 2D dimensional structures. This, however, is not the case for solenoidal coils. There are approaches, to manufacture pseudo-solenoids, by 2.5D manufacturing with multilevel lithography, as has for example been put forth by Klein *et al.* [180]. A more sophisticated approach to manufacture solenoidal micro coils, is to structure a coil directly onto a capillary. An approach to this was introduced by Rogers *et al.* [181], who used microcontact printing of copper on a 324 μm diameter capillary. As similar approach is the use of laser-lathe lithography to pattern copper on glass capillaries [69, 182–184] with coil diameters down to 100 μm. An alternative route to manufacture solenoidal micro coils, was established by Kratt *et al.*, using an automatic wire bonder to wind coils around support structures, with diameters down to 150 μm (see fig. 3.2) [16, 17, 185, 186]. This technology has been pushed further in the authors work group to a variety of devices, such as micro coils with an integrated fluidic network [23], micro Helmholtz coils [21, 187], and phased array of micro coils [18, 188].
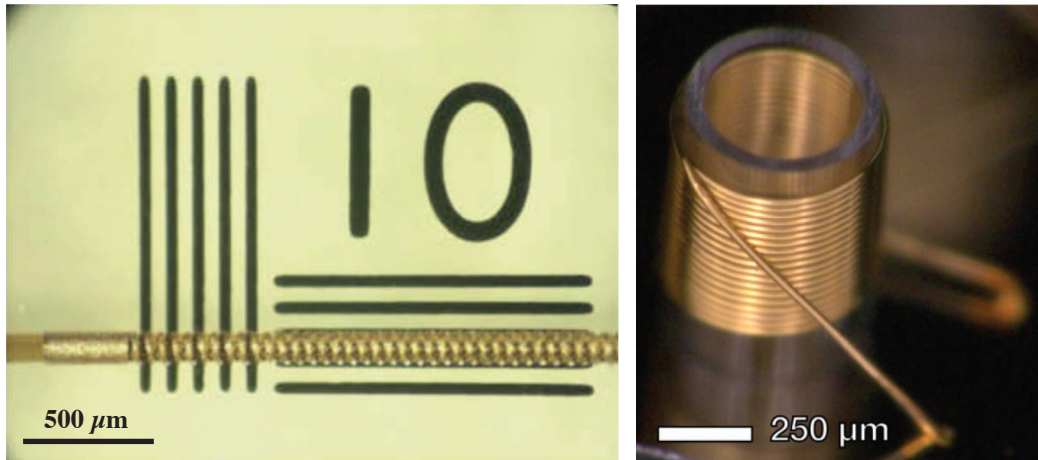
Fig. 3.2 Left: A micro coil manufactured by laser-lathe lithography with a diameter of 100 μm. Image reprinted with permission from [182]. Right: A solenoidal micro coil manufactured by winding with a wire bonder. Image reprinted with permission from [185].

An overview of a variety of solenoidal micro coils manufactured by hand, by wire bonding, by laser-lathe lithography and planar micro coils is given in table 3.1. The normalised limit-of-detection (nLOD) was scaled for all coils to the 600 MHz value (scales with $\omega_L^{7/4}$ [22]). As can be seen from the nLOD-values, hand-wound solenoids potentially show the lowest nLODs, where other solenoids and planar coils perform inferior. Wire bonded are the closest to hand-wound micro coils in shape, since wire bonding uses coil wire with round cross section that is continuously wound around a support structure. Therefore, it is assumed that wire bonded coils have the potential to show best performance, while being high precision and fully integrate-able with other MEMS processes.

For gaining the optimal SNR, the second condition to meet, is to maximise the filling factor of the r.f. coil. This is significantly easier for surface micro coils, since the sample can simply be positioned directly on top of the coil, covering the coil up to a certain height, resulting in a high filling factor. With volume micro coils, this can be much harder to achieve, especially when down-scaling the coils. The micro solenoids are wound around a support structure, that needs to bear the force applied to it while winding. This requires a minimum thickness of the hollow post, or the glass capillary the wire is wound around. As the coils are down-scaled, the relative volume is occupied by the support structure, rather than the sample itself, leading to lower filling factors and thus lower sensitivity.
Kratt *et al.* manufactured wire bonded coils around x-ray lithography structured PMMA posts and SU-8 posts [185, 186]. The minimum wall thickness the hollow PMMA posts

Table 3.1 Characteristics of a variety of hand-wound (h.-w.), manually wound (m.-w.), wire bonded (w.b.), laser-lathe (la.-l.) solenoidal and planar micro coils. Values taken and complemented from [22].

Coil Type	Sample Volume μl	Resolution ppb	nLOD at 600 MHz nmol s^{-1}	Reference
H.-w. solenoid	0.005	2	0.13	Olson *et al.* [165]
H.-w. solenoid	$4 \cdot 10^{-8}$	1700	0.36	Ciobanu *et al.* [189]
W.b. solenoid	$6.4 \cdot 10^{-5}$	1700	16.5	Badilita *et al.* [16]
W.b. solenoid	0.02	16	1.05	Meier *et al.* [23]
La.-l. solenoid	0.03	2.33	141.1	Rogers *et al.* [181]
La.-l. solenoid	0.08	17000	6.21	Demas *et al.* [183]
M.-w. solenoid	0.0001	2600	7.0	Seeber *et al.* [190]
Planar	0.03	300	20.9	Massin *et al.* [164, 168]
Planar	0.47	300	262	Massin *et al.* [164, 168]
Planar	0.393	12.4	13.8	Trumbull *et al.* [191]
Planar	0.57	100	163	Wensink *et al.* [160]
Planar	330	400	92000	Renaud *et al.* [192]
Planar	0.5	50	12.3	Syms *et al.* [170]
Planar	1.2	7.5	22	Ryan *et al.* [19]

was 20 μm, which leads to a filling factor of 36 % for 100 μm posts. Since x-ray lithography is an expensive technology, an alternative process is the use of SU-8 posts, which needs thicker walls of at least 60 μm for the wire bonding process to work. Therefore very small diameters (i.e. 100 μm) are not possible, and even for coils with 1 mm diameter, the filling factor is only 77 %. Especially for miniaturisation of MR detectors based on solenoidal micro coils, this severly limits progress. Thus this thesis approaches this challenge by winding coils around structures that can be removed after winding, leading to high filling factors.

3.3 Micro coils for Magnetic Resonance Force Microscopy

3.3.1 Magnetic Resonance Force Microscopy

Magnetic Resonance Force Microscopy (MRFM) is an extremely high spatial resolution technique, where detection of the spin of a single electron has been shown [193]. MRFM combines magnetic resonance and a set-up similar to an Atomic Force Microscope (AFM). AFMs rely on micro cantilevers (AFM tip), that are scanned across the surface of a sample. The AFM tip is pulled towards the surface by Van der Waals and capillary forces, while at the same time it is pushed away from the sample according to the Pauli exclusion principle

and Coulomb's law. These force lead to an equilibrium, described by the Lennard-Jones-potential, where the AFM tip does not touch on the sample, but is dragged in close proximity to it. The deflection of the AFM tip is then measured capacitively or or optically via quadrature photo diodes, leading to sub nanometre resolution. Similarly, in MRFM a micro cantilver is used, on which the sample is positioned. The sample is subjected to a magnetic field gradient passively applied by the vicinity of a ferromagnetic material, or actively applied by a micro coil [1]. The whole set-up is placed into a strong static magnetic field B_0, as is the case in a magnetic resonance scanner, to polarise the spins. When in the gradient field, the spins with positive gyromagnetic ratio are pulled towards the stronger magnetic field. By applying an r.f. field at the Larmor frequency, the spin orientation is periodically flipped which induces an oscillating magnetic force in the cantilever. The resonance frequency of the cantilever is matched to the Larmor frequency of the spins to be observed in the sample. The cantilever thus experiences a force at its mechanical resonance, causing the cantilever to vibrate. The vibration is measured using a laser and a quadrature detector (as used by the AFM), and its amplitude is proportional to the number of spins present in the slice of the sample excited by the r.f. field. Slice thickness in the sample is a function of the magnetic field gradient amplitude, similar to spatial encoding in MRI (see section 2.1.2) [194].

During the course of this thesis, micro coils used as gradient and read-out coils for MRFM were manufactured. With an inner diameter of 100 μm and a height of up to 300 μm, these micro coils are at the current technologic limit of wire bonded micro coils and are the smallest wire bonded coils manufactured yet [195]. The dimensions and layout of the dies on which the coils were produced, were subject to specific constraints imposed by the MRFM set-up. The MRFM set-up includes two of the micro coils used for their gradient fields, which are arranged at a 90° angle, to achieve 3 dimensional imaging of the MRFM sample. Therefore, the posts, around which the micro coils were wire bonded, had to be positioned right at the edge of the die (see fig. 3.3). The process developed to manufacture these coils, which overcame some challenges accompanied with the downscaling, is described in the following paragraph.

3.3.2   Process Description MRFM Coils

Two sets of micro coils for MRFM were manufactured. The first batch with silicon (SI) and the second batch with Pyrex® glass as substrate. Manufacturing was based on a cleanroom

---

[1]An optional approach is to position the micro coil or the ferromagnetic material on the micro cantilever, while scanning across the sample.

process, with an overview of the process parameters given in table 3.2 and depicted in fig. 3.3. There were 10 principle manufacturing steps explained in the following section.
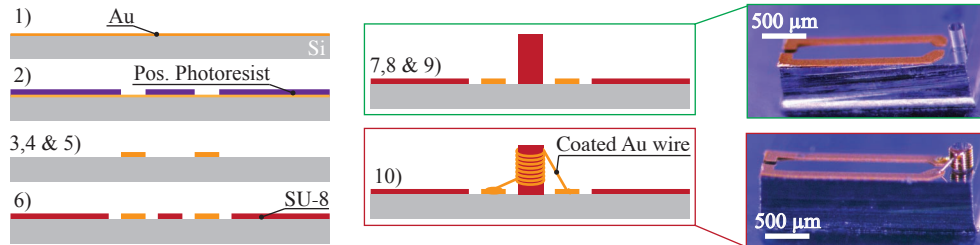

Fig. 3.3 Process flow for MRFM microcoils

First, a seed layer, consisting of 50 nm Chromium (Cr) and 200 nm Gold (Au) were sputtered onto the substrate with a UNIVEX 500 sputtering machine (*Leybold GmbH, Germany*) (1). A 20 µm thick AZ 40XT positive photoresist layer (*Microchemicals GmbH, Germany*) was lithographically structured using the Maskaligner MA6/BA6 (*Suss MicroTec, Germany*) (2) with an exposure dose of 4.9 mW for 120 s according to the protocol given in Appendix D.1 and developed for 5 min in AZ 726 MIF (*Microchemicals GmbH, Germany*). The structured AZ 40XT was used as mould for 15 µm thick gold electroplating (3) of the wire bond pads and interconnects to the MRFM periphery (for chip layout see Appendix F). After stripping the AZ 40XT mould in a TechniStrip® NI555 (*Microchemicals GmbH, Germany*) bath for 5 min (4), the seed layers are removed by a 5 min gold etch in TechniEtch^{TM} ACI2 (*Microchemicals GmbH, Germany*) a 1 min chromium etch in TechniStrip Cr01 (*Microchemicals GmbH, Germany*) to avoid electrical short-circuits of the bond pads and interconnects (5). An 8 µm SU-8 3005 (*MicroChem Corp., USA*) adhesion layer is patterned with the Maskaligner MA6/BA6 (*Suss MicroTec, Germany*) with i-line filter and an exposure dose of 200 mJ cm^{-2} in 100 s onto the substrate (6), according to the recipe given in Appendix D.2. This adhesion layer leaves the bond pads and interconnects free, but increases adhesion of the 100 µm diameter SU-8 2150 (*MicroChem Corp., USA*) posts. This step was key, to avoid the posts from chipping off during the wire bonding step. For the SU-8 2150 posts patterning, the substrate was prebaked for 10 min at 95 °C on a hotplate to avoid residue humidity. The substrate was subsequently cleaned for 2 min in a 600 W O2 plasma machine Matrix model 205 (*Matrix Integrated Systems Inc., USA*). After O2 plasma cleaning, the substrate was placed onto a hotplate at a constant temperature of 60 °C. The SU-8 2150 (*MicroChem Corp., USA*) was applied by constant injection (3 ml SU-8 2150 for 300 µm layer thickness on a 100 mm diameter substrate). The softbake of the SU-8 2150 layer was done on a levelled hotplate for 7 min at 65 °C followed by a 1 °C min^{-1} temperature ramp to 95 °C where the substrate was baked for 8 h.

Table 3.2 Overview of the manufacturing process.

Step	Process	Parameters
1	Seed Layer sputtering	Cr/Au 50nm/200 nm
2	Photoresist mould AZ 40XT	20 µm thick, details Appendix D.1
3	Gold Electroplating	15 µm thick
4	Stripping of AZ 40XT	5 min in AZ 726 MIF
5	Au/Cr seed layer removal	5 min TechniEtch^{TM} ACl2, 1 min TechniStrip CR01
6	SU-8 3005 Adhesion Layer	8 µm, details see Appendix D.2
7	SU-8 2150 Post Layer	200 µm thick, details Appendix D.3
8	O2 Plasma purge (residue removal)	2 min at 600 W
9	Wafer Dicing	Feedrate: $2\,\mathrm{mm\,s^{-1}}$
10	Wirebonding	Heater plate at 125 °C Ball bond: IF: 500 mN, BF: 250 mN, US: 60 % for 30 ms Wedge Bond: IF: 8 mN, BF: 450 mN, US: 35 % for 3 ms

The levelled hotplate and the slow temperature ramps avoids stress, bubble formation from evaporating solvents and flattens the 300 µm thick SU-8 2150 layer. The SU-8 2150 was patterned with the Maskaligner MA6/BA6 (*Suss MicroTec, Germany*) with i-line filter and an exposure dose of $600\,\mathrm{mJ\,cm^{-2}}$ for 250 s (7). The spost exposure bake was done on a hotplate for 7 min at 65 °C followed by a $1\,\mathrm{°C\,min^{-1}}$ temperature ramp to 95 °C where the substrate was baked for 2 h. The SU-2150 was developed for 45 min and purged in fresh diacetone alcohol based SU-8 developer (*MicroChem Corp., USA*) for 5 min and 99.8 % isopropanol Rotisolv® Pestilyse®(*Carl Roth GmbH & Co. KG, Germany*) for 5 min. After SU-8 structuring, the whole wafer is purged in an O2 plasma for 2 at 600 W in an STS Multiplex Reactive Ion Etching (RIE) machine (*SPTS Technologies Inc., UK*) to remove residual resist from the bond pads (8). The wafer is then diced with a DAD-321 wafer saw (*Disco Corp., Japan*) at a feed rate of $2\,\mathrm{mm\,s^{-1}}$ with a 200 µm thick diamond blade to chips of 2x5 mm^2, with the posts placed at the edge of the chip (9), as depicted in fig. 3.3. In the last step, 25 µm diameter insulated gold wire is wirebonded around the posts with an automated wire bonder 3100plus (*ESEC, Switzerland*), forming a micro coil with 8 windings, without interwinding spacings (10). Wirebonding was done at 125 °C and the ball bond was formed with an impact force of 500 mN, a bond force of 250 mN at 60 %

ultrasound power and a bond time of 30 ms. The wedge bond is done with an impact force of 8 mN, a bond force of 450 mN at 35 % ultrasound power and a bond time of 3 ms respectively.

The most critical step in this process, is the wirebonding step. If no SU-8 adhesion layer is used, the SU-8 posts chip off the substrate (see fig. 3.4 a). When the height of the SU-8 posts is not controlled properly, and their height is less than aimed for, the top windings of the wire bonded coil do not form a coil, as can be seen in fig. 3.4 b. And finally, if the bond pads are not cleaned properly from the resist residue (e.g. no plasma etch), the wire bond will not be in intimate contact with the bond pads and detach as shown in fig. 3.4 c. However, by solving these issues, it is possible to manufacture extremely small micro coils, which are true solenoids, as depicted in fig. 3.4 e-f.
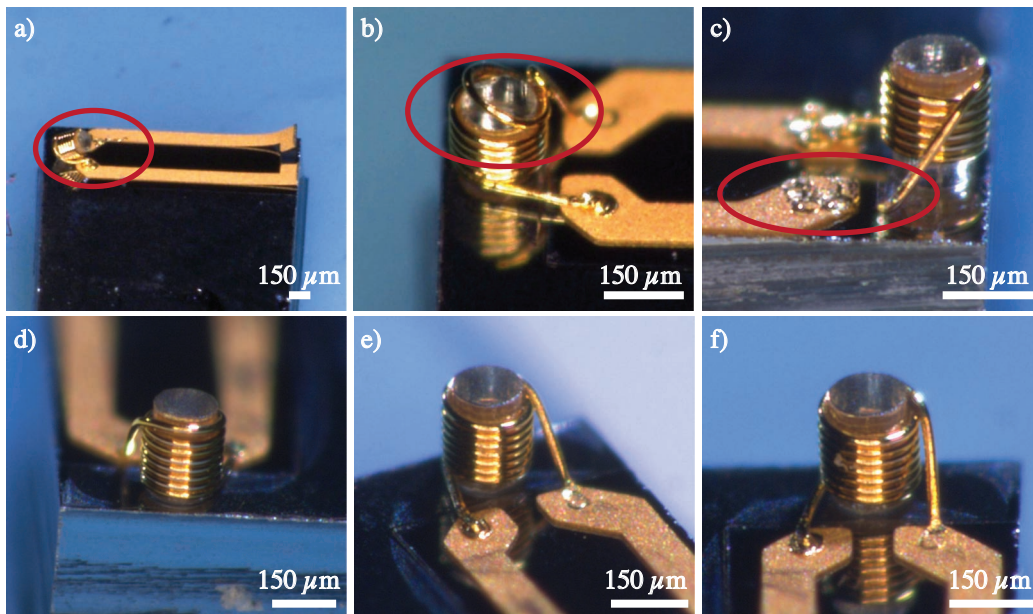
Fig. 3.4 Failure mechanisms during wire bonding of small micro coils. a) If the adhesion of the wire bond post is not promoted by an adhesion layer, the posts chips off during wire bonding. b) If the SU-8 post height is too low, the top winding(s) do not form a coil. c) If the bond pads are not clean, the wire bond rips off. A micro coil, manufactured with the described process. d) front view, e) side-view and f) back side.

3.3.3   Results MRFM Coils - Proof of Concept

All images and measurements described in this proof of concept section were recorded by Sebastian Schnoz at the Laboratory of Physical Chemistry, ETH Zürich headed by Prof. Dr. Beat Meier.

For the evaluation of the working principle of the micro coils for MRFM, the coil chips were mounted into a custom made MRFM setup operated in an 89 mm diameter wide bore NMR spectrometer (*Oxford Instruments plc, UK*) at a static field strength of 5.87 T (250 MHz 1H frequency). In this set-up, depicted in fig. 3.5, two MRFM chips were adjusted in a 90° angle w.r.t. each other. The two micro coils are brought into close vicinity of the MRFM cantilever, and at the tip of the MRFM cantilever a crystal of Ammonium sulfate ($(NH_4)_2SO_4$) is positioned as sample. This crystal is relatively large and only acts to test the coil set-up, while in future measurements the sample will be significantly smaller than the coil diameter. For the proof of concept a one dimensional image of the Ammonium sulfate crytal is recorded. Therefore, the coil opposite of the cantilever tip (MRFM Chip 2) is used to excite the MRFM signal, while the other chip (MRFM Chip 1) is used for the gradient field to decode the spatial origin of the signal. A lock-in amplifier is used to distinguish noise from MRFM signal. Therefore, the MRFM signal is detected in-phase (real channel) with the applied r.f. field, which is the phase the cantilever oscillates in. The 90° shifted signal (imaginary channel) then is the noise signal not susceptible to the cantilever oscillation. The signal is read out with 4 quadrant diode and the result of this measurement is shown in fig. 3.5. For multidimensional MRFM measurements, MRFM Chip 1 decodes the X-direction and MRFM Chip 2 decodes the Y-direction, while the Z-direction is decoded by a magnetic cylinder (not shown in the image).
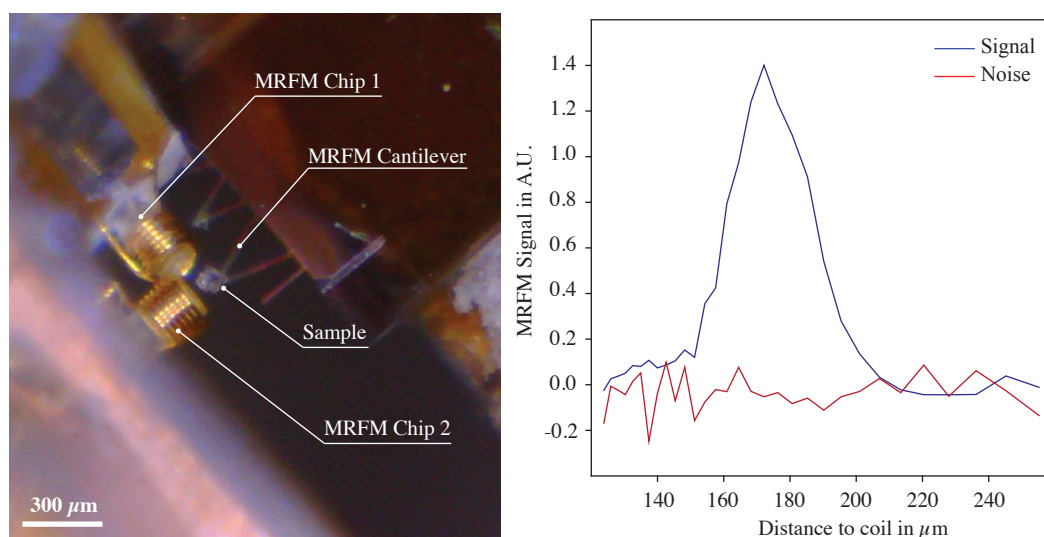

Fig. 3.5 Left: Photo of the the MRFM measurements setup, with two of the manufactured MRFM chips built in. The MRFM cantilever and the Ammonium sulfate crystal (sample) are clearly visible. Right: MRFM measurement recorded with the depicted setup.

3.4 Hollow Micro Coils

A significant part of this section on hollow micro coils was presented in [RK5[a],RK23[b]].

---

[a]Contributions: *RK:* Process development, hardware manufacture and design, MR data acquisition, analysis and interpretation, Manuscript concept and writing. *AM:* Process development, proofread manuscript. *JGK:* Data interpretation, proofread manuscript. *OGG:* Process development, data interpretation, proofread manuscript.

[b]Contributions: *RK:* Process development, hardware manufacture and design, MR data analysis/interpretation, Manuscript concept and writing. *OGG:* Hardware design, MR data acquisition, proofread manuscript. *JH:* MR data acquisition. *JGK:* Concept and proofread manuscript, data interpretation

During the course of this thesis, manufacturing procedures for solenoidal micro coils were developed, that address both in section 3.2 mentioned challenges, making the manufacturing less tedious with higher yield, and maximising the filling factor. A solution to approach commercialisation of the solenoidal micro coils, is the use of a wire bonder, as has been introduced by Kratt *et al.* [186]. In their publications, they used a wire bonder to wind coils around a solid structure, made either from SU-8 photoresist, or from PMMA [16, 186]. While wire bonding solves the winding part of the challenge, it does not account for the decreasing filling factor with decreasing coil diameter. This section introduces manufacturing procedures to produce micro solenoids with the wire bonder and a support structure used as sacrificial layer to be removed after the coil has been fixed from the outside (fig. 3.6).
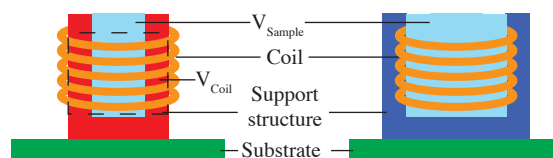
Fig. 3.6 Solenoidal microcoils with internal and external support structures. Image reprinted from [196].

3.4.1 Version 1 - Manufacturing by dip coating of capillaries

In MEMS manufacturing technologies, the use of sacrificial layers are widely used. Many of the sacrificial processes use silicon dioxide or porous silicon as sacrificial layers, which are selectively etched with specialised machines and toxic solvent, such as potassium hydroxide (KOH), sodium hydroxide (NaOH) or hydrofluoric acid (HF) [197–200]. Therefore the use of polymers as sacrificial layer is increasing for different MEMS processes. These polymers do not need toxic solvents, but rely on solvents commonly available in

most laboratories, such as water and acetone. Bagolini *et al.* [201] spin coated a $4\,\mu m$ polyimide (PI) layer onto a silicon substrate. While PI endures for example acetone and HF, they used an O_2-plasma release the PI layer. Patel *et al.* [202] patterned a thick SU-8 layer on top of a silicone layer. Since the adhesion between SU-8 and silicone is low, it was possible to peel off the SU-8 structures. Neutralised Polyacrylic Acid (PAA) is highly soluble in water. Linder *et al.* [203] showed the use of spin coated PAA as sacrificial layer, with very high etching rates. However, in the authors experience, PAA is not applicable to be used with voluminous structures, due to crack formation, but only for very thin films. Another water-soluble polymer, Polyvinyl Alcohol (PVA), was used by Ferrell *et al.* as 750 nm sacrificial layer [204]. This material also works for more voluminous structures, and can be cast and extruded under elevated temperatures, with lower shrinkage than PAA. These publication all use polymeric sacrificial *films*, rather than thick structures, so these processes are not directly transferable to produce posts $> 100\,\mu m$ height.

Manufacturing procedure dip coated hollow micro coils

The manufacturing procedure depicted in fig. 3.7 is based on a 1.5 mm thick PCB with FR4 base material with a pre-coated $35\,\mu m$ thick copper layer (*Bungard Elektronik GmbH & Co.KG, Germany*). Conductive tracks for interconnection, tuning and matching to the MR system and for wire bonding are made by standard PCB lithography. Therefore, a mask layer was printed with a resolution of 600 dpi on Herlitz semi-transparent paper (*Pelikan GmbH, Germany*) with an office laser printer. After 2 min UV light illumination in a Hellas exposure machine (*Bungard Elektronik GmbH & Co.KG, Germany*) the copper wet etching was done in a bench top bubble etch tank PA104 (*Mega Electronics Ltd., UK*) for 15 min at $45\,°C$ in Sodium persulfate - water solution ($220\,gl^{-1}$) (1) and $5\,\mu m$ thick gold electroplating of the wire bond pads. An $800\,\mu m$ hole was drilled into the PCB (2). Minicaps® capillaries (*Hirschmann Laborgeräte GmbH & Co.KG, Germany*), with an outer diameter of $760\,\mu m$ were dip coated with neutralised Polyacrylic Acid (PAA). PAA with a molecular weight of ≈ 100000 with $35\,wt-\%$ in water (*Sigma Aldrich Chemie GmbH, Germany*), was mixed under constant stirring with a saturated sodium hydroxide (NaOH) solution (*Sigma Aldrich Chemie GmbH, Germany*) until neutralisation was achieved [203]. PAA acts as water-soluble sacrificial layer (3). Subsequently the dip coated capillaries were inserted into the hole of the PCB, drilled with a CNC mill 4030 (*isel Germany GmbH, Germany*) with parameters given in appendix E.2 (4). The set-up is dried for 24 h at room temperature, such that the capillaries are glued to the PCB by the PAA.
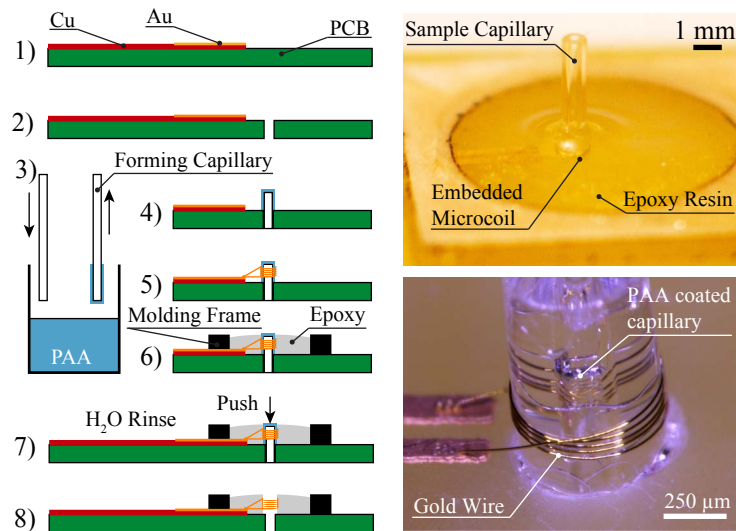
Fig. 3.7 Hollow coils first trials. Image adapted from [205].

After acetone/isopropanol clean and a 2 min, 100 W, 40 kHz O_2 plasma flush in a STS Multiplex RIE (*SPTS Technologies Inc., UK*), coils were wound around the PAA coated capillaries with an automatic wire bonder 3100plus (*ESEC, Switzerland*) (5). Wirebonding was done at 125 °C and the ball bond was formed with an impact force of 700 mN, a bond force of 350 mN at 80 % ultrasound power and a bond time of 40 ms. The wedge bond was done with an impact force of 800 mN, a bond force of 500 mN at 38 % ultrasound power and a bond time of 25 ms respectively. The coils are made from an 25 µm insulated gold wire and 5 windings with an interwinding spacing of 50 µm (see fig. 3.7). As depicted in fig. 3.7, a casting frame was glued onto the PCB and the frame including the coil was filled with epoxy resign (*UHU Endfest plus, UHU GmbH & Co KG, Germany*) and cured for 3 h at room temperature (6). The whole set-up is then placed into deionised water for 6 h to dissolve the PAA sacrificial layer (7), and then the capillary can smoothly be removed achieve a hollow solenoidal micro coil (8). Since this process relies on the coating of PAA, and PAA has a very high solubility in water, the capillary can easily be removed. This works smoothly without high force, which decreases the potential to hurt the coil windings that are directly at the interface to the PAA. However, since this process relies on glass capillaries assembled by hand to the PCB, that are pinched off with pliers, the wirebonding posts are prone to break during this step and/or they are tilted w.r.t. the PCB, and thus donot form optimal coil yokes for the wire bonding step.

Results of dip coating manufactured hollow micro coils

Micro coils manufactured with this process were characterised by acquiring an MR spectrum of a de-ionised water sample ($1\,\mathrm{gl}^{-1}$ $CuSO_4$), and MR images of the whole coil filled with de-ionised water and a capillary inserted into the coil with the same sample. The results of these measurements are depicted in fig. 3.8. All measurements were acquired with a Bruker BioSpec Avance III vertical bore spectrometer with a micro 5 probe imaging set, at a static magnetic field strength of $11.7\,\mathrm{T}$, which sets the 1H larmor frequency to $500\,\mathrm{MHz}$. The full-width half maximum line-width was determined to be at $0.055\,\mathrm{ppm}$, which corresponds to $27.5\,\mathrm{Hz}$ at $500\,\mathrm{MHz}$. With an active sample volume of $15.4\,\mathrm{nl}$ a normalised mass limit of detection of $\mathrm{nLOD_m} = 33\,\mathrm{nmol}\sqrt{s}$ was determined.

The MR images were acquired with a standard non-RF-spoiled FLASH sequence. The image SNR_i was determined for a capillary inserted into the micro coil, with a repetion time $T_R = 120\,\mathrm{ms}$, an echo time $T_E = 4.4\,\mathrm{ms}$ and a flip angle of 30°. The slice thickness was set to $100\,\mu\mathrm{m}$, and the field of view of $\mathrm{FOV} = 0.5\,\mathrm{x}\,0.5\,\mathrm{cm}^2$ and an image size of $\mathrm{MTX} = 512\,\mathrm{x}\,512$ sets the in-plane resolution to $9.8\,\mathrm{x}\,9.8\,\mu\mathrm{m}^2$. With 8 averages, the image SNR is the computed to be $\mathrm{SNR}_i = 16.6$.

For the MR image where the whole coil volume was filled with de-ionized water ($1\,\mathrm{gl}^{-1}$ $CuSO_4$), we used $T_R = 300\,\mathrm{ms}$, $T_E = 3\,\mathrm{ms}$, a flip angle of 30°, a slice thickness of $300\,\mu\mathrm{m}$, a $\mathrm{FOV} = 0.3\,\mathrm{x}\,0.3\,\mathrm{cm}^2$ and an image size of $\mathrm{MTX} = 256\,\mathrm{x}\,256$ yielding a resolution of $11.7\,\mathrm{x}\,11.7\,\mu\mathrm{m}^2$. The image SNR was therefore calculate to be $\mathrm{SNR}_i = 9.6$.
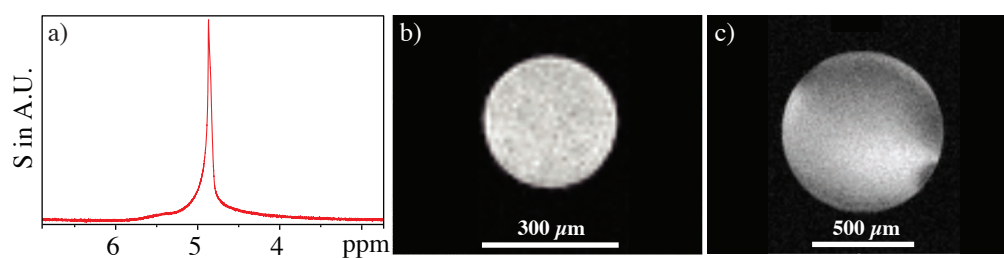
Fig. 3.8 MR measurements of a micro coil, manufactured by dip-coating of capillaries. Left: An MR spectrum of pure de-ionized water with FWHM = $0.055\,\mathrm{ppm}$. Middle: MR image of the micro coil with a capillary inserted, with $\mathrm{SNR}_i = 9.6$. Right: MR image of the micro coil volume completely filled with de-ionized water yielding $\mathrm{SNR}_i = 16.6$.

3.4.2 Version 2 - Manufacturing by a two solvent process

Two central issues emerged while manufacturing the hollow micro coils with the dip coating process. The PAA film showed an non-uniform thickness which impedes reproducible coil diameters and shapes. Additionally, the PAA peeled off the capillaries regularly, which

lowers manufacturing yield significantly. Both of these issues were circumvented by wire bonding around coil pillars that were cast in bulk material.

Substrate preparation

Although many different substrates are compatible with the two-solvent process, its choice was limited by constraints imposed by MRS and MRI. Mismatches in magnetic susceptibility of substrate and water lead to line broadening and imaging artefacts. A 100 mm diameter Pyrex wafer substrate was selected, with a thickness of 500 µm. Alternatively, other materials, such as silicon or printed circuit boards, would be feasible, but, due to their susceptibility mismatch with water, are less opportune for the MR environment.
A 50 nm chromium adhesion layer and a 150 nm gold electroplating starting layer were deposited onto the Pyrex substrate by chemical vapor deposition in a UNIVEX 500 machine (*Leybold GmbH, Germany*). Then, 20 µm AZ 40XT (*Microchemicals GmbH, Germany*) positive photo resist was spin coated, lithographically patterned with a MA/BA6 Maskaligner (*Suss MicroTec, Germany*) and developed for with AZ 726 MIF (*Microchemicals GmbH, Germany*), according to the recipe given in appendix D.1 and . After subsequent electroplating of 15 µm gold layer, the photo resist was stripped for 5 min with TechniStrip NI555 (*Microchemicals GmbH, Germany*) and the substrate cleaned with 99.9 % acetone, 99.8 % isopropanol (both Rotislov® Pestilyse® *Carl Roth GmbH, Germany*) and DI-water. Discrete electrical contacts of the electroplated structure was ensured by a 5 min gold etch in TechniEtch^TM ACI2 (*Microchemicals GmbH, Germany*) and a 1 min chromium etch in TechniStrip Cr01 (*Microchemicals GmbH, Germany*) of the adhesion and electroplating starting layer. The substrate was then diced with a DAD-321 wafer saw (*Disco Corp., Japan*) and a feed rate of $2\,\mathrm{mm\,s^{-1}}$ to chip size. The through hole necessary for further processing was manufactured by powder blasting with a fine sandblasting unit model basic classic (*Renfert GmbH, Germany*), while the rest of the chip was masked by structured aluminium milled with a CNC mill 4030 (*isel Germany AG, Germany*) and the milling parameters given in appendix E.3.

Two-solvent process

The key materials used in this process are PVA and PMMA as sacrificial material, and acetone and water as etchants. To evaluate sufficient cross selectivity, PVA was submerged in acetone, and PMMA was submerged in water. Both set-ups remained for 72 h at room temperature. An inspection with an optical microscope indicated no visible changes in
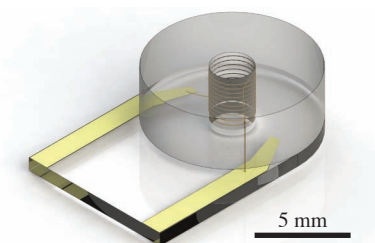
Fig. 3.9 Rendered CAD model of the externally supported microcoil mounted on the Pyrex substrate (designed and rendered with Solidworks 2014 (*Dessault Systems SE, France*)). Image reprinted from [196].

either of the materials. Thus this material-etchant combination was deemed fit for the following processing steps summarised in table 3.3.

An 1 mm thick FR4 carrier board (*Bungard Elektronik GmbH, Germany*), with CNC milled cavities (parameters see appendix E.2) acting as anchors for the subsequent PVA cast, was prepared. A PMMA mould, with cavities for PVA casting and holes for the application of precision pins was manufactured with a CNC mill model 4030 (*isel Germany GmbH, Germany*) with parameters given in appendix E.1. The PMMA mold was mounted onto the FR4 carrier board by a simple mechanical press, that clamps the PMMA to the FR4 board to ensure intimate contact, while the alignment was ensured by the use of precision pins.

For casting a PVA mixture was prepared by mixing 50 % PVA filament (*Makerbot Industries LLC, USA*) with 50 % DI-water by weight. After sealing the mixture air tight, to avoid water evaporation, it was stirred for 12 h at 75 °C. The PVA mixture was subsequently dispensed with a DX250 dispenser (*Esska.de GmbH, Germany*) into the prepared PMMA mould (1) at 75 °C. To avoid bubble formation in the PVA cast, after dispensation, the whole set-up was dried in a pressure chamber for 24 h at 2.5 bar and 55 °C.

After drying, the aluminium press was removed. The rest of the set-up (FR4 carrier board, PMMA mould and dried PVA), was submerged in 99.9 % Rotisolv® Pestilyse® acetone (*Carl Roth GmbH, Germany*) (2). Since the overdue PMMA settles at the bottom of the acetone etch bath, the set-up was oriented upside down. Etching of PMMA was finished after 24 h at room temperature followed by a rinse in fresh acetone to remove PMMA residue. The Pyrex substrate chips were glued on the FR4 carrier board by dispensing 6 µl neutralised PAA ($M_w \approx 100000$, 35 wt − % in water, *Sigma Aldrich Chemie GmbH & Co.KG, Germany*), neutralised with saturated NaOH solution (*Sigma Aldrich Chemie GmbH, Germany*) with a pipette under the chip. This was dried for 12 h at 55 °C (3), see fig.3.10.

Table 3.3 Overview of the casting procedure.

| No.	Step (+ Description)	Parameters
1	**Cast PVA posts** FR4-board anchors posts drilled PMMA mould attached with Al press syringe dispensed PVA	mix PVA/water 50/50 wt-% heat mixture to 75 °C fill syringe and dispense dry 24 h at 2.5 bar at 55 °C
2	**Dissolve PMMA mould** Put set-up in Acetone bath bottom up	Acetone bath for 24 h Rinse with clean Acetone
3	**Glue substrate chips** glue substrate chips to PCB with neutralised water-soluble PAA (see [203])	6 µl of neutralised PAA Dry 12 h at 55 °C
4	**Wirebond microcoil** Special frame for substrate fixation	Heater plate at 125 °C Ball bond: IF: 700 mN, BF: 350 mN, US: 80 % for 40 ms Wedge bond: IF: 800 mN, BF: 500 mN, US: 38 % for 25 ms
5	**Cast PMMA support** PDMS form as casting mold seal PDMS mold off by press PMMA = Paladur®	mix powder & fluid for 10 s dispense mixture with syringe cure 12 h at 2.5 bar at 55 °C
6	**Polish PMMA support** Use polishing frame	grain size P180 to P1200 polish 9 µm to 3 µm
7	**Dissolve PVA posts** place set-up in clean water	dissolve 24 h at 55 °C
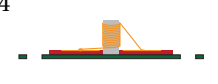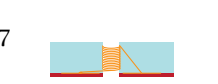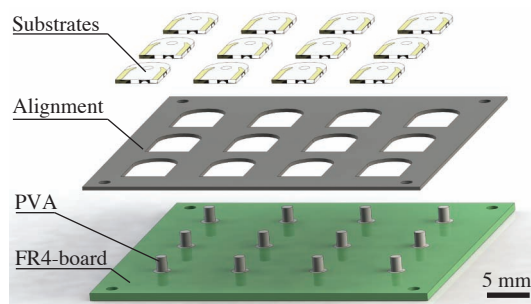
Fig. 3.10 Cast PVA posts on a FR4-board. The substrates are aligned with an aligmnent frame. Image reprinted from [196].

The whole set-up was attached to the wire bonding machine (*ESEC Wire Bonder 3100^{plus}*) with a custom made frame, and aligned with precision pins. Wire bonding was done at 100 °C (4). Wire winding was made with a 25 μm diameter insulated gold wire with 5-8 windings per coil. The ball bond was formed with an impact force of 700 mN, a bond force of 350 mN at 80 % ultrasound power and a bond time of 40 ms. The wedge bond was done with an impact force of 800 mN, a bond force of 500 mN at 38 % ultrasound power and a bond time of 25 ms respectively.Since the wedge bond tends to be weaker than the ball bond, the wedge bond was secured by attaching an additional ball bond on top of it (see fig. 3.11).

A Polydimethylsiloxane (PDMS) mould was cast from a CNC milled Polyoxymethylene (POM) master mould. The two components of the PDMS Elastosil® M 4642 (*Wacker Chemie AG, Germany*) were mixed component A to B in a 10:1 by weight ratio and stirred by hand for 5 min. The mixture is degassed in a vacuum desiccator for 10 min, poured into the POM mould and degassed for another 10 min in the vacuum desiccator. Directly afterwards, the PDMS and the POM mould are transferred into an oven and hardened for 1 h at 100 °C. After deforming, the PDMS mould was used as casting frame for the subsequent PMMA cast, and attached to the set-up with an aluminium press for intimate contact. We used PMMA Paladur® (*Heraeus Kulzer, Germany*), a material commonly used in dental care for non-permanent prostheses. Since it is a medical product, it's easy to handle, and it has low volume shrinkage, which improves contour accuracy. The two components were mixed according to the Paladur® data sheet, where 0.6 ml fluid (Methylmethacrylate, Dimethylacrylate) and 1 g powder (Methylmethacrylate co-polymer) was mixed for 10 s by hand. Immediately after mixing, the Paladur® was filled into a syringe and dispensed into the PDMS mould. The set-up was cured in a pressure chamber at 2.5 bar for 12 h at 55 °C.

The PDMS mould was peeled off after PMMA curing. The overdue PMMA was removed by grinding with grain sizes P180 down to P1200, and polished with polishing suspension with particle sizes from 9 µm down to 3 µm with grinder and polisher machine model Beta (*Buehler Inc., USA*) (6). Since the wire bonded coil is stabilised by the PMMA cast, finally the PVA can be dissolved by placing the set-up for 24 h in water at 55 °C. This not only dissolves the PVA posts, but additionally removes the Pyrex chips from the FR4 carrier board (7). The resulting hollow micro coils are depicted in fig. 3.12.
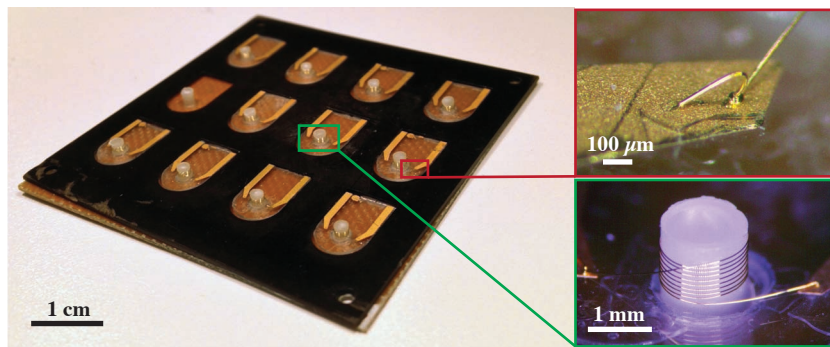
Fig. 3.11 Bottom: Array of wire bonded microcoils, wound around PVA posts. Upper right: Magnified view of one of the wire bonded microcoils. Upper left: Secured wedge bond. Image reprinted from [196].
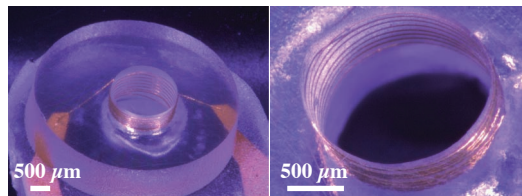
Fig. 3.12 Left: Wire bonded microcoil with external support to maximise the filling factor. Right: Close-up view of the microcoil windings (with an inter winding pitch of 100 µm). Image reprinted from [196].

Failure Mechanisms

During the evaluation of the PMMA casting process, some failure mechanisms were frequently observed, which will briefly be discussed in this subsection.

When using a two component system (e.g. by *S u. K Hock GmbH, Germany)*, that cross-links while curing, the volume shrinkage can be very large, as seen in fig. 3.13 b). Therefore, multiple casting steps are necessary to achieve the final structure. This does not only delay the manufacturing procedure, but additionally raises the probability to trap air bubbles into the cast, which then result in artifacts in the MR imaging or spectroscopy

measurement.

It is alternatively possible, to use a one component PMMA casting material. However, since the one component casting material is essentially drying out, rather than curing, the surface of the cast hardens first. This makes the casting method prone to trap air bubble, since the bubble, that presumably stem from evaporation of solvents, can not escape the cast, but is blocked by the hardened skin of the material.

If the PMMA is not cured perfectly, for example if cured under the wrong conditions, or if curing is not given enough time, the PMMA can absorb the PVA during the PVA etching step. As depicted in fig. 3.13 a, this leads to a tinted cast. This is not only an optical problem, but might alter material parameters, which then are not really defined.

All of these problems can be solved by the use of Paladur, a PMMA casting system with a liquid (Methylmethacrylate, Dimethylacrylate) and a powder based component (Methyl-methacrylate co-polymer) used in dental health-care (*Heraeus Kulzer, Germany*). This system has a very small volume shrinkage, and their casting procedure is bubble free. However, if the steps before the PMMA casting are not completely successful, such that the PVA posts have integrated air bubbles, the PMMA can flow into the hollow part of the coil (see fig. 3.13 c). If the PVA post is otherwise deformed, this then also leads to deformation of the PMMA cast, which can result in arbitrary structured in the inner part of the coil, as depicted in fig.3.13 d.
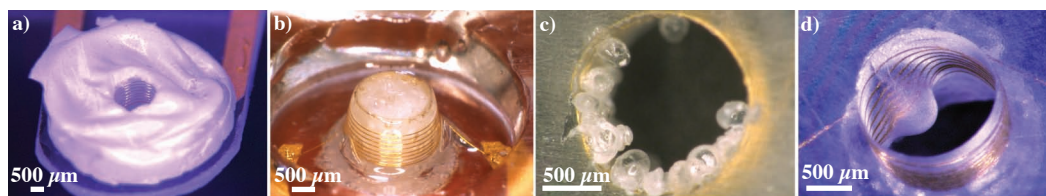
Fig. 3.13 a) Absorbed PVA during PMMA cast. b) Very high volume shrinkage of PMMA. c) Residue of air bubbles in the PVA cast. d) Nose-like PMMA structure that leaked into the PVA. Images adapted from [196].

Results of two-solvent manufactured hollow coils

During the course of this thesis, two different sets of micro coils were manufactured with the described two-solvent process. Both sets have an inner diameter of 1.5 mm and an interwinding pitch of 100 µm. In the first set, 8 coil windings were wire bonded, and in the second set only 5 windings. Both coil sets were first characterised for their electrical performance, and subsequently for their performance as MR probeheads.

The self-resonance frequencies of both coil sets were measured with a 1 cm diameter pickup coil, connected to a USB vector network analyser (*miniVNA Tiny, miniradiosolu-*

tions.com). From the S11 reflection curve, the self-resonance frequencies were measured to be $f_{SRF8} = 1003.2 \pm 29.6\,\text{MHz}$ and $f_{SRF5} = 1118.4 \pm 37.1\,\text{MHz}$. The self-resonance frequency (SRF) of a coil is where the coil inductance and the parasitic capacitances form a resonant circuit. This is the frequency, from which the coil is dominated by the capacitance, and above the self-resonance frequency the energy is stored predominantly in the electric field, such that the coil is useless as MR probehead. The coil resonators q-factors were calculated from these reflection curves to be $Q_8 = 113.8 \pm 13.6$ and $Q_5 = 64.0 \pm 2.0$. As the coils are used attached to an MR probehead, it is useful to characterise their electrical performance when set-up into their coupling network. The first coil set, with 8 windings was not tunable to 400 MHz with the depicted circuit, the proton Larmor frequency of the available MR scanner. Because of that, only the set with 5 windings was characterised with its coupling network. After tuning to 400 MHz and matching to $50\,\Omega$, the Q-factor was averaged from the S11 curve of the cable bound coil. An exemplary S11 curve is depicted in fig. 3.14, and the Q factor for 5 different coils was $Q_{TM} = 44.0 \pm 5.2$. Magnetic resonance
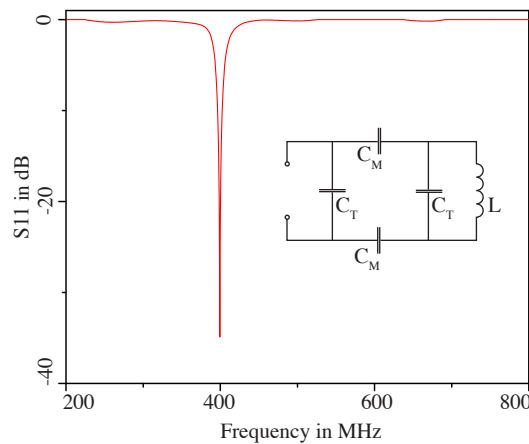
Fig. 3.14 S11 curve of a hollow micro-coil, tuned and matched to 400 MHz and 50 Ohm and a schematic of the tuning and matching network.

experiments were performed with a conventional horizontal bore Bruker BioSpec 94/20 USR (*Bruker BioSpin, Ettlingen, Germany*) at a static magnetic field strength of 9.4 T, which correspongs to a 1H larmor frequency of 400 MHz. The full-width half-maximum (FWHM) linewidth was determined from a pure sample of deionized water. As shown in fig. 3.15, the linewidth was 0.081 ppm, corresponding to 32.43 Hz at 400 MHz. A nutation spectrum was acquired, by sweeping the excitation pulse length from 0 to 170 µs in 10 µs steps at a constant excitation pulse power of 0.625 mW. From the nutation spectrum, the 90° flip angle was determined to be at 140 µs at 0.625 mW. The nutation frequency can be computed from the period of the nutation spectrum envelope function. The period

was measured to be $T_{\text{nut}} = 560\,\mu\text{s}$ yielding a nutation frequency of $f_{\text{nut}} = 1785.7\,\text{Hz}$. With the gyromagnetic ratio of protons $\gamma_{1\text{H}} = 42.576\,\text{MHz}\,\text{T}^{-1}$ and equation 2.15, the r.f. field strength is calculated to be $B_1 = 83.88\,\mu\text{T}$. The probehead efficiency is derived by normalising the r.f. field strength by the square root of the excitation pulse power, such that $\eta_{\text{rf}} = B_1 / \sqrt{P_{\text{exc}}} = 3355\,\mu\text{T} / \sqrt{W}$, where $P_{\text{exc}} = 0.625\,\text{mW}$.

For further characterisation, MR images were taken with different configurations. Coronal and axial images were recorded with a standard FLASH sequence. The first set of images was acquired in receive only mode. Spin excitation was delivered by a 74 mm diameter volume coil and the micro coil was positioned in the isocentre of both, the volume coil and the static magnetic field. The excitation by a larger volume coil should yield a more homogeneous excitation field, while signal reception still remains efficient through the micro coil. A repetition time of $T_R = 100\,\text{ms}$ and an echo time of $T_E = 6\,\text{ms}$ was set. The flip angle was set to 30° at a slice thickness of 170 µm. The field of view FOV = 0.33 x 0.33 cm^2 at a matrix size of MTX = 100 x 100 yields a resolution of 33 x 33 µm^2. Averaging this sequence over 64 acquisitions (NEX = 64) results in an imaging Signal-to-noise ratio of $SNR_i = 41$ for the MR images are shown in fig. 3.16. From the receive only imaging sequence, high signal intensity can clearly be identified in close proximity of the micro coil, which is in general not observable in set-ups where the windings are further away from the signal giving sample.

The second set of MR images was recorded in transceive mode, such that the micro coil is used for both, spin excitation and signal reception. This way, the spin excitation is less homogeneous, but is more efficient, since the magnetic energy is only deposited where the sample is. At $T_R = 267\,\text{ms}$, $T_E = 4.8\,\text{ms}$ and FA = 30°, images with a slice thickness of 250 µm, a field of view of FOV = 0.30 x 0.30 cm and a matrix size of MTX = 120 x 120 yielded a resolution of 25 x 25 µm. Averaging 64 times resulted in an image SNR of $SNR_i = 218$.
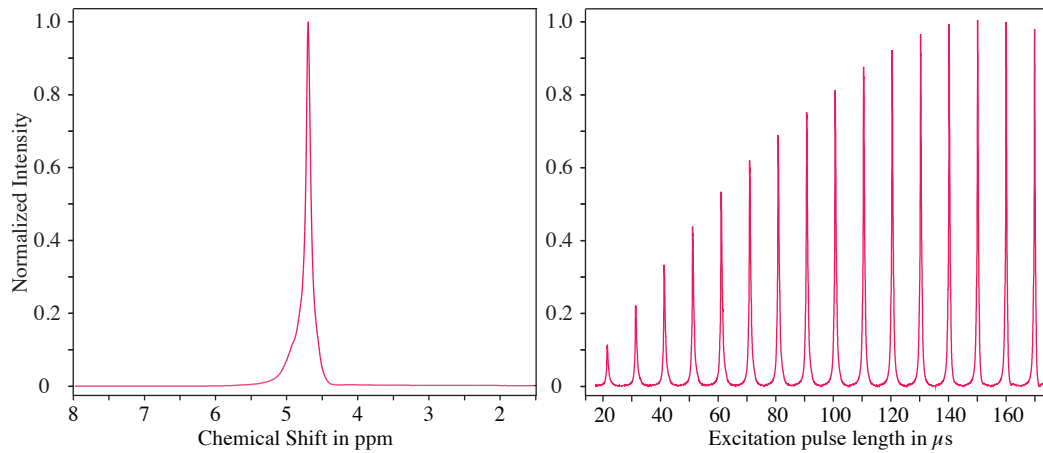
Fig. 3.15 NMR spectrum (left) and nutation spectrum (right) of water, recorded in a 400 MHz Bruker Biospin system with the manufactured micro-coil.
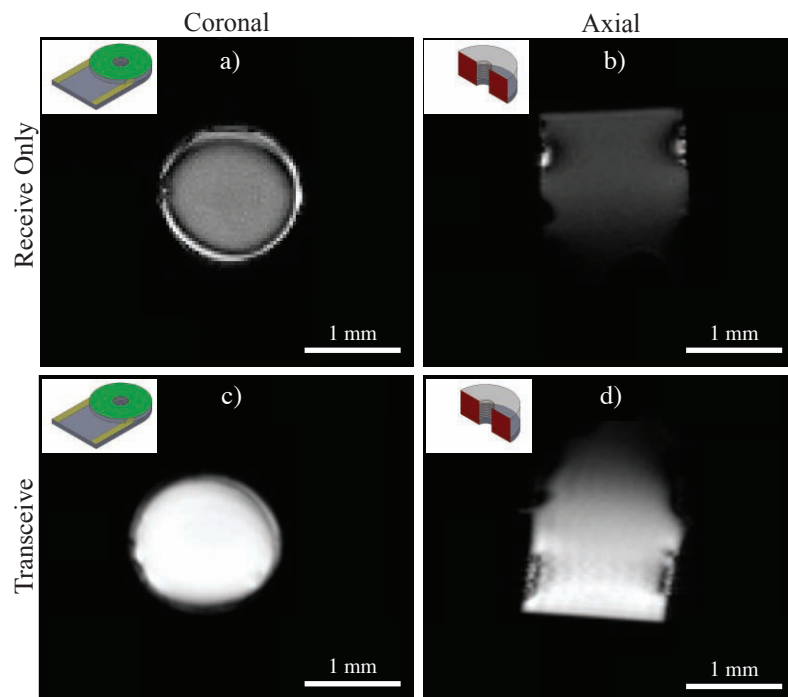

Fig. 3.16 Coronal and axial MRI sections through a hollow micro-coil in receive only (a and b) and in transceive mode (c and d). Image reprinted from [196].

3.4.3   Version 3 - Manufacturing using PTFE sleeves

The manufacturing using two-solvents and a bulk cast of PVA allows for uniform micro coils. However, the volume shrinkage of the PVA cast leads to a low contour accuracy. Even more crucial is that PVA becomes soft at high temperature. Therefore, gold wire bonding at 125 °C worked, but at 150 °C which is the temperature needed for copper wire bonding. By using PTFE sleeves, temperature and high contour accuracy is achieved.

Standard 1 mm thick FR-4 printed circuit boards (PCB) with 35 μm copper layers (*Bungard Elektronik GmbH, Germany*) were milled using an ISEL 4030 mini mill for mechanical structuring using the milling parameters given in appendix E.2. For high precision the photoresist was directly ablated with an Nd:YVO4 marking UV-laser TruMark 6330 (*Trumpf GmbH, Germany*) at 355 nm wave length, fitted with a custom alignment system. Ablation was done at 100 % power, a lasering speed of 600 mm s^{-1}, 20 kHz pulse frequency and a hatching pattern. The PCB was subsequently etched in a bench top bubble etch tank PA104 (*Mega Electronics Ltd., UK*) for 15 min at 45 °C in a sodium persulfate - water solution (220 gl^{-1}). To ensure optimal wirebond adhesion, 5 μm gold was electroplated onto the copper pads.
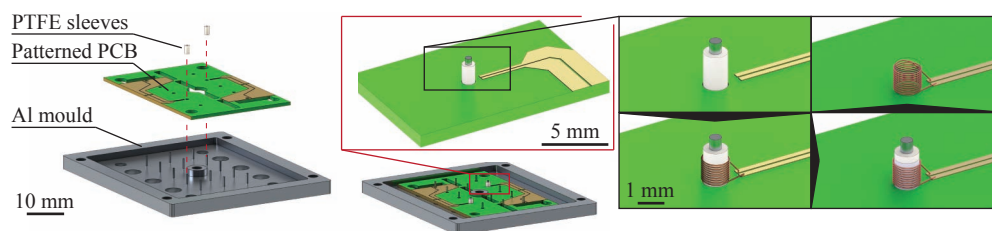
Fig. 3.17 A PCB is mounted onto an aluminium form with pins for PTFE sleeves. The micro coils are wire bonded around the PTFE sleeves. After casting the coils into Araldite 2020 the PTFE sleeves are removed.

An aluminium mould fitted to the wirebonder, with 0.5 mm diameter, 3 mm high yokes was milled with a 4030 CNC mill (*isel Germany AG, Germany*) using the paramters given in appendix E.3. This aluminium mould serves as multi-use wirebonding mould, in which different PCB designs might be fitted. As shown in fig. 3.17, the PCB is placed into the aluminium mould, and 2.5 mm pieces of 0.5 mm/1 mm inner/outter diameter Polytetrafluoroethylene (PTFE) tubing (*Laborhandel24 GmbH, Germany*), were slid over the aluminium yokes.

The whole set-up was subsequently mounted to the wire bonder 3100plus (*ESEC, Switzerland*), and microcoils with a diameter of 1 mm and 0 mm height, and an interwinding pitch of 25 μm were wound from an 50 μm diameter insulated copper wire. Wire bonding

was done at 150 °C. The ball bond was formed with an impact force of 700 mN, a bond
force of 350 mN at 80 % ultrasound power and a bond time of 40 ms. The wedge bond
was done with an impact force of 800 mN, a bond force of 500 mN at 38 % ultrasound
power and a bond time of 25 ms respectively. A 5 mm thick mould milled from PTFE was
then pressed onto the PCB with an external aluminium board screwed to the bottom
aluminium mould. Two component clear epoxy adhesive Araldite 2020 (*Huntsman Inter-
national LLC, USA*) was mixed in a component A to B 10:3 ratio by weight and stirred by
hand for 5 min. The mixture was degassed for 10 min in a vacuum desiccator, cast into
the PTFE mould and degassed another time for 5 min. Araldite 2020 cured under 2.5 bar
nitrogen pressure at 100 °C for 1 h. Subsequently the PTFE mould was released and the
Aluminium mould with the yokes was pushed out of the PTFE tubing. The PTFE tubings
were pushed through the Araldite with a blunted needle. As a last step, the protruded
Araldite 2020 was ground with a grinder and polisher machine model Beta (*Buehler Inc.,
USA*) from grain size P180 to P1200 and polished down to 3 µm, to have a flat surface.

3.4.4   Intermediate conclusion hollow micro coils

Several structures were used for winding micro coils. For the two solvent process, a PVA
cast is used as dissolvable pole to wind a micro coil. PVA has its melting point at 200 °C
and its glass transition temperature at 85 °C, limiting the maximum temperature of the
wirebonding step. Therefore, the two solvent process is most likely only feasible for gold
wirebonding, but not suited for copper bonding. At gold wirebonding temperatures of
125 °C the PVA poles became soft but manufacturing with 25 µm gold wire was manage-
able. Since copper wirebonding needs higher substrate temperatures, a manufacturing
procedure which implements PTFE sleeves mounted onto milled aluminium rods was
developed. With this process, hollow micro coils with diameters down to 1 mm diameter
were manufactured from 50 µm insulated copper wire.

The hollow micro coils were embedded into PMMA or Araldite 2020. The Q factor of the
coils can be diminished by the embedding, since the the air between windings is replaced
by a lossy material (higher dielectric loss tangent), which increases parastic capacitance
and losses. When approaching self-resonance, the parasitics influence increases since
an increasing fraction of the energy is stored in the electric rather than in the magnetic
field [206]. For an increasing frequency, at its self-resonance frequency, the resonator
changes from inductive to capacitive behaviour. The micro coils were designed for a work-
ing frequency of 400 MHz and its MR detector performance should not suffer from the
capacitive behaviour since the self-resonance frequency is approximately 1 GHz. However,
when further application at higher frequencies become of interest, these losses can not be

neglected. Then, the casting material needs to matched to the application (i.e. low loss material, MR compatible, zero-susceptbility).

The micro coils manufactured, are competitive with other devices, but the linewidths of 0.081 ppm needs improvements if high resolution spectra are aimed for[22]. An r.f. efficiency of $3355\,\mu\mathrm{T}/\sqrt{\mathrm{W}}$ is comparable to similar devices, i.e. by Ryan *et al.* [19], with an efficiency of $184\,\mu\mathrm{T}/\sqrt{\mathrm{W}}$, Sakellariou *et al.* with an efficiency of $2030\,\mu\mathrm{T}/\sqrt{\mathrm{W}}$ [159] and Sillerud *et al.* with an efficiency of $1897\,\mu\mathrm{T}/\sqrt{\mathrm{W}}$ [207].

Using the micro coils, high resolution MR images were acquired with a non-RF-spoiled FLASH sequence at 9.4 T field strength, as shown in fig. 3.16. The high intensity peaks demonstrate the wire influence, which is in direct proximity of the sample. For very small samples, this needs to be compensated for, as for example by passive shimming [208].

This newly developed processes allow for the manufacturing of micro coils with a filling factor of 100 %. To this time point, this has not yet been possible, and it presents a significant step towards miniaturisation micro coils, especially for magnetic resonance applications. Other publications dealt with hollow micro coils with smaller filling factors. Micro coils by wire winding around PMMA posts structured by deep X-ray lithography and by SU-8 posts were published by Kratt *et al.*[185, 186]. Manufacturing of these micro coils required a wall thickness of the hollow posts of minimum 20 μm for PMMA and 60 μm for SU-8. This permits a filling factor of of 94.5 % and 84.6 % respectively for 1.5 mm diameter coils. The coils by Sillerud *et al.* were manufactured on a glass capillary with an outer diameter of 550 μm resulting in a filling factor of 53 % [207]. For miniaturisation, the minimal yoke wall area needs to be kept constant to withstand wire bonding force and hence the filling factor suffers tremendously. However, with miniaturisation the SNR increases linearly, while the spectral resolution suffers [106]. Thus high filling factor micro coils are particularly useful where line-width is less important than concentration sensitivity or small volumes.

3.5   Lenz Lenses

A significant part of this section on Lenz lenses and inductive coupling will be submitted to the Journal of Magnetic Resonance as [RK3][a]

---

[a]Contributions: *MJ:* Theory and calculation, data interpretation, manuscript concept and writing. *RK:* Coil design, MR data acquisition, processing and analysis, manuscript concept and writing. *JL:* MR data acquisition and optimisation, manuscript proofread. *NS:* Initial coil concept, manuscript proofread. *JH:* MR sequences and methods, manuscript proofread. *JGK:* data interpretation, manuscript proofread. *OGG:* Coil design, MR data acquisition, manuscript concept and writing.

3.5.1   Introduction to Lenz Lenses

Since the beginnings of magnetic resonance, inductive coupling has been used for two main applications. Either for tuning and matching of an MR probe [109, 209, 210] or for contactless signal transmission [211–214] where access is restricted. Inductive coupling is achieved, by bringing the primary coil in close proximity to the secondary coupled coil. The primary coil and the secondary coil are coupled, when the primary coils flux field lines penetrate an area enclosed by the secondary coil. They are described by their mutual inductance. The inductive coupling is described by Faraday's law.

$$emf = \frac{d\Phi_B}{dt} \tag{3.1}$$

Signal between the coils depends on the strength of the magnetic flux (Φ_B) and the percentage of field lines the secondary coil is able to collect.

With inductive coupling, LC resonators (an inductance + tuning capacitor) have been used for a long time for their coupling is very efficient. However, with sufficient coupling, using an inductively coupled LC resonator leads to a resonance splitting in the tuning and matching curve, which means one needs a broader range for tuning. LC resonators are restricted to one acquisition frequency, rendering multi-nuclear experiments difficult.

On the other hand, broadband MR probes can still be efficient. The Lenz lens, as introduced by Schoenmaker *et al.* [215], consists of a single current carrying track, with an outer and an inner loop (see fig. 3.18). When coupled inductively to a magnetic field (from the primary coil), as the Lenz law states, the induced current flows in the direction that opposes the source current. Since in a Lenz lens, there is a single current carrying track, the outer loop of the lenz lens carries the opposing current, while the current direction of the inner loop has the same direction as the source current. Since the magnetic flux density (B-field) in a current loop depends on the current and the radius of the loop, the magnetic flux density is higher in the inner loop, and thus the magnetic flux is focused.

Following optical terminology, focusing capability in combination with following the Lenz law, this device was termed Lenz lens.

Although Schoenmaker *et al.* described the flux focussing capabilities of Lenz lenses, they did not utilise it for any magnetic resonance experiments. The application of the Lenz lenses in MR was introduced by Spengler *et al.* [216, 217]. While Schoenmaker *et al.* derived equations and simulations to compute the current in a lenz lens up to approx. 100 kHz, Spengler *et al.* extended the model for the high frequency regime of MR. Spengler *et al.* additionally introduced Lenz lenses in a Helmholtz-like configuration, which may enlarge the focusing zone, and improve the B-field homogeneity in the focusing area. Both papers additionally manufactured sets of Lenz lenses, and performed technical characterisation. However, neither of the above mentioned publications compare Lenz lenses to conventional inductively coupled LC resonators or deal with the application of Lenz lenses to resolve tissue microstructure.
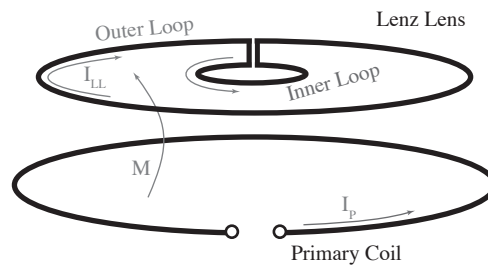
Fig. 3.18 Schematic representation of the primary coil and the Lenz lens w.r.t. each other.

3.5.2 Theory

This section on the theory and the computations of Lenz lenses a based on the work done by Mazin Jouda of the Institute of Microstructure Technology, Karlsruhe Institute of Technology.

In this section, a wired - tuned and matched - detector coil (wired LC), an inductively coupled LC detector coil (LC resonator) and a Lenz lens (LL) and their SNRs are compared. Therefore, all three coils are modelled with a simple circuit. Starting with the wired LC, the circuit is depicted in fig. 3.19 a. The value for the tuning capacitor C_T can be computed from the real part of equation 3.2 at the larmor frequency ω_L.

$$\{1/(j\omega_L \cdot C_T) || r_a + j\omega_L \cdot L_a\} = 50 + jX \tag{3.2}$$

For matching the coil L_a, the imaginary part of the equation can be eliminated through C_M computed from the imaginary part of:

$$\{1/(j\omega_L \cdot C_T)||r_a + j\omega_L \cdot L_a\} + 1/(j\omega_L \cdot C_M) = 50 \tag{3.3}$$

In the circuit, the MR signal is represented by the signal voltage v_{sig}, acquired through the detection coil L_a. In accordance with the principle of reciprocity [103] it can be calculated from:

$$v_{sig} = K\omega_L B_1 V_s M_0 \tag{3.4}$$

which depends on an inhomogeneiety factor K, the transverse magnetic field B_1 when a 1 A current is fed through the coil, the sample volume V_s and the magnetisation M_0. The magnetisation can be computed from:

$$M_0 = \frac{N^2 \gamma^2 \hbar^2 I(I+1) B_0}{3 k_B T_s} \tag{3.5}$$

where N is the number of spins in the sample, γ the gyromagnetic ratio, $\hbar$ the Planck's constant (reduced), I the spin quantum number, k_b the Boltzmann constant and T_s the sample temperature in Kelvin.

The noise is represented by the noise voltage v_n and depends on the coil temperature T_c, the receiver bandwidth Δf and the coil AC resistance R_{noise} (which includes the skin and proximity effect).

$$v_n = \sqrt{4 k_B T_c \Delta f R_{noise}} \tag{3.6}$$

If the receiver bandwidth and the sample volume is fixed, the SNR depends strongly on the coil geometry. Assuming a spherical sample with a fixed diameter of d_{sample} and a surface coil with a diameter d_{coil} the SNR drops dramatically when the coil diameter increases (decreasing filling factor). This is depicted in fig. 3.19, where the SNR is normalised by the SNR one can obtain when $d_{coil} = d_{sample}$. The SNR is computed from fig. 3.19 a (w/o receiver noise). The curve is dominated by the AC resistance of the coil (higher v_n) and the decrease in B_1 field strength in the sample volume (lower v_{sig}).
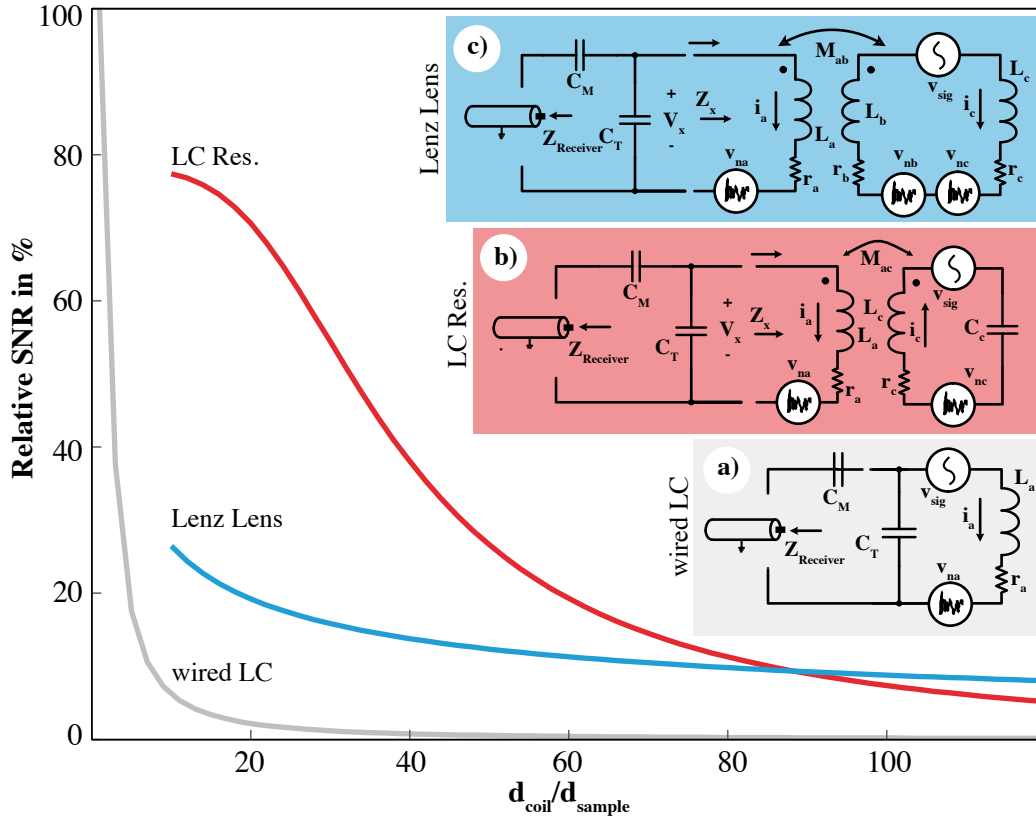
Fig. 3.19 The decrease of the relative SNR of a wired detector coil (a), an inductively coupled LC resonator (b) and a Lenz lens (c) and computed from their circuit schematics for increasing coil diameters and a fixed sample diameter.

As demonstrated a high filling factor of the coil is desired for an optimal SNR. However, a high filling factor can not always be achieved with the detection coils mounted into a specific MR spectrometer or MR scanner, as for example when a specific part of a sample needs to be imaged or in magic angle spinning. Inductively coupled coils have long been used to approach this challenge. An LC resonators, which is an inductor L with a high filling factor with an attached tuning capacitor that resonates at $\omega_L = 1/LC$, can be one solution. A circuit model of an LC resonator coupled to a transmission coil is depicted in fig. 3.19 b. When using an LC resonator, C_M and C_T need to be adapted and can be found through:

$$Z_x = \frac{V_x}{I_x} = r_a + j\omega_L L_a - \frac{(j\omega_L M_{ac})^2}{r_c + j\omega_L L_c + \frac{1}{j\omega_L C}} \tag{3.7}$$

$$\Re\left[\frac{Z_x \cdot \frac{1}{j\omega_L C_T}}{Z_x + \frac{1}{j\omega_L C_T}}\right] = 50 \tag{3.8}$$

$$\Im \left[\frac{1}{j\omega_L C_M} + \frac{Z_x \cdot \frac{1}{j\omega_L C_T}}{Z_x + \frac{1}{j\omega_L C_T}} \right] = 0 \tag{3.9}$$

Then, the SNR can be computed by superposition, where the noise power of the coils add and thus $V_n = (V'^2_{na} + V'^2_{nc})^{1/2}$. As depicted in fig. 3.19, the LC resonator efficiently enhances the SNR (if the LC resonator is tuned to the larmor frequency), when the detector coil diameter increases (while the LC resonator diameter stays constant with an optimum filling factor). Here, the SNR of the LC resonator mainly degrades due to lower coupling between primary detector coil and LC resonator.

Now a Lenz lens, with an inner loop L_c (with high filling factor) and an outer loop L_b (to collect the maximum amount of B_1 field from the primary coil L_a) is considered. L_b collects the current from L_a and, since both are connected, this current runs through L_c and results in a high B_1 field in the sample volume. As the principle of reciprocity states, a high B_1 results in a high NMR signal, which is then coupled to L_a.
This circuit is modelled as depicted in fig. 3.19 c. Since the primary coil and the outer loop of the Lenz lens are by far bigger than the inner loop diameter, the coupling between $L_a - L_c$ and $L_b - L_c$ is neglected. The impedance of the coil then changes to:

$$Z_x = \frac{V_x}{I_x} = r_a + j\omega L_a - \frac{(j\omega M_{ab})^2}{r_b + r_c + j\omega L_b + j\omega L_c} \tag{3.10}$$

With the obtained Z_x, C_T and C_M can be computed from equations 3.8 and 3.9. Solving the circuit by superposition and obtaining the noise voltage with $V_n = (V'^2_{na} + V'^2_{nb} + V'^2_{nc})^{1/2}$ the resulting relative SNR is depicted in fig. 3.19.

3.5.3   Experimental comparison of LC resonators and Lenz lenses

A series of experiments was recorded to compare a wired MR probe with an inductively coupled LC resonator and three different Lenz lenses. A custom Tx/Rx surface coil with a diameter of 50 mm is used. The wired MR probe, the LC resonator and all Lenz lenses have the same inner coil diameter of 5 mm. The Lenz lenses outer diameter is varied between 45 mm (big), 22.5 mm (middle) and 12.5 mm (small), giving area ratios of 81, 20.25 and 6.25. All test lenses, coils and resonators are depicted in fig. 3.20. Water was used as reference sample. The round PMMA sample container has a fixed sample volume of 40 μl with a diameter of 4.5 mm and a height of 2.5 mm. For every measurement, the sample is positioned in the centre of the MR probe. For all measurements, a 9.4 T horizontal

Table 3.4 Measurement results for different inductively coupled coils with a fixed inner coil diameter (ID) of 5 mm and various outer diameters (OD). The integrals are acquired over from 8 ppm to 2 ppm. Images and the spectra of the coils are given in fig. 3.20.

| | | | Lenz Lenses | | | |
	a) w.LC	b) LC Res.	c) Big	d) Middle	e) Small	f) Tx/Rx
OD/ID in mm/mm	5/5	5/5	45/5	22.5/5	12.5/5	50/50
Abs. SNR	10959	8565	2743	1514	1167	1401
Rel. SNR in %	100.0	78.2	25.9	13.8	10.6	12.8
Calc. SNR in %	100.0	77.3	26.5	16.5	8.2	7.2
Linewidth in Hz	28.69	29.65	36.21	21.95	19.47	16.83
Efficiency in	167.77	148.80	58.72	24.72	18.79	16.20
Abs. Integrals	0.89	0.86	0.32	0.17	0.13	0.12
Normalised Integrals	1.00	0.98	0.36	0.19	0.15	0.14

bore Bruker small animal scanner was used. Before data acquisition, an automated shim procedure was applied (B0 map acquisition, map shim and iterative shim). The 90° flip angle was found with a nutation experiment, by sweeping the excitation pulse length at 1 W excitation pulse power. The probe efficiencies were computed from the nutation sepctra by using equation 2.15 and the gyromagnetic ratio of protons of $\gamma_{1H} = 42.576\,\mathrm{MHz}\,\mathrm{T}^{-1}$. Water spectra were acquired without averaging for all set-ups with approximately the same linewidth at half maximum of 20-30 Hz, as depicted in fig. 3.20. The SNR of each spectrum is computed from the noise over a 2 ppm region and the peak height of the water signal using the TopSpin software (*Bruker BioSpin, Germany*). Similarly, the integral of each spectrum was measured from 8 ppm to 2 ppm for each spectrum and normalised by for the maximum integral to be 1.0. All measurement data is summarised in table 3.4.

The wired MR probe with a high filling factor and minimum transmission losses is the most efficient with an SNR of 10959 used as reference SNR to normalise the SNR (100 %), and the integral of 0.885 was normalised to be 1.0. The 50 mm diameter Tx/Rx coil is measured at a relative SNR of 12.8 % and a normalised integral of 0.14. Unsurprisingly, the LC resonator at 78.2 % of the SNR and an integral of 0.98 is close to the wired MR probe performance and to the calculated relative SNR of 77.3 %. For the broadband Lenz lenses, the biggest one with an outer diameter of 45 mm performes at an SNR of 25 % and an integral of 0.36, which is an SNR gain of apporximately a factor of 2 over the Tx/Rx coil. The smalles Lenz lens with an relative SNR of 10.6 % however performs even worse than the Tx/Rx coil, if only the SNR is considered. The relative SNR for the measured circuit
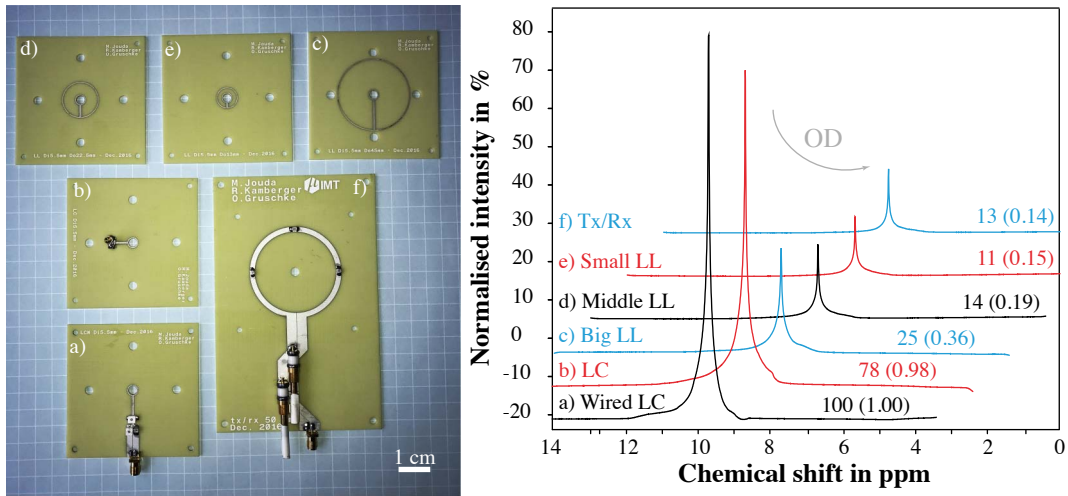
Fig. 3.20 Left: Images of the (a) the wired LC resonator, (b) the LC resonator, (c) the big, (d) the middle, (e) the small lenz lenses with inner coil diameter of 5 mm and (f) the reference Tx/Rx coil. Right: Collected spectra from a 4.5 mm diameter 40 µl water sample with their normalised intensities in %. The values for the normalised integrals (integrated from 8 ppm to 2 ppm) are given in brackets.

was additionally computed according to the procedure described in section 3.5.2. As can be seen from table 3.4, the computed values (Calc. SNR in %), are in good correlation with the experimental values. However, the smallest Lenz lens performs worse in SNR in the experiment than the Tx/Rx coil, which is presumably owed to the smaller linewidth in the Tx/Rx experiment. It should be noted, that for the big Lenz lens, it was necessary to re-tune and re-match the Tx/Rx coil, since its tuning range was exceeded. Although these measurements give indication how the different resonators and lenses perform, it should be noted, that the SNR of the spectra depends on the linewidths. They could not be exactly matched for all resonators, since the proximity of copper conductors and discrete capacitors induce B_0 inhomogenieties. The integrals are less affected by the linewidth, thus the integral of the small lenz lens with 0.15 is marginally better performing than the Tx/Rx coil with an integral of 0.14. An alternative measure for comparison, the probe head efficiency can be used, which is also given in table 3.4.

3.5.4   Designs for the MR microscopy

The Lenz lenses used for MR microscopy in this thesis, are designed to fit the incubation system introduced in detail in chapter 4. Therefore, the Lenz lenses have an inner diameter of 5 mm, while the outer shape is defined by the boundary conditions imposed by the incubator. Thus, the Lenz lens outer circumference is not a concentric circle, but a copper

track along the inlet holder, to maximise the area ratio (and thus the magnification factor), between inner and outer loop of the Lenz lens. There are three principal versions of the Lenz lenses manufactured (see fig. 3.21). (a) Two symmetrical copper tracks, that each form one half of the inner and one half of the outer loops. (b) A Lenz lens with with a single copper track for the inner and outer loop of the lens. (c) Two symmetrical copper sheets, filling the whole area between inner and outer loop, that focus the magnetic flux via eddy currents. The magnification in B_1 field strength was simulated using Maxwell 2015.2 (*ANSYS Inc., USA*), where for a constant current i, the SNR scales linearly with B_1. For the simulation a uniform B_1 field was generated by a 50 mm diameter Helmholtz coil configuration, with an applied current of 1 A, resulting in a mean B_1 field of 76 μT in the centre. For the simulation it is assumed that the Lenz lenses are concentrically aligned within the Helmholtz coil, without any tilt. A copper conductor with a bulk conductivity of 58 MS m^{-1} is assumed and an excitation frequency of 400 MHz is used, which results in a skin depth of 3.3 μm in copper. The carrier substrate (polyimide) is neglected. The B_1 field profiles from a diagonal cut through the lenses are shown in fig. 3.21. The simulated B_1 fields of the Lenz lenses are normalised by the field generated from the Helmholtz coil only, to evaluate the gain in B_1 field strength resulting from the Lenz lenses. The simulation shows that the Lenz lenses with an area ratio of 6.25 and of 10 shown an increase in B_1 of a factor of approximately 1.3 and 1.5 respectively, corresponding to a mean B_1 field of approx. 100 μT and 120 μT. As the B_1 field strength scales linearly with the SNR, this should also hold for the SNR gain.

The maximum magnification of the Lenz lenses can additionally pushed, by attaching an external capacitance, to form an LC resonant circuit. It combines the advantages of an LC resonator with the flux focusing capabilities of the Lenz lens. However, it is then obvious, that one looses the broadband reception feature of non-resonant circuits.
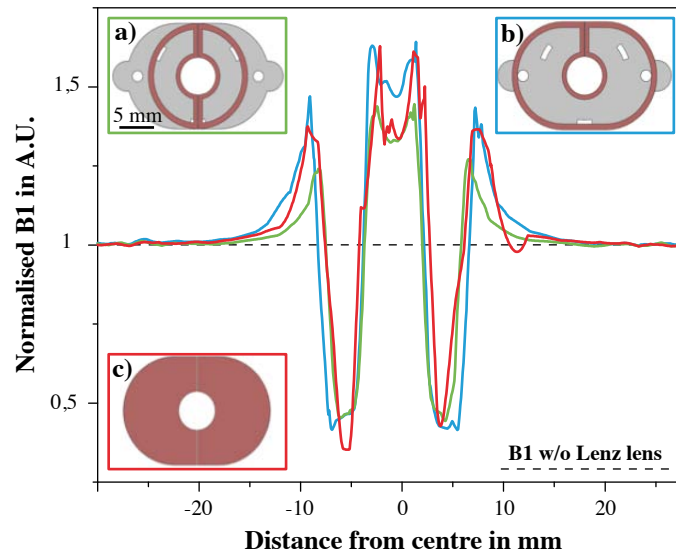
Fig. 3.21 B_1 field profile simulation three Lenz lenses normalised by a B_1 field of a 50 mm diameter Helmholtz excitation coil.

3.5.5   Manufacturing Procedure for flexible Lenz lenses

The Lenz lens layout was design with the computer aided design (CAD) software Solidworks 2014 (*Dessault Systems SE, France*). The basis for the flexible Lenz lenses manufactured during the course of this thesis, are flexible printed circuit boards RF775 RA 50 (*Contag AG, Germany*). The base material of these boards is a 50 μm Polyimide (PI) sheet with a 55 μm thick copper layer. The Lenz lenses are manufactured in a custom process summarised in table 3.5.
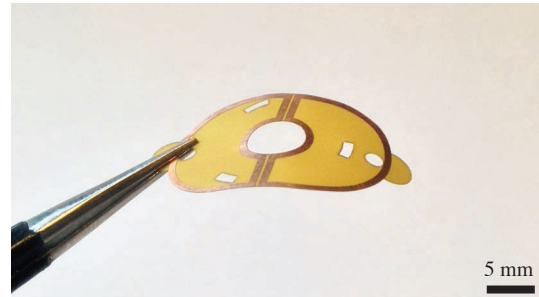
Fig. 3.22 Photo of a flexible Lenz lens manufactured with the described process.

The substrates are cut into 100 mm round sheets by hand. A 100 mm diameter silicon wafer is used as handle wafer. 2 ml PAA ($M_w \approx 100000$, 35 wt − % in water, *Sigma Aldrich Chemie GmbH & Co.KG, Germany*), neutralised with saturated NaOH solution (*Sigma Aldrich Chemie GmbH, Germany*) is spin coated onto the handle wafer at 2000 rpm for 30 s. The substrate is laminated by hand onto the handling wafer subsequently (1). The sandwich is dried on a hotplate for 30 min at 100 °C. Then, AZ 9260 positive photoresist (*Microchemicals GmbH, Germany*) is spincoated for 30 s at 2000 rpm onto the substrate and softbaked for 15 min at 110 °C on a hotplate (2). The photoresist is structured di-

rectly by UV-laser ablation with a Trumark 6330 (*Trumpf GmbH, Germany*) marking laser at 355 nm wave length (3), fitted with a custom alignment system. Ablation was done at 100 % power, a lasering speed of 600 mm s^{-1}, 20 kHz pulse frequency and a hatching pattern. The copper is selectively etched (4) in a bench top bubble tank PA104 (*Mega Electronics Ltd., UK*) for 15 min at 45 °C in a sodium persulfate - water solution (220 g l^{-1}). The substrate is removed from the carrier wafer by a 15 min PAA etch in water at room temperature (5). Structuring of the PI substrate is then performed using direct laser writing with a TruMark 6330 UV-laser, with 100 % power, a lasering speed of 170 mm s^{-1}, 25 kHz pulse frequency and 18 repetitions (6).

Table 3.5 Manufacturing of flexible Lenz lenses.

Step		Process	Parameters
1		Laminate Cu-PI foil on carrier substrate	Neutralised PAA as glue, dry 30 min at 100 °C
2		Spincoat AZ 9260 masking layer	30 s at 2000 rpm Hotplate 15 min at 110 °C
3		UV-Laser Direct Writing of AZ 9260	100 % power, 600 mm s^{-1}, 20 kHz
4		Copper Etch	Sodium persulfate (220 g l^{-1}) in water for 15 min at 45 °C
5		Remove Foil from carrier substrate	15 min in DI-water at room temperature
6		UV-laser cut alignment structures (optional)	100 % power, 170 mm s^{-1}, 25 kHz, 18 repetitions

3.5.6 Results of Lenz lenses in the MR incubator

The Lenz lenses as designed for later use in the incubation system described in chapter 4, were tested first in a tube filled with water as a reference, and then in the incubation system. All measurements for characterisation were done at a 9.4 T horizontal bore Bruker Biospin small animal scanner equipped with a 72 mm volume rat coil. Three different

Lenz lens designs were glued onto a PMMA holder, adjusted in a plastic tube flooded
with water and sealed air tight. A CPMG-RARE sequence was run with parameters TR =
5000 ms, TE = 66.4 ms, slice thickness = 0.25 mm, FOV = 8.0 x 4.14 cm^2, MTX = 500 x 259
and NEX = 4.
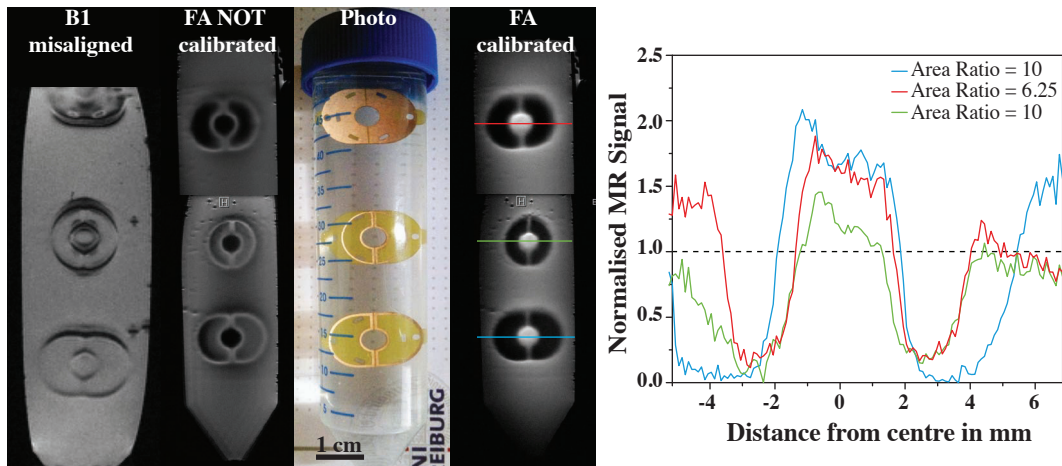
Fig. 3.23 Three different Lenz lens designs placed into a water filled plastic tube. When B1
is misaligned by 90°, no signal change in the lenz lens centre can be observed (only B0
field distortion). A poor calibration of the flip angle results in signal loss (in the Lenz lens
centre). With proper adjustments, the signal is enhanced in the centre of the Lenz lens.
The magnification depends on the area ratio of the lenz lens, as depicted in the normalised
SNR profiles (w.r.t. to a 72 mm volume coil). The CPMG-RARE sequence was run with
parameters TR = 5000 ms, TE = 66.4 ms, slice thickness = 0.25 mm, FOV = 8.0 x 4.14 cm^2,
MTX = 500 x 259 and NEX = 4.

As depicted in fig. 3.23, when the axes of the Lenz lenses is misaligned to the B1 field by
90°, the lenses only produce artefacts due to the B0 inhomogeniety imposed by the copper
tracks, but no signal amplification can be observed. The outcome dramatically changes,
when the lenz lens axis is aligned with the B1 field of the primary coil. The automatic
calibration procedure of the ParaVision software (*Bruker BioSpin GmbH, Germany*) cali-
brated the reference power for the 90° flip angle by maximising the signal over the sample
volume in an sagittal slice. Therefore, when the automatic reference power calibration is
used, the signal is optimised not for the region of interest in the center of the Lenz lens.
This miscalibration can result in a flip angle of more than 90° in the centre of the Lenz
lens, thus resulting in signal loss in this particular area of interest. Obviously, for optimal
use of the Lenz lenses this needs to be avoided. When the reference power adjustment
procedure is adapted to be optimised in the lenz lens centre (in this measurement, using a
coronal slice through the Lenz lenses was sufficient), the MR signal is clearly amplified in

the centre of the Lenz lens. In fig. 3.23 SNR profiles through the Lenz lenses with calibrated flip angles are depicted. They show an SNR gain of approx. a factor of 1.5 for the Lenz lenses with an area ratio of 10, and an SNR gain of approximately 1.25 for the Lenz lens with the area ration of 6.25. As expected, it also makes no significant difference, whether the Lenz lens flux collecting area is made from a sheet of copper, or only a thinner wire used to collect the flux. The by far strongest influence on the SNR gain stems from the area ratio of the lens. After these initial tests, a Lenz lens with area ratio 10 was placed into the incubation system. The Lenz lens is compared to the measurement set-up with out any signal amplification (reference), an LC resonator with the same inner coil diameter of 5 mm and a combination of the LC resonator and a Lenz lens. In the combination of the LC resonator and the Lenz lens a capacitor is mounted between inner and outer loop of the Lenz lens, which combines the flux collection capability with the resonance condition, it is thus named the resonant Lenz lens. The four set-ups were measured with a non-RF-spoiled FLASH sequence shown in fig. 3.24 with parameters TR = 200 ms, TE = 3 ms, slice thickness = 1 mm, FOV = 2 x 2 cm^2, MTX = 200 x 200 and NEX = 8.

Coronal and axial sections were recorded as depicted in fig. 3.24. As expected, the reference (ref) image shows the lowest signal-to-noise ratio of $\text{SNR}_i^{\text{ref}} = 16.4$. The r.f. resonator (LC) and the Lenz lens (LL) increase SNR by a factor of approx. 1.7, with $\text{SNR}_i^{\text{LC}} = 28.0$ and $\text{SNR}_i^{\text{LL}} = 27.4$. The increase in signal-to-noise ratio for this set-up is even more visible for the resonant Lenz lens (LLC), with $\text{SNR}_i^{\text{LLC}} = 38.5$ and thus a gain of approx. 2.3.
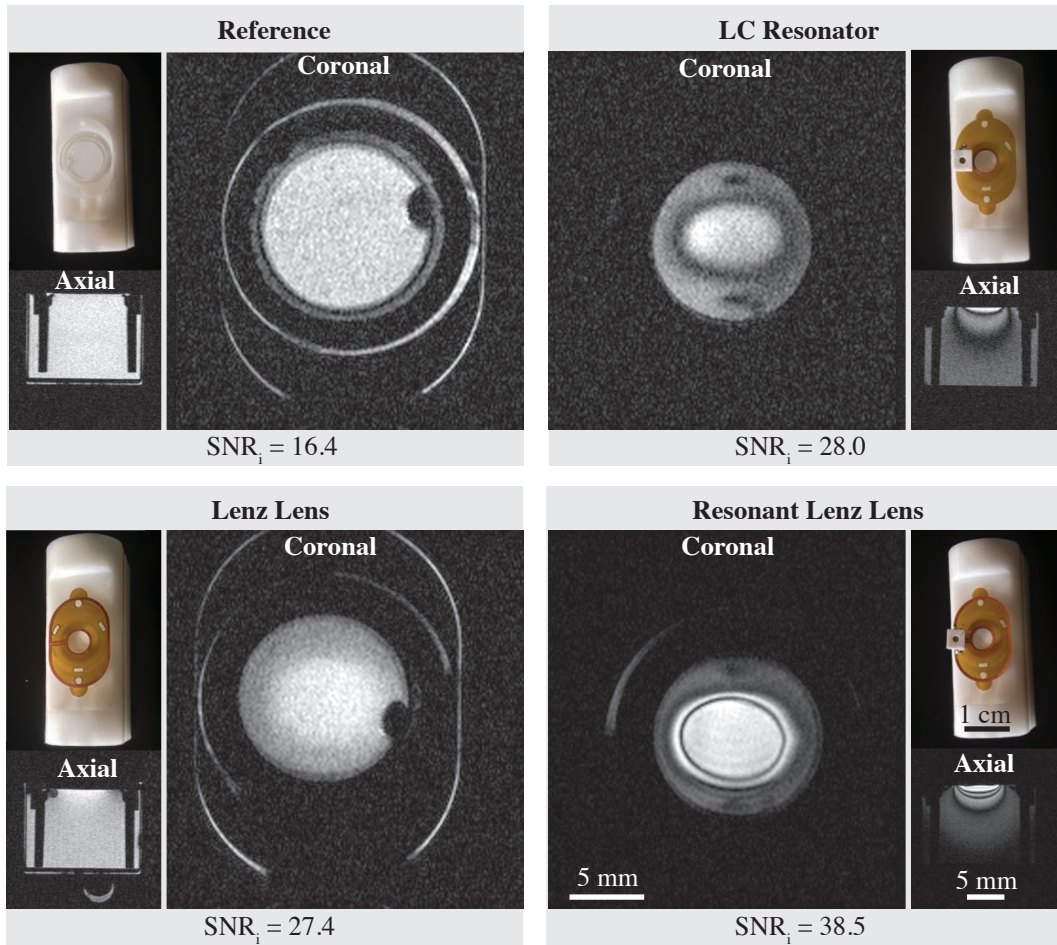
Fig. 3.24 Comparison of MR imaging using only a 72 mm volume coil (reference), an LC resonator, a Lenz lens and a resonant Lenz lens (all with an inner diameter of 5 mm). A non-RF-spoiled FLASH sequence was used with parameters TR = 200 ms, TE = 3 ms, slice thickness = 1 mm, FOV = 2 x 2 cm^2, MTX = 200 x 200 and NEX = 8.

3.5.7 Intermediate Conclusion Lenz lenses

This section introduced Lenz lenses as signal magnification method for magnetic resonance. First the concept of Lenz lenses was compared to a wired MR probe with small diameter, an LC resonator and a large Tx/Rx coil. As expected, the wire MR probe is the most efficient followed by the LC resonator. However, being broadband, the biggest Lenz lens with an area ratio of 81 still increased the SNR by a factor of 2 as compared to the Tx/Rx coil. The biggest Lenz lens was still less performant than the LC resonator that increased SNR by a factor of approximately 7-8.

For the MR incubator, Lenz lenses were manufactured whose base material is foil, which keeps substrate thickness to a minimum, to fit into the MR incubator. A custom process

was developed to manufacture these lenses. These Lens lenses were first used in a water filled tube and their MR signal profiles were extracted. They shown an MR signal increase of approximately 1.5 for Lenz lenses with an area ratio of 10.

A combination of LC resonator and Lenz lens, termed the resonant Lenz lens, is the most performant of the inductively coupled resonators. This has been verified in MR imaging experiments using the MR incubator. By comparing the SNR_i of the MR images, the superiority of the resonant Lenz lens w.r.t. the other inductively coupled resonators is apparent. The concept of the resonant Lenz lens is not in need of attaching cable, which lowers the risk of contamination in the MR incubator while being space efficient. However, one needs to be carful when using (resonant) Lenz lenses, since the calibration procedure needs to be adjusted to have the optimum signal at the region of interest (localised power adjustment).

4

MR compatible nurturing system for brain slice culturing

This chapter describes the implementation of an MR compatible nurturing platform for organotypic hippocampal slice cultures. A state of the art on magnetic resonance of brain slices is given. A technical characterisation of the MR incubator and a brain slice viability test concludes the chapter.

4.1   Introduction

Cultured brain tissue, either extracted from human patients or from mammalian specimen, is a vital part of neuroscientific research. Human brain tissue samples can be used to elucidate the pathology of different brain diseases at high resolution, as it can be investigated closely and over extensive time periods. As described in chapter 2.3, small animals are used as biological models for the progression of different brain diseases including epilepsy. However, as the aim of tissue fixation is to stop cellular processes and degradation, while the cytoarchitecture is preserved, the metabolism can not be resolved anymore. Additionally, since with fixation the chemical environment and composition of the tissue changes, so do the relaxation times and thus tissue contrast in magnetic resonance [62, 218–220]. This change in MR contrast and cell metabolism is especially of importance, when transferring findings from small animal models to the clinical diagnostics, as for example with quantitative markers for disease progression.

Although the life sciences discovered the potential of microtechnology, for example for brain-on-a-chip concepts [49, 60, 221, 222], for drug response testing [48, 223] and for electrophysiological measurements [224, 225], most publications deal only with acute brain slices, rather than cultured brain slices, and thus do not accommodate for patholog-

ical patterns.

Monitoring this disease progression is vital for understanding the disease and finding biomarkers for their onset. Therefore, we implemented a nurturing system, that allows for culturing of OHSC in the MR environment.

4.2 Magnetic Resonance Microscopy of brain slices and OHSC – State of the art

The MR monitoring of viable *ex vivo* cells and tissue has been gaining in momentum in recent years. Esteve *et al.* [59] introduced a cell culture system for simultaneous optical and MR monitoring of cells based on microfluidic nurture medium delivery. Their system incorporates environmental control of temperature, pH and oxygen in the nurturing medium and is designed for imaging and spectroscopy of single cells and cell clusters with a 14 T MR scanner. While it does support cell cultures, their system is not able to sustain viability of larger biological tissue.

In tissue engineering magnetic resonance is used to monitor and assess tissue regeneration, proliferation and development [226]. Thus there are a couple of devices, that allow for tissue to be grown inside an MR scanner [227–229]. One of the most sophisticated incubation systems for tissue engineering was introduced by Khalilzad-Sharghi and Othman *et al.* [55, 56]. The e-incubator is designed to fit into a vertical bore 9.4 T MR scanner, and the environmental parameters (temperature, CO2 levels, pH) are controlled by a microcontroller unit (see fig. 4.1 (i)). The microcontroller additionally controls fresh medium flow. The e-incubator is designed for longitudinal studies of engineered bone tissue and has real-time monitoring ability of the tissue growth, which is largely owed to the fact that bone grows slowly. However, the e-incubator is designed for vertical bore scanners, thus it is not possible to accommodate the interface culturing method necessary for prolonged viability of brain slices (see section 4.3).

Richardson *et al.* [63] introduced an incubation chamber capable of accomodating rat optic nerves. The chamber allows temperature and medium oxygen level control. As depicted in fig. 4.1 (ii) it consists of a chamber laser sintered from Polyamid, fitted with heating tubes and filled with oxygenated artificial cerebrospinal fluid (aCSF). Their system kept the rat optic nerve stable for up to 10 h while inserted into a 9.4 T vertical bore scanner. Although this incubation chamber is designed for the use with neurological tissue (e.g. the rat optic nerve), it is not capable of maintaining brain slices or OHSC viable.

Publications that deal with brain slices or brain slice cultures and bringing the necessary incubation environment to the MR scanner are rare. There are two systems currently

published that specifically deal with small animal brain slices. Flint *et al.* [67] showed an in-bore oxygenation and perfusion system for MR microscopy of tissue explants, that was tested with acute cortical rat brain slices (see fig. 4.1 (iii)). The perfusion system is designed for use in a vertical bore scanner system. There are two key features of this system that have to be highlighted. The brain slices are supplied with aCSF, that is flown through an oxygenation chamber just before entering the perfusion chamber where the brain slice is positioned. Therfore, the aCSF is oxygenised directly before being supplied to the brain slice. The perfusion chamber itself is directly mounted onto a 500 µm diameter Bruker surface micro coil (covering the brain tissue only partly), in which a woven nylon sheet gently pushed the brain slice onto the coil. Brain slice viability was tested for up to 15.5 h, where the stability of the MR diffusion signal was used as marker for viability.
Bai *et al.* [65] published a test bed for organotypic cortical brain slices. Their low field system (see fig. 4.1 (iv)), with a static field strength of 0.32 T, is based on the NMR mouse [230, 231]. The brain slice is inserted horizontally and nutrients are supplied by a flow of oxygenated aCSF. Dedicated r.f. coils ensure optimum sensitivity. The test bed is designed as an open system, thus enabling simultaneous MR, optical and electrophysiological measurements. To the authors knowledge, this is the only system currently published, that allows these kind of simultaneous measurements to be recorded. The test bed has subsequently been used by Bai *et al.* to elucidate one of the unanswered challenges on what underlies the functional MRI by correlating the neuronal activity (recorded by electrophysiology) with diffusion MRI [66]. While this is a vital contribution to the fundamental understanding of fMRI, and possibly other problem sets, this system comes with some drawbacks. Since at this stage, it does not incorporate a gradient system, only 1D experiments can be performed (where the slice is selected by physically changing the height of the brain slice w.r.t. the static magnetic field). Additionally when working with low fields, the findings are not directly transferable to clinical or higher field strengths.
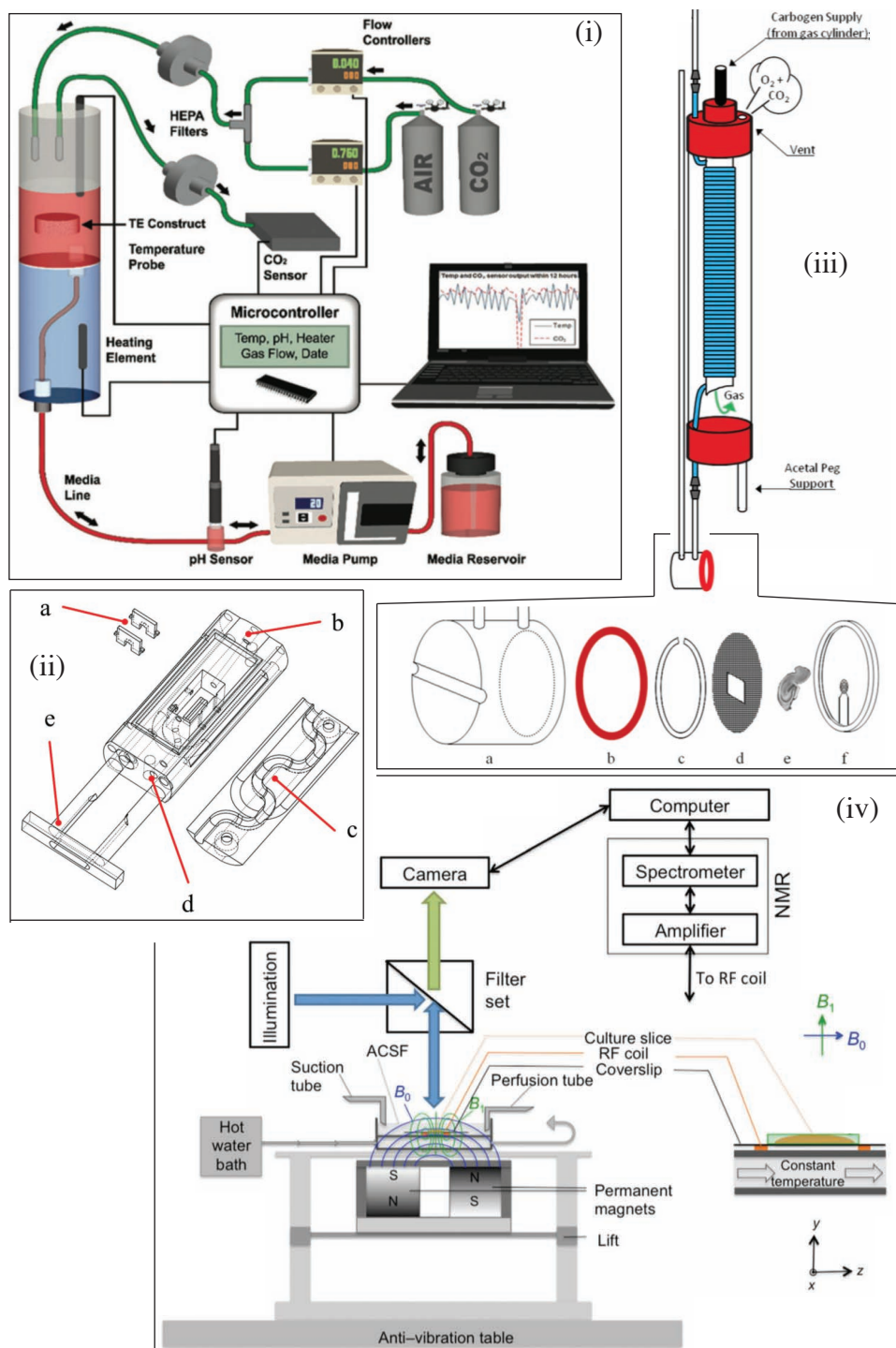
Fig. 4.1 The most significant MR compatible incubation systems. (i) The microcontroller controlled e-incubator for monitoring of engineered bone tissue reprinted from [55]. (ii) Incubation chamber for MR imaging of rat optic nerves reprinted from [63]. (iii) In-bore oxygenator for vertical MR systems for cortical rat brain slices reprinted from [67]. (iv) Open low field system for 1D MR measurements of cortical rat brain slices reprinted from [65].

None of these devices address organotypic hippocampal slice cultures (OHSC), or more general brain slice *cultures*. In the best case scenario, they use acute brain or acute brain slices with prolonged viability to up to 24 h. Brain slice cultures however, impose very specific requirements. (i) Cultivation means the brain slices are first dissected from a specimen, then transferred to a culturing dish and cultured in an incubation chamber. During culturing the brain slice may alter it's morphology, shape and metabolism specific to the induced pathology one wants to investigate (on our case epileptogenesis). This means, the slice needs to be kept viable over at least two weeks, for disease progression to reliable form. (ii) Since the cultivation takes weeks, sterility of the system is vital. If it is not achieved, brain slice cultures die within hours to days. (iii) During the culturing period, the brain slices are thinning, thus from an original thickness of 400 µm a slice will shrink to a thickness of only 100 µm. Additionally, cutting of the brain slices effects their interface layers so the exposed neurons are killed, leaving viable tissue at a thickness of approx. 80 µm.

These requirements lead to the construction of the incubation chamber as described in the following section. The approach of this thesis is to use the most common brain tissue culturing method (namely the interface culturing method [232]). By designing a modular culturing platform, it is possible to culture tissue in the laboratory incubation chamber, and transfer it to a dedicated MR compatible incubation platform, designed to work in a small animal, horizontal bore MR scanner system. Importantly, the tissue can be re-introduced into the laboratory incubation chamber after an MR measurement, to allow further cultivation of the same brain slice.

4.3 Design

A significant part of this section on the MR compatible nurturing platform was presented in [RK11, RK13, RK15] [a].

---

[a]Contributions: *RK:* Process development, design and manufacture of hardware, MR measurements, data analysis, manuscript concept and writing. *KG:* MR data acquisition and processing, proofread manuscripts. *JG:* Sample preparation, interpretation of data, proofread manuscript . *OGG:* Process development, manuscript concept, proofread manuscript. *PL:* Development of MR data processing, proofread manuscript. *JL:* MR measurement optimisation, MR data acquisition. *DvE:* Evaluated MR methods. *J. Hennig:* Evaluated MR methods, MR sequences, proofread manuscript. *C. Haas:* Interpretation of data, proofread manuscript. *JGK:* Data interpretation, proofread manuscript.

The MR compatible incubator designed, built and tested during this thesis is specifically designed to accommodate organotypic brain slice *cultures* to monitor epilepto-

genesis *in vitro* in longitudinal studies of the same OHSC. There are various methods to culture brain slices [42], where the method keeping OSHC viable the longest is the interface culturing method [40, 232, 233].

In the interface culturing method, the slice is placed onto a membrane. A culturing container is filled with nurturing medium up to this membrane, and the whole set-up is kept in a controlled gas environment (temperature, gas and humidity controlled). This interface between gas and medium ensures that the brain slice is optimally supplied with nutrients from the nurturing medium, while having maximum exposure to oxygen in the gas phase, thus avoiding necrotic cell death due to oxygen deprivation. Cultivation of up to 6 months has been demonstrated with this method [234, 235]. Due to these reasons, the MR incubator relies on the interface culturing method. The MR incubator needs to meet the following requirements:

- The interface culturing method as method of choice for long term slice culturing is used (needs an interface with a controlled gas atmosphere).

- Since the slices will be monitored over several weeks, it has to be possible to cultivate the OHSCs in a laboratory incubation chamber in between MR scans.

- The incubator needs to be sterile during MR measurements.

- Temperature has to be stable over the course of the MR scan.

4.3.1 Version 1

The first version of the MR incubator consist of three central parts: A Millicell® culture plate insert, which is placed into milled PMMA inlet (see fig. 4.2). The PMMA inlet is fitted to the MR incubator platform and covered with a PI foil (not shown in the image) to avoid gas evaporation.

Hippocampal slices are cultured in a laboratory incubation chamber on the sterile 12 mm Millicell® culture plate insert PICM01250 (*Merck GmbH, Germany*) with a hydrophilic biopore PTFE membrane and 0.4 µm pore size before being transferred to the MR incubator. The PMMA insert, milled with a 4030 CNC mill (*isel Germany GmbH, Germany*) with parameters given in appendix E.1, is designed to fit the Millicell®inlet and avoids a 90° interface orthogonal to the B_0 field to minimise MR imaging artefacts. PMMA was used, since it is clear and has a susceptibility close to water [236]. PMMA inlet and culturing insert are placed into the MR incubator platform. The MR incubator platform is

extrusion printed from Acrylonitrile butadiene styrene (ABS) filament (*Makerbot Industries LLC, USA*) with the 3D printer Makerbot Replicator 2X (*Makerbot Industries LLC, USA*).

Initial testing of this first version of the MR incubator revealed central issues which render this device disadvantageous for MR measurements of tissue slices. Due the manufacturing method, the 3D printed MR incubator platform has long and thin material grooves. These grooves are prone to harbour dirt and bacteria. Since ABS and PMMA is not autoclavable, tissue sample were regularly contaminated, which renders longitudinal studies infeasible.

An additional issue with this version was that the nurturing medium was sucked out of the PMMA inlet. Presumably this happened, since the PMMA inlet was filled with nurturing medium up to the top, and the crack between
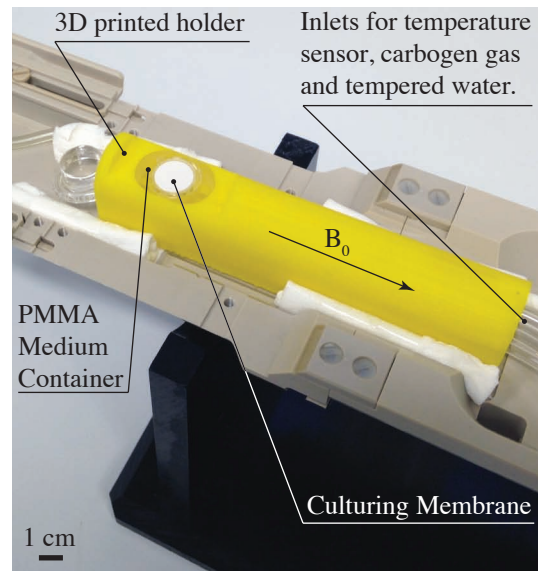
Fig. 4.2 Version 1 of the MR incubation platform.

PMMA and ABS in combination with the grooves in the ABS sucked the nurturing medium into the ABS holder due to capillary forces. Therefore, as depicted in fig. 4.3, nurturing medium vanished rapidly from the PMMA inlet (within the time course of 30-45 min). The resulting air bubble leads to a fast drying of the tissue slices and strong MR imaging artefacts. Scan times longer than 30 min were not possible with this device.
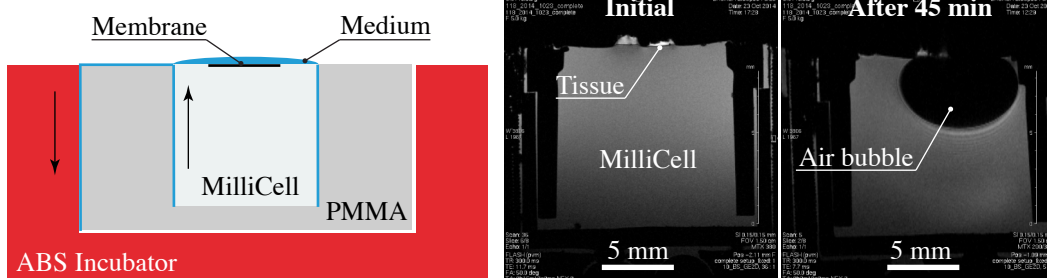
Fig. 4.3 The nurturing medium is presumably sucked out of the PMMA inlet by capillary forces. This leads to rapidly vanishing nurturing medium.

4.3.2 Version 2

Version 2 of the MR incubator is shown in fig. 4.4. The heart of the incubator is a Poly-oxymethylen (POM) inlet milled with a 4030 CNC mill (*isel Germany GmbH, Germany*) with milling parameters given in appendix E.4. The POM inlet accommodates a 12 mm diameter Millicell®-PICM01250 insert (*Merck Millipore, Germany*). The Millicell®has a hydrophyilic PTFE membrane, with a pore diameter of 0.4 µm which is commonly used to culture OSHC, so that the culturing protocol does not need to be changed. However, it is used upside-down to it's intentional use, with the membrane aligned on the top level, so that the OSHC is at the topmost position, which is closest to the r.f. coil of the MR scanner, thus enabling significantly better SNR during the measurement.

The insert is placed into the POM inlet. A technical drawing of the POM inlet is depicted
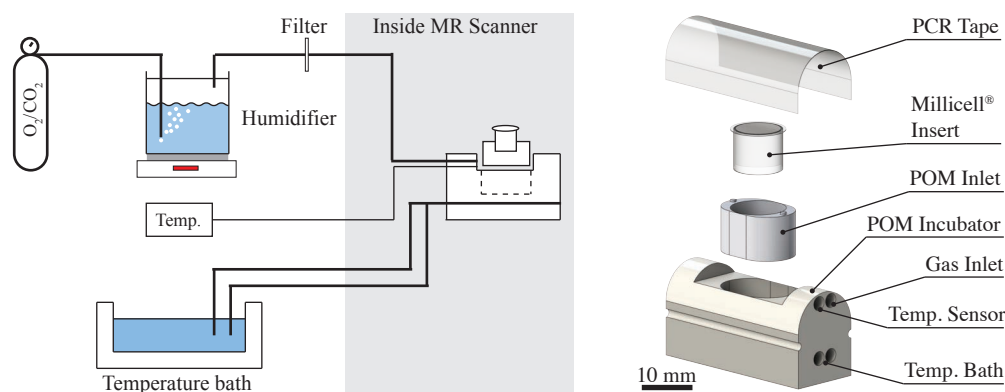
Fig. 4.4 Left: Schematic of the MR compatible nurturing system for brain slice culturing, incorporating a humidified gas supply, a temperature bath for temperature control and the MR incubator itself. Right: Exploded view of the MR incubator.

in appendix G. During cultivation and MR measurements, the POM inlet is filled with nurturing medium prepared from a mixture of basal medium eagle (BEM) (1X) liquid (*Thermo Fisher Scientific Inc., USA*), mimimum essential medium (MEM) (*Thermo Fisher Scientific Inc., USA*) and B27 supplement (*Thermo Fisher Scientific Inc., USA*). The POM polymer was chosen for three main reasons. (i) It does not induce artefacts in the MR measurement, since it's magnetic susceptibility is close to that of the nurturing medium (as compared to e.g. a metal inlet). (ii) It is extremely well machinable with substractive manufacturing methods (e.g. milling), and (iii) POM is a polymer capable of sustaining high temperatures and thus can handle a standard autoclave procedure for sterilisation (15 min at 121 °C).

The Millicell®insert and the POM inlet are placed into the POM incubator. This POM incubator has a gas inlet for carbogen gas (95 %/5 % O_2/CO_2) and for a temperature sensor.

Carbogen gas (*Linde AG, Germany*) is chosen, since its high oxygen content of 95 % ensures maximum exposure of the OSHC to oxygen (which is deliverd by gas phase diffusion into the tissue). The 5 % carbon-dioxide gas stabilises the nurturing medium to a pH-value of 7.4 (carbon dioxide - bicarbonate buffer system), which is essential for the OHSC to stay viable. The POM incubator additionally allows for external temperature stabilising water tubing to be connected through the bottom of the device. The autoclavable 1.6 mm outer and 0.8 mm inner diameter Tygon® S3$^{\text{TM}}$ E3603 water tubing (*Carl Roth GmbH & Co.KG, Germany*) is connected to a Bruker small animal bed, which in combination with a temperature sensor allows for temperature control of the MR incubator. The MR incubator is sealed off with sterile self-adhesive Rotilabo® polypropylene PCR tape (*Carl Roth GmbH & Co.KG, Germany*), to allow an controlled gas atmosphere, reduce drying and avoid external contamination. A layout of the MR incubator can be found in appendix H. Since the carbogen gas applied to the MR incubator is directly supplied by a gas bottle, it is fed through a heated bath filled with autoclaved water. This feed through humidifies the gas to avoid drying out the nurturing medium, and thus killing the OHSC. It is additionally equipped with a 0.45 μm pore size 25 mm diameter sterile PTFE membrane air filter (*Carl Roth GmbH & Co.KG, Germany*), to avoid contamination of the gas supply.

There were several challenges arising during the testing of the MR incubator version 1. Some challenges were solved by the redesign of the MR incubator. Over the incubation period of several hours, the nurturing medium evaporated and was sucked out of the insert by capillary forces through the slit between PMMA inlet and ABS incubator. The vanishing medium is an application killer, since it leaves air bubbles directly under the OHSC, which induces huge imaging artefacts, making MRM imaging hardly possible. Additionally, the OHSC dries out completely, thus it kills the tissue from oxygen deprevation, which makes the *in vitro* tracking impossible. Both of these issues were addressed, by (a) switching from a PMMA to a POM insert and making a deeper inlet and (b) adding a humidifier to the gas flow. The deeper POM inserts ensure, that the Millicel®inserts are lower w.r.t. to the upper interface of the POM inlet. Therefore, the risk of overflowing the nurturing medium is reduced. The humdifier for the gas flow, saturates the carbogen gas up to 75 % relative humiditiy, therefore reducing the drying effect further.

4.4   Standard Operating Procedure

A significant part of this standard operating procedure for MR imaging of tissue with the interface method will be submitted to the Journal of Magnetic Resonance Imaging as [RK1][a]

[a]Contributions:*RK*: Process and hardware development and design, MR data acquisition, data processing, analysis and interpretation, manuscript concept and writing. *KGG:* MR data acquisition. *JG:* Tissue preparation, tissue stainings and data interpretation. *OGG:* Data interpretation, manuscript proofread. *JH:* MR methods development, manuscript proofread. *PL:* Data processing methods, proofread manuscript. *CH:* Data interpretation, proofread manuscript. *JGK:* Data interpretation, manuscript concept, proofread manuscript.

The redesign did not resolve the artefacts induced by air bubbles from filling nurturing medium into the container, and from artefacts induced by the small interface from the side of the OHSC that is orthogonal to the B0-field. Both of these artefacts were reduced by the use of a standard operating procedure for the filling the POM inlet. The protocol is as follows:

1. Place the (sterilised) POM inlet and the Millicell®insert (with membrane attached OHSC) in a clean medium filled container, so that both are fully submerged in medium

2. Make sure, there are no air bubbles attached to the POM inlet or the Millicell®insert.

3. In the medium, place the Millicell®insert into the POM inlet (without touching the membrane), and turn the set-up membrane up.

4. Take out the POM inlet, with Millicell®insert inside, and dry off medium from the sides of the POM inlet

5. Place POM inlet into the MR incubator

6. Overflow the membrane with nurturing medium to level with the upper interface of the OHSC with gas.

7. Seal MR incubator with sterile tape and insert into the MR scanner

This operating procedure significantly reduces artefacts in the MR images, as is shown in fig. 4.5. The B_0 field distribution was simulated with Maxwell 16 (*ANSYS Inc., USA*) and an applied static magnetic field of $B_0^{\text{Sim}} = 7\,\text{T}$. For the simulation, air was assumed as gas with $\chi_{\text{Air}} = +0.4\,\text{ppm}$ and water as medium with $\chi_{\text{Water}} = -9.0\,\text{ppm}$. The brain tissue was approximated with a difference of -2.0 ppm to water with $\chi_{\text{Brain}} = -11.0\,\text{ppm}$, as indicated

in [237]. The brain tissue is modelled as a 2x3 mm rounded 400 µm thick tissue slab. The water/medium container is a 10 mm diameter, 10 mm deep cylinder. For the improved method, the medium-brain slice miniscus is approximated by a cut off cone of water, with the upper edge aligned with the brain slice. A sagittal cut of the simulation shows the ΔB_0 field distribution as difference from $B_0 = 7\,\text{T}$ in ppm. As can be seen from fig. 4.5 a, when the brain slice lays flat on the water, without the medium meniscus (as is the case for the interface culturing method), a strong shift in of up to $\Delta B_0 = -8.0\,\text{ppm}$ is visible at the edges of the brain slice. This shift radiates into the slice and the medium from the edges of the brain slice. This shift results in an artefacts, which are visible in the MR non-RF-spoiled FLASH images (fig 4.5 b and c). When the medium cone/meniscus closes off with the top surface of the brain slice, this behaviour is much less pronounced in the simulation of fig. 4.5 d and the coronal MR image of fig. 4.5 f. In the sagittal MR image of the improved method (fig. 4.5 e) the artefacts completely dissapear and thus it can be concluded that the improved method indeed efficiently reduces artefacts and makes imaging of the brain slices with the improved interface culturing method possible.
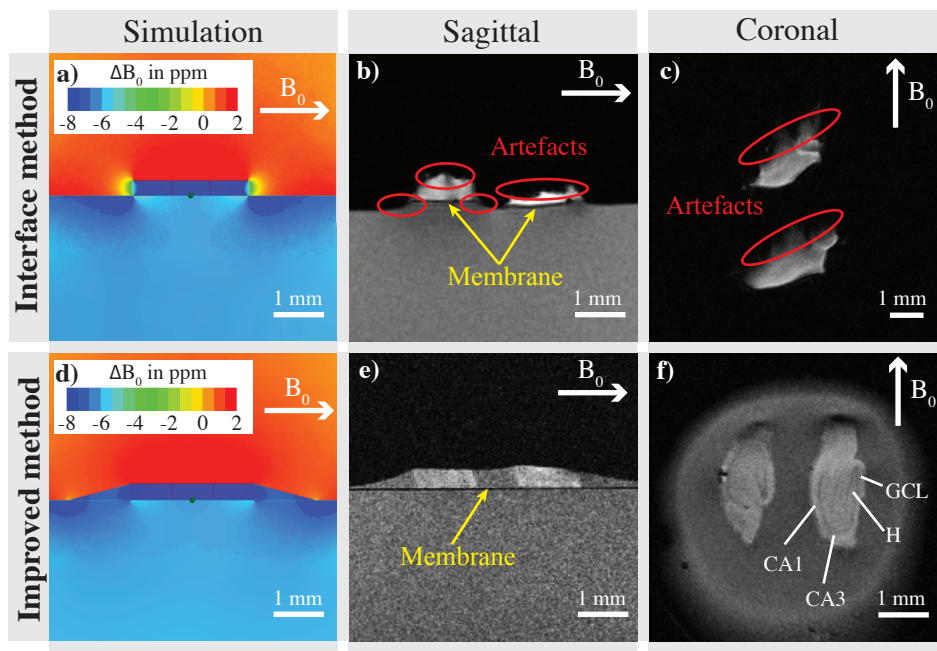
Fig. 4.5 Simulation of the B_0 field distribution shows a strong shift of the magnetic field for the interface method (a), which is less pronounced for the improved method (d). Non-RF-spoiled FLASH images show artefacts in the sagittal (b) and coronal (c) MR images, when using the standard interface method of cultivating OHSC, where the nurturing medium is filled to just touch the culturing membrane. These artefacts are reduced when using the handling protocol, to fill the nurturing medium levelled to the top interface of the OHSC and reduces artefacts in the sagittal (e) and coronal (f) MR images.

4.5 Technical Characterisation

In this section technical parameters of the MR compatible incubation system (Version 2) are assessed. Temperature profiles in different settings were recorded. The oxygen level and the relative humidity were measured at different points in the set-up: (i) from the carbogen gas supply, to the humidifier (ii) and finally to the incubation system itself (iii). Temperature profiles were measured over a time period of 5 h and at a room temperature of 22.3 °C. Three different temperature profiles were recorded. Two of which were the temperature profiles in the nurturing medium of the incubation system, (i) starting with nurting medium at room temperature and (ii) starting with the nurturing medium directly taken from an incubation chamber at 37 °C. For both medium measurements, the temperature bath (small animal temperature bed, *Bruker BioSpin GmbH, Germany*) was set to its maximum temperature of 63 °C and the room temperature was measured at 22.3 °C. As the graph of fig. 4.6 depicts, both temperature profiles stabilise at around 32.2 °C for starting at room temperature after 30 min and for starting from 37 °C after 20 min respectively. The third temperature profile was recorded in the gas atmosphere of the incubation chamber. For this measurement, the gas inflow was switched on, and led through the humidifier. The humidifier, an autoclaved water tank placed on a heater plate, started from room temperature and was set to a target temperature of 65 °C. The gas temperature started from 19.3 °C when the humidifier bath is at room temperature of 22.3 °C and stabilises at 24.0 °C when the humidifier bath is at 65 °C.
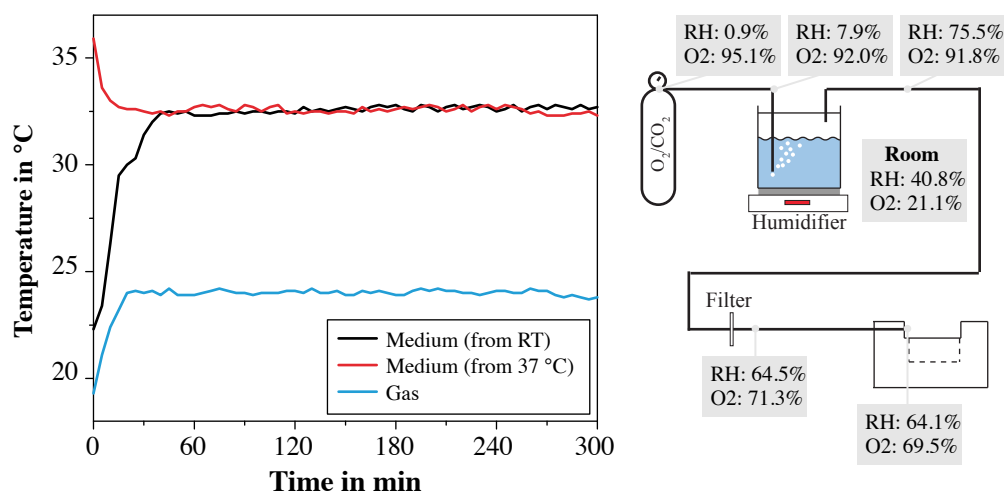

Fig. 4.6 Left: Temperature profiles of the nurturing medium in the incubator and the carbogen gas, wich stabilises over time. Right: Relative humidity (RH) and oxygen content (O2) of the gas supply at different points of the set-up.

9 The relative humidity (RH) and the oxygen content (O2) in the gas supplied to the MR incubator were measured at different points in the set-up. As shown in fig. 4.6 these point were: Directly at the carbogen gas bottle (RH:0.9 %, O2:95.1 %), before the humidifier (RH:7.9 %, O2:92.0 %), after the humidifier (RH:75.5 %, O2:91.8 %), after the sterile filter (RH:64.5 %, O2:71.3 %) and in the incubator (RH:64.1 %, O2:69.5 %).

4.6   Brain tissue survival tests

All tissue stainings and microscope images in this section were done by Johannes Gerlach or Catarina Reis Orcinha of the Experimental Epilesy, Department of Neurosurgery, University Hospital Freiburg.

After assessing its technical performance, the ability of the nurturing system to keep brain slices alive is to be tested. These tests should ensure its usability in a neuroscientific context. It is, however, not trivial to evaluate whether the brain tissue is kept viable, and if it is not viable, what the cause of cell death is. There are multiple reasons for cell death in a brain slice during culturing. Reasons may be hypoxia (oxygen deprivation), too much oxygen after slight hypoxia (hyperoxia by reperfusion [238]), exploited nurturing medium (shortage of nutrients), high temperature (proteins degenerate), low temperature (forming of ice crystal hurts cell membranes), pH-value shift of the nurturing medium (away from pH 7.4), mechanical shock or vibration [144, 239] and contamination of the culturing system. Obviously any combination of these might also lead to cell death, which makes the identification of the cause of death extremely challenging. Two approaches to test tissue viability were considered, (i) using classical tissue staining techniques, as introduced in chapter 2.3.5, and (ii) using diffusion weighted imaging.
Both of these techniques come with certain trade-offs. Since with staining techniques every cell is marked, its optical read out gives a very accurate count for dead and alive cells in the tissue. Additionally, to some extend the source of cell death can be determined. For example, necrotic cell death (as introduced by hypoxia) gives other signal distribution than a diffuse cell death. However, the staining protocols needs to be adapted to work reliably, which is time and labour intensive. Additionally, the tissue can not be cultivated further once it was stained, an thus this method does not allow for a continuous tracking of tissue viability, but rather a point by point check of different tissue slices.
Diffusion MR methods on the other hand provide the possibility to measure the tissue culturing in situ and continuously. However, a reliable MR protocol needs to be set-up, which is especially challenging for very thin tissue slices. Although a link between diffusion signal change and tissue viability has been proven in stroke patients [240], it is not an

absolute measure, and thus tissue comparability suffers, and it was therefore decided to validate the MR incubator performance by histological stainings.

A measurement series was set-up to evaluate the functionality of the MR incubator. Hippocampal slices were prepared from three days old C57BL/6 mice (p3) and cultivated for 14 days. After 14 days *in vitro* (14 DIV), the slices were placed into the MR incubator. For the first set of 3 hippocampal slices (negative control), the MR incubator was switched off, and kept in a sterile bench for 8 h. The second set of hippocampal slices was mounted into the small animal horizontal MR scanner at 7 T static field strength, the MR incubator was switched on. After 8 h the hippocampal slices were removed.
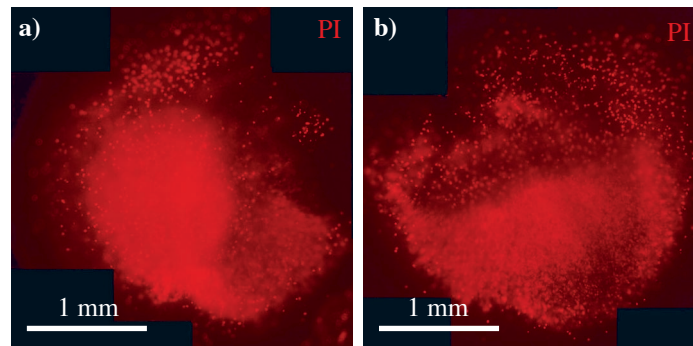
Fig. 4.7 Propidium Iodide (PI) stainings of negativ control hippocampal slices. a) and b) shows a central necrosis of cells (cloudy red background signal, generated by out of focus dead cells in the slice). This central necrosis is likely caused by oxygen depression (as wished for in the negative control).

Both sets of slices were stained with Propidium Iodide (PI) according to the protocol given in [134] directly after the 8 h period. PI, a polar compound, only enters cells with damaged cell membranes and binds into the nucleic acid, thus staining only dead cells. As shown in fig. 4.7, the negative control hippocampal slices that were kept in the switched-off MR incubator, show a central necrosis of the cells. The central necrosis can be seen from the cloudy red signal in the slice centre caused by out of focus dead cells in the hippocampal slice. The central necrosis likely indicates cell death from oxygen deprivation, since the oxygen diffusing to the centre of the slice does not suffice to stabilise slice viability. This behaviour is expected in the negative control of the experiment.

In the hippocampal slices, that were placed into the active MR incubator and put into the MR scanner, the PI staining indicates a diffuse cell death, but no central necrosis (as can be seen in fig. 4.8). This diffuse cell death is normal in hippocampal slice cultures and thus does not indicate stronger cell death than would be normal in an incubated slice culture. Additionally, the neuronal nuclei stain (NeuN) indicates that the laminarity of the

hippocampal slice sections was not compromised during the measurement, validating their viability.

Since these tissue survival tests were done only on a small number of tissue slices, a final evaluation of the nurturing platforms performance will need additional test, that should ideally be verified by another method (i.e. DWI during cultivation).
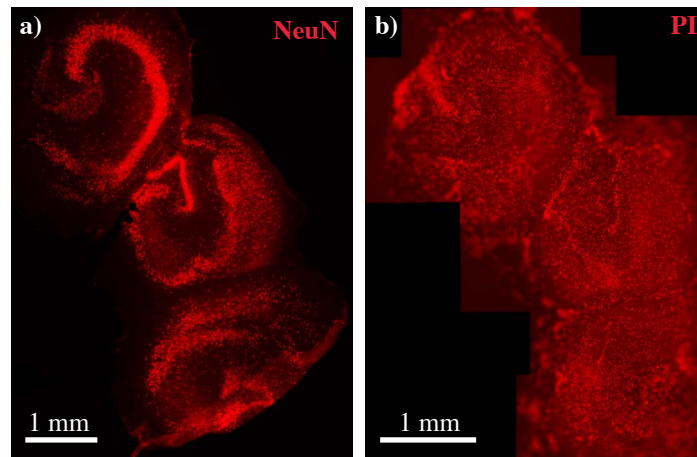
Fig. 4.8 Stainings of three hippocampal slices. a) Staining of the neuronal nuclei (NeuN), showing the main cell layers to be intact. In b) there is diffuse cell death. In diffuse cell death, the cells die everywhere in the slice, indicating they did not die from oxygen deprivation, but other factors. Note that in this staining, the neuronal nuclei are stained in red, as is the Propidium Iodide (cell death) staining.

4.7   **Intermediate Conclusion Nurturing System**

An MR compatible nurturing system (MR incubator) was built, to accomodate the interface culturing method in the MR scanner, thus allowing for the (longitudinal) measurement of organotypic hippocampal slice cultures (OHSC). This capability distinguishes the MR incubator from the systems already published, that deal with *acute* organotypic tissue slices. As the MR incubator is based on the interface culturing method, challenges were encountered due to the part of the interfaces of the OHSCs that are not in parallel with the B0 field. Although these interfaces are low (< 400 μm), they still induce strong artefacts. These challenge was overcome by introducing an improved method and a standard operating procedure, in which the slices are filled up to their top to reduce susceptibility jumps from nurturing medium to tissue. While this results in an acceptable MR image quality, where substructures in the brain slice cytoarchitecture can be identified, it complicates handling and repeatability of the experiments.

Temperature profiles were taken of the medium and the gas atmosphere. Although the temperature of a laboratory incubation chamber (37 °C) was not achieved, the main contribution was to keep the temperature stable for an controlled environment, which was proven. However, since the gas atmosphere poses a temperature gradient to the medium (gas stable at approx. 24 °C, medium at approx. 32 °C), this may lead to additional stress in the OHSC.

The humidity measurements show, that the humidifer increases the relative gas humidity (RH) to 75 %, but some of the humidity if filtered out by the sterile filter. Therefore the gas supplied to the MR incubator at 65 % relative humidity dries the medium container over time. MR measurements for up to 5 h were working well, but the drying effect became relevant for longer experiments, thus limiting the safe scan time. Tests of the oxygen levels in the gas indicate, that along the set-up some oxygen content is lost, and it drops from 95 % to just below 70 %. While this oxygen content is sufficient to supply the OHSC, as long as it is constant, it would be important to know the CO_2 level, since it is used as a pH buffer for the nurturing medium. If the pH level shifts, the OHSCs will die eventually.

The brain slice survival tests show the MR incubator's general functionality, but these tests are not conclusive. As concluded the PI stainings, hippocampal slices were dying from other causes than oxygen deprivation in the negative control, which should be the primary cause of cell death, since it is the fastest. This indicates, that there might be more issues to deal with when implementing this system on a larger scale. Moreover, since the slices are transferred from the laboratory incubation chamber to the MR incubator and back, sterility can not be guaranteed all the time. Additionally, the hippocampal slices are very sensitive to mechanical stress and vibration, thus carrying the slice cultures around, mounting them into the MR scanner and back again may compromise slice integrity, and unintentionally induce epilepsy on its own. This may be an issue, when transferring the MR incubator to be used in tranlsational studies of the same slice culture. To the authors knowledge, translational studies of the same slice have never been done before, but only studies in acute slices. Obviously most of the encountered challenges will not be an issue in experiments with acute slices (except oxygen deprivation), but will also not give the opportunity to follow disease progression closely.

5

Application of MRM Tools to Neuroscientific Research

In this chapter the method of virtual staining as a tool in neurological research is introduced and applied to fixed brain slices of healthy and epileptic mice. Brain tissue measurements obtained with the Lenz lenses and the MR compatible nurturing platform are presented.

Ethics Statement

All animal treatments, tissue dissections, tissue preparations and histologic and immuno-histochemical tissue stainings presented in this thesis were executed by Johannes Gerlach or Catarina Reis Orcinha of the Experimental Epilepsy, Department of Neurosurgery, University Hospital Freiburg headed by Prof. Dr. Carola Haas.

All animal procedures were performed in accordance with the guidelines of the European Community's Council Directive of September 22, 2010 (2010/63/EU) and approved by the regional council (Regierungspräsidium Freiburg) and local animal welfare officer, according to the German animal protection act.

5.1 Magnetic Resonance Microscopy and tractography of fixed hippocampal slices – Virtual staining

This section on virtual staining using DTI in fixed hippocampal slices was developed in a strong collaboration of Robert Kamberger (hardware development and manufacturing, MR data acquisition), Katharina Göbel-Guéniot (MR methods (DTI and DWI) development, MR imaging, data processing and interpretation) and Johannes Gerlach (sample preparation, stainings and interpretation of data) and will be submitted to NeuroImage as [RK2][a].

---

[a]*KGG:* MR method development, MR imaging, data processing, data interpretation, manuscript concept and writing. *JG:* Tissue preparation and stainings, interpretation of data, manuscript concept and writing. *RK:* Hardware development and manufacturing, MR data acquisition, manuscript writing and proofreading. *DvE:* MR method optimisation, proofread manuscript. *JH:* MR method optimisation, proofread manuscript. *JGK:* Manuscript concept and proofread. *C. Haas:* Data interpretation, proofread manuscript. *PL:* Data interpretation, MR methods, manuscript concept and proofread.

The aim of imaging fixed hippocampal slices was to determine which level of cytoarchitecture and which pathogenic changes towards chronic epilepsy (specifically mesial temporal lobe epilepsy - MTLE) can be visualised. Therefore fixed sections act as standard sample, since the same slice can be imaged multiple times, and protocols can be adapted to it. Aside from directly resolving tissue structure with a CPMG-RARE sequence, diffusion tensor imaging and tractography was used for its superresolution and its ability to indicate connectivity, thus *virtually staining* the tissue (a method also known as MR histology [241, 242]). Slices from healthy and chronically epileptic animals are virtually stained to investigate how the signal corresponding to the tissue structure changes after chronic epilepsy has developed. To validate the MR and tractography images, histological and immunohistochemical stainings were performed subsequently. Neuronal nuclei (NeuN) and granule cell axons (ZnT3) were stained with sepcific antibodies, as they are central to the hippocampal circuit.

All fixed tissue measurements were done on 400 µm thick hippocampal slices. Healthy slices were prepared from mice at postnatal week 8-9 and epileptic slices from kainate injected mice. All epileptogenic hippocampal slices shown in this thesis are prepared from kainate (KA) injected male adult mice (C57BL/6N or Thy1-eGFP mice). KA was injected into the right dorsal hippocampus. The mice were anaesthetised, and 50 nl of 20 mmol KA solution in saline were injected with a micro-pump. After surgery, the mice were observed for several hours to verify behavioural status epilepticus (SE), by mild convulsive movements, chewing, rotations or immobility. Tissue samples were prepared 21 days after

Table 5.1 MR imaging parameters used for CPMG-RARE and tractrography of fixed hip-
pocampal slice sections.

Parameter	RARE	DTI
TR	2000 ms	3000 ms
TE	51 ms	39 ms
RARE factor	6	–
Slice thickness	$100 \, \mu m$	$100 \, \mu m$
MTX	512 x 480	320 x 190
Resolution	$20 \times 24 \, \mu m^2$	$39 \times 39 \, \mu m^2$
NEX	32	16
b-value	–	$1000 \, s \, mm^{-1}$
# b=0 images	–	6
Segments	–	4
Directions	–	60
Scan time	1 h 25 min	3 h 31 min

KA injection from mice in the chronic epilepsy phase. At this time point, the morphologi-
cal changes of epilepsy pathogenesis are fully developed. The hippocampal slices were
immersion-fixed in 4 % PFA at 4 °C for 12 h and rinsed in phosphate buffer (PB) before
MR measurements. For the MR measurements, the slices were placed into a fitted PMMA
container glued onto a custom 3D printed ABS holder that ensures close proximity to the
quadrature cryoprobe[1]. The whole PMMA container was flooded with saline solution
and sealed with sterile PCR tape for the MR measurements to avoid artefacts and slice
dehydration.

For testing the method of virtual staining two types of fixed hippocampal slices were
tested: (i) Healthy hippocampal slices (control) and (ii) hippocampal slices from kainate
(KA) injected mice sacrificed in the chronic phase of epilepsy. All of these hippocampal
slices were recorded with the MR parameters summarised in table 5.1 and the results of
these measurements are depicted in fig. 5.1.

In the healthy control slice, several features of the cytoarchitecture can be identified in
the CPMG-RARE images shown in fig. 5.1 a. The principal neuronal cell layers of cornu
ammonis (CA1 and CA3 pyramidal cell layers) and the granule cell layer can be identified,
since these consist of densely packed neuronal cell bodies. Additionally the molecular
layer (ML), the stratum oriens (SO), the stratum radiatum (SR) and the hilus (H) are clearly
visible in the control slice. In the tractography images, anisotropic diffusion is visualised

---

[1]This is not the MR incubator described in chapter 4

in the SR of CA3, where mossy fibers extend and innervate the CA3 pyramidal cells. Additionally the SO from hippocampal long-range projections are visible. Tractography of the mossy fibers is verified by ZnT3 staining (fig 5.1 c) marked by the small arrow heads. The CA1, SR and stratum lacunosum moleculare, positioned between ML and SR, show additional anisotropy. Their signal from the CA3 pyramidal cell axons (the Schaffer collaterals) lies orthogonal to the direction of the vertical signal of the CA1 pyramidal cell dendrites (red color code, marked by the asteriks in fig. 5.1 b))
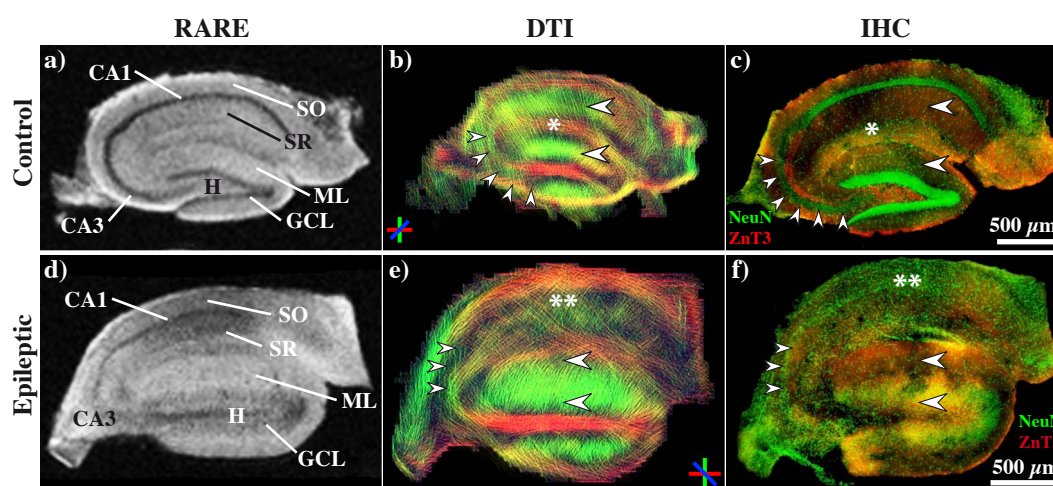
Fig. 5.1 CPMG-RARE (a and d), DTI (b and e) and immunohistochemical (c and f) images of hippocampal slices of from a healthy (control) and a KA injected mouse (epileptic). In the healthy slice, the key cytoarchitecture can be identified. These are, cornu ammonis (CA1 and CA3) pyramidal cell layers, granule cell layer (GCL), molecular layer (ML), stratum oriens (SO), stratum radiatum (SR) and hilus (H). By comparing the control and the slice of an epileptic animal a number of changes can be identified. The cell layers of CA1 and CA3 degenrate (a and d), the granule cell layer (GCL) disperses (large arrow heads in b vs e), the Schaffer collaterals degenerate (single asteriks b vs e) and mossy fibers srpout into the GCL and into remaining CA2 pyramidal cells (small arrow heads in c and e). MR image acquisition and data processing by Katharina Goebel. Tissue preparation/stainings and data interpretation by Johannes Gerlach.

For the evaluation and comparison of the two different kinds of hippocampal slices, special attention was paid to the areas of the hippocampus that show significant changes from healthy to chronic epileptic tissue. The changes that can prominently identified are:

1. The pyramidal cell layers of CA1 and CA3 degenerate (fig. 5.1 a vs. d)

2. The granule cell layer (GCL) disperses (fig. 5.1 a vs. large arrow heads in e)

3. The Schaffer collaterals (CA3 axons innervating CA1 dendrites) and the CA1 dendrites degenerate (single asteriks in fig. 5.1 b vs. e)

4. Sprouting of the mossy fibers (GCL axons projecting into CA3) (small arrow heads in fig. 5.1 b vs. e).

5.2 Magnetic Resonance Microscopy of acute hippocampal tissue

In the last section 5.1 fixed hippocampal slices were investigated to benchmark which hallmarks of the hippocampal cytoarchitecture and their alteration with epileptogenesis can be resolved. Subsequently viable acute hippocampal slices were measured. These were mounted in the MR incubator, to ensure a prolonged viability of the tissue.

The hippocampal tissue was dissected from a p4 mouse, cut into 400 µm slices, positioned onto a Millicell®inlet and placed into the MR incubator (filled with nurturing medium). The whole set-up was put into the 7 T horizontal bore MR scanner (*Bruker BioSpin GmbH, Germany*) directly after mounting the tissue into the MR incubator. A non-RF-spoiled FLASH image with the parameters given in appendix I was subsequently recorded.

In the acquired non-RF-spoiled FLASH image, as depicted in fig. 5.2, the gross cytoarchitecture of the hippocampal slice was resolved in a scan time of 1 h 12 min. The pyramidal cell layers (CA1 and CA3) and the granule cell layer (GCL) and the hillus (H) are resolved as confirmed by the immunohistochemical staining.
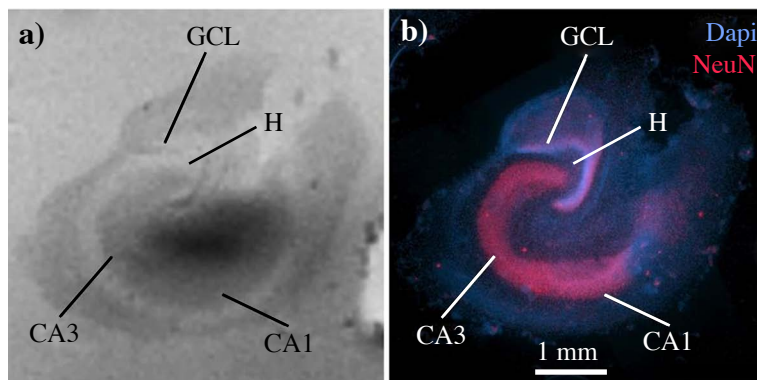
Fig. 5.2 non-RF-spoiled FLASH image of an acute hippocampal slice resolves histological details at high resolution and enables the identification of neuronal cell layers: granule cell layer (GCL) and pyramidal cell layers (CA1, CA3). The subsequent immunostaining of the same hippocampal slice confirms these results, since location and orientation of neuronal cell layers corresponds to the MR signals. MR image acquisition and data processing by Katharina Goebel. Tissue preparation/stainings and data interpretation by Johannes Gerlach.

5.3   MR microscopy using Lenz lenses

A significant part of this section on MR microscopy using Lens lenses was presented in [RK8][a] and will be submitted to the Journal of Magnetic Resonance Imaging as [RK1][b]. Histological staining of the whole brain slice by Johannes Gerlach, Experimental Epilsepy Lab, Department of Neurosurgery, University hospital Freiburg.

[a]Contributions: *RK:* Designed and manufacture of hardware, MR measurements, data evaluation, manuscript concept and writing; *OGG:* Data evaluation, concept and proofread the manuscript; *JGK:* Proofread the manuscript

[b]Contributions: *RK*: Process and hardware development and design, MR data acquisition, data processing, analysis and interpretation, manuscript concept and writing. *KGG:* MR data acquisition. *JG:* Tissue preparation, tissue stainings and data interpretation. *OGG:* Data interpretation, manuscript proofread. *JH:* MR methods development, manuscript proofread. *PL:* Data processing methods, proofread manuscript. *CH:* Data interpretation, proofread manuscript. *JGK:* Data interpretation, manuscript concept, proofread manuscript.

The Lenz lenses were run in two different settings. First in a Bruker 9.4 T horizontal bore small animal scanner equipped with a 72 mm diameter rat volume coil. For the second setting a Bruker 7 T horizontal bore small animal scanner with a 20 mm diameter quadrature cryoprobe for mice studies was used.

For this measurement, a fixed brain slice was used as tissue sample. The brain slice was prepared from an eight weeks old C57BL/6N and transgenic Thy1- eGFP mouse transcardially perfused for one minute with saline, and subsequently perfused with 4 % PFA in 0.1 mol phosphate buffer (PB) at pH 7.4. Then the brain was removed, post-fixed with 4 % PFA for 6 h at 4 °C and cut into 400 µm thick coronal sections with a vibratome VT 100S (*Leica Biosystems, Germany*).

The brain slice was placed on a Millicell® inlet, and the POM insert was filled with water to avoid tissue dehydration (and to simulate the *in vitro* culturing situation). The whole MR compatible platform was then assembled, and the Lenz lens was placed on top of the sample, by using alignment marks milled into the POM inlet (see fig. 5.3). As explained in chapter 3.5.6, if tilted, the Lenz lenses will only collect the magnetic flux that is pentrated by the field lines parallel to the B_1 field of the primary coil. Therefore, the Lenz lens axis should not be tilted towards the B1 field of the primary coil. The reference power and the reference gain were determined with a 1 mm thick coronal slice through the tissue sample and followed by localised shim to minimise signal distortion.

A T1 weighted FLASH sequence with the following parameters was used: TR = 200.0 ms, TE = 3.0 ms, flip angle = 30°, slice thickness = 0.5 mm, MTX = 200 x 200, FOV = 2 x 2 cm^2, resolution = 100 x 100 µm^2, NEX = 16 and scan time = 8 min 0 s. The raw images are shown in fig. 5.3. Image SNR was computed from exported DICOM raw data using ImageJ and the procedure described in chapter 2.2.2. In the setting described, an SNR of $SNR_i^{Ref} = 4.0$

was determined for the reference measurement using the 72 mm volume coil only. With a broad band Lenz lens, an $\mathrm{SNR}_i^{\mathrm{LL}} = 8.4$ was computed, which roughly doubles the image SNR. By using a resonant Lenz lens in this set up, SNR of was improved by approx. a factor of 10 to be $\mathrm{SNR}_i^{\mathrm{LLC}} = 34.4$.
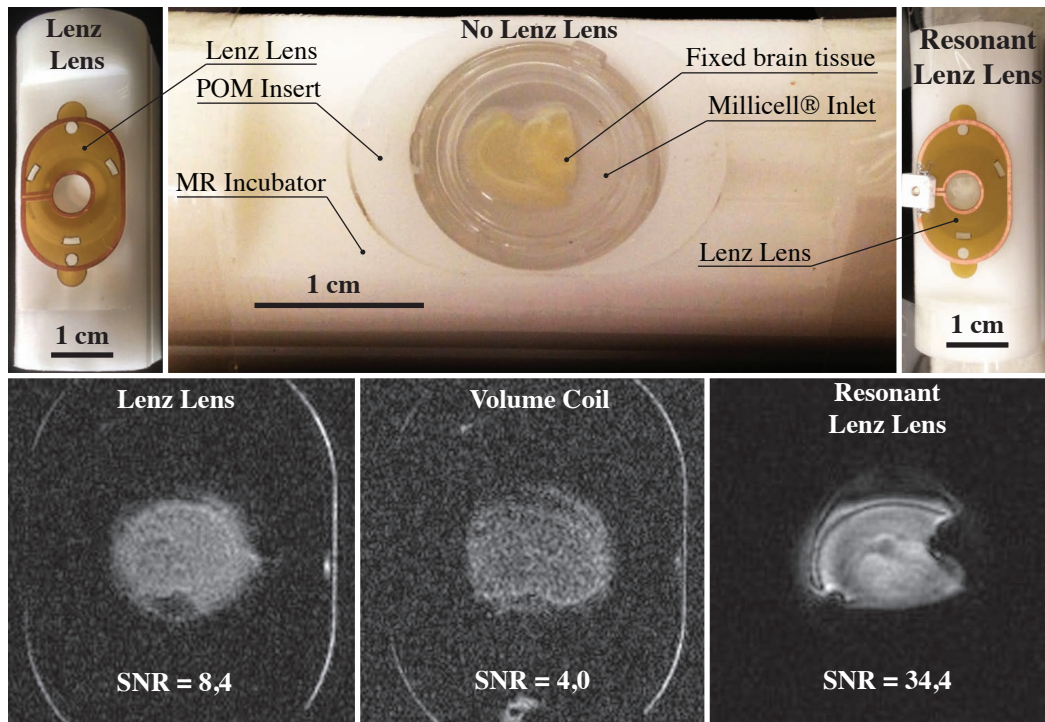

Fig. 5.3 A fixed half brain slice mounted in the MR incubator with the Lenz lens as signal amplifier. The signal to noise ratio increases significantly from a 72 mm diameter volume coil to a broadband Lenz lens and a resonant Lenz lens.

5.3.1   Lenz lens at 7 T with 20 mm quadrature cryoprobe

For this measurement, hippocampal slices were prepared from a mouse after postnatal day 4 (p4). The mouse was anaesthetised with isoflurane and decapitated. After dissection in ice-cold PB, the hippocampus was cut into 400 µm thick transverse sections. The hippocampal slices were cultivated for 21 days (3 weeks) on a Millicell® insert and then immersion-fixed in 4 % PFA at 4 °C for 12 h and rinsed in PB prior to the MR measurements.

Again, the whole MR compatible platform was assembled and used with a Lenz lens attached. The reference power and the reference gain were determined with 1 mm thick coronal slice through the tissue sample and followed by localised shim to minimise signal distortion. Since the 400 µm thick hippocampal slices were 21 days in vitro (DIV) they thinned down to a nominal thickness of approx. 100 µm. The neurons at the interfaces were injured when cutting the tissue into slices and thus uniformity of the hippocampal slice is compromised at the interface so the effective usable slice thickness is approx. 80 µm. If a 1D FLASH sequence, with an MR slice thicker than the physical hippocampal slice is applied the MR image is blurred due to the partial volume effect and image contrast drops dramatically. As can be seen from fig. 5.4 a), when using a 1D FLASH sequence, and in fig. 5.4 b) for a RARE sequence, with an MR slice thickness of 200 µm, although the hippocampal slice is clearly visible, no structures in the slice can be identified.

Therefore a 3D FLASH sequence (phase read-out in two directions) allowing for thinner coronal slices, was used. The 3D FLASH sequence used an effective coronal slice thickness of 75 µm with an in-plane resolution of 75×75 µm^2. Since in PFA fixed *ex vivo* tissue T2 and T1 time differ strongly from the *in vivo* and the *in vitro* case, the flip angle was adjusted for maximum signal (Ernst angle). If the flip angle is adjusted poorly, image contrast is at a minimum (see fig. 5.4 c)). Sweeping the flip angle at a constant TR = 29.3 ms and TE = 4.1 ms showed maximum signal at a flip angle of 10° as depicted in fig. 5.4 d)-f).

A 3D FLASH image with the following measurement parameters was recorded in 2 min 56 s scan time: TR = 29.3 ms, TE = 4.1 ms, flip angle = 10°, slice thickness = 75 µm, MTX = 200×200, FOV = 1.5×1.5 cm^2, resolution = 75×75 µm^2 and NEX = 2. A reference image without Lenz lens was recorded in the same time with the same parameters. As can be seen from fig. 5.4 h) & h), with an SNR of $SNR_i^{Ref} = 13.5$ and $SNR_i^{LL} = 14.7$, the reference measurement shows comparable performance to the Lenz lens measurement for this set-up.

In a 23 min 28 s scan, it is possible to identify cytoarchitectial key features of the hippocampal slice, such as CA1, CA3 and the granule cell layer (GCL).

	1D FLASH	RARE	Uncalibrated FA
Poor adjustments	a)	b)	c)
	$SNR_i = 35.2$, $CNR_i = 11.6$	$SNR_i = 12.3$, $CNR_i = 4.5$	$SNR_i = 8.8$, $CNR_i = 2.9$
	FA = 20° in 2min56s	FA = 15°, in 2min56s	FA = 10° in 2min56s
FA Calibration	d)	e)	f)
	$SNR_i = 10.6$, $CNR_i = 7.8$	$SNR_i = 14.5$, $CNR_i = 11.3$	$SNR_i = 21.1$, $CNR_i = 15.8$
	Reference in 2min56s	FA = 10° in 2min56s	FA = 10° in 23min28s
3D FLASH	g)	h)	i)
	$SNR_i = 13.5$, $CNR_i = 6.1$	$SNR_i = 14.7$, $CNR_i = 8.2$	$SNR_i = 37.2$, $CNR_i = 26.9$
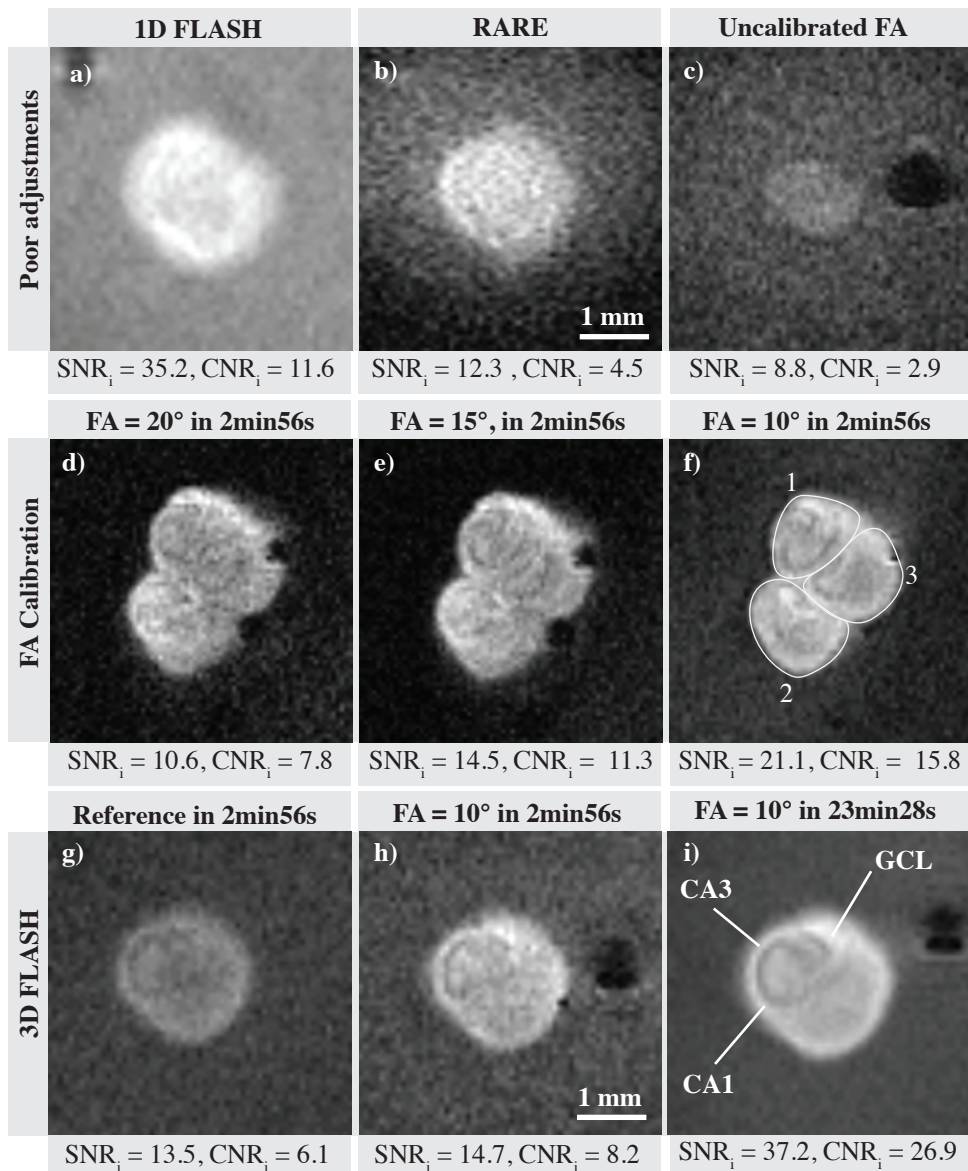
Fig. 5.4
Top row: The MR image quality suffers strongly when the MR slice thickness is thicker than the physical slice thickness of a hippocampal slice (partial volume effect), shown for a 1D FLASH and RARE sequence. Additionally, when the MR parameters are adjusted poorly (in this case the flip angle), almost no contrast is visible.
Middle row: A calibration of the flip angle towards the optimal angle (Ernst angle) improves image SNR and CNR tremendously (in this case 3 hippocampal slices are recorded in one shot).
Bottom row: Application of the Lenz lens increases SNR only slightly at 7 T with a cryoprobe coil. Still, the gross cytoarchitecture of a thin hippocampal slice ($< 100\,\mu m$) can be resolved in short scan times.

5.4   Intermediate conclusion neuroscientific results

In this chapter various methods and technologies were used to image fixed, acute and organotypic hippocampal slices cultures. First, fixed hippocampal sections and acute hippocampal slices were imaged to identify which hallmarks of the hippocampal cytoarchitecture are identifiable with FLASH, RARE and DTI sequences and confirmed via immunhistochemical stainings. Subsequently thinned out cultured brain slices were imaged, where the MR incubator and the Lenz lenses acted as key technologies.

From fixed hippocampal slices, high-resolution MR images were acquired over the whole physical slice within a scan time of 1 h 28 min for structural MR images and 3 h 31 min for diffusion tensor images. Similar imaging paradigms were published in other papers, but are either acquired from sub-samples of the hippocampus at higher resolution [47, 243] or in extensive scan times of up to 235 h [244]. However, all sequences explored for fixed tissue measurements are acquired from relatively thick (approx. 400 μm) tissue slices and from dead fixed tissue. The protocol used included rinsing the fixed tissue in phosphate buffer and imaging in saline solution as medium subsequently. During the course of this thesis, it became clear that there may be multiple issues with this approach. The fixative may induce artefacts [245], and T1 and T2 times differ significantly in fixed tissue [246–249] and so does the diffusion signal [250–252]. Thus the protocols for fixed tissue do not work well with the in vitro case. As the hippocampal slices were only rinsed, it is likely, that the fixative was not completely flushed from the tissue. This means, diffusion of the fixative may have happened even during MR image acquisition, thus changing the MR parameters while imaging. Therefore, it can be assumed that the parameters found for fixed tissue, although leading to beautiful results, are not optimum.

Since the scope of imaging hippocampal slices was to monitor disease progression, OHSC (cultured for three weeks) were subsequently imaged. As expected, the measurements protocols needed adaptation for optimum SNR in the in vitro case, thus the flip angle and TR/TE times were adjusted. Since the OHSC are far thinner than acute or fixed hippocampal slices (< 100 μm), a 3D sequence was used with very thin imaging slices to avoid the partial volume effect. The details that were identified with this method from the structural FLASH images, are not at the same level as with the fixed tissue measurements (as hallmarks, the cornu ammonis and the granule cell layer were still clearly visible). MR imaging of whole OHSC has been achieved with better image quality by Shepherd *et al*. [253]. In their publication, diffusion images of 14 DIV p9 Wistor rat OHSC were acquired at 78 μm^2 in plane resolution in 3.5 h and at 80 μm^2 in plane resolution in 25 min for FLASH images. However, they cut the OHSC from the culturing membrane and the culturing dish

for their measurement, and thus their method does not allow for further culturing of the same slice for longitudinal studies of disease progression, a core objective of this thesis.

6

Conclusions

This chapter concludes the thesis by review of the obtained results and their implication towards the scientific community. Potential future applications are discussed.

6.1 Review of the results

Within this thesis, three different types of MR probes were developed for magnetic resonance microscopy, the magnetic resonance force microscopy coils, the hollow micro coils and the Lenz lenses. An MR compatible incubation platform for longitudinal studies of brain tissue was developed and tested. These technologies were applied to MR microscopy of viable brain tissue.

In the introduction chapter 1, four hypotheses were posed.

1. Can we design and build magnetic resonance microscopy detectors with the potential of automated manufacturing and miniaturisation to close the gap between single cell experiments and studies on complex neuronal networks?

This hypothesis was addressed by the design, manufacturing and testing of three different MR detectors.

(i) The smallest wire bonded micro coils with a diameter down to $100\,\mu m$ SU-8 posts were manufactured. These up to $300\,\mu m$ high coils were designed and tested in a magnetic resonance force microscopy experiment, which is the highest resolution technique in magnetic resonance.

(ii) A novel manufacturing procedure for hollow micro coils manufactured by wire bonding around a dissolvable or removable post was developed. The embedded micro coils were manufactured with diameters of 1.5 mm and 1 mm respectively, where the fabrication procedure went through multiple iterations. The micro coils resulting from this process, show

slightly better performance than already published work by Ryan *et al.* [19], Sakellariou *et al.* [159] and Sillerud *et al.* [207]. The hollow micro coils have the advantage of being solenoidal and with no sidewall for an optimum filling factor (and therefore best possible MR sensitivity). These coils were designed for single cell and cell cluster experiments.

(iii) The Lenz lenses designed, built and tested are meant for magnetic resonance microscopy of more complex neuronal circuitry, namely hippocampal slice cultures. In principle, the wireless Lenz lenses are implantable coils. Due to their broad band capability, they allow multi-nuclear experiments, which is not easily possible with inductively coupled LC resonators. The Lenz lenses in this thesis cover a full hippocampal slice of a mouse (with approx. dimensions of $2 \times 3 \, mm^2$). The concept of Lenz lenses was explored and compared to inductively coupled LC resonators. While LC resonators are more efficient in MR signal magnification, the standard Lenz lenses posses broadband capability. Self-resonant Lenz lenses are found to be even better than r.f. resonators and are used in the further measurements of this thesis. These type of Lenz lenses were merged with the MR incubator to allow for the imaging of OHSC *in vitro*.

Although the built detector coils by themselves are capable of high resolution imaging, there is no single detector for single cell MR imaging *and* imaging of complex neuronal networks (namely hippocampal slices).

2. Can we build a platform to hyphenate brain slice culturing and magnetic resonance microscopy?

An MR compatible incubator was successfully designed and built. It can accommodate for the interface culturing method of OHSC, and its technical functionality has been qualified by temperature, gas and humidity measurements. Brain slices were used to evaluate tissue survival in the incubation platform which was confirmed by histological stainings of the samples. This platform offers the opportunity to culture brain tissue in a laboratory incubation chamber and transferring the tissue to the MR incubator seamlessly. Thus longitudinal measurements with MR microscopy methods are possible. The MR incubator was hyphenated with the Lenz lenses and two different MR scanners. However, a conclusive qualification apart from histological stainings still remains to be done. It would be opportune to use MR diffusion as a measure for tissue viability for this, as this would allow for continuous viability monitorin in the tissue over the whole MR measurement period.

3. Can we perform magnetic resonance microscopy on mouse brain slices with a small animal magnetic resonance imaging system?

For benchmarking, fixed hippocampal slices of healthy and epileptic mice were measured with FLASH and RARE imaging sequences and with diffusion weighted MR and

tractography. In the fixed tissue, it was possible to identify substructures of the hippocampal cytoarchitecture. The main cell layers of cornu ammonis and the granule cell layers were clearly visible and were used to identify even smaller features. The findings were confirmed by immunhistochemical stainings of the same slice. The method of virtual staining (tractography) gives additional insights into the connectivity of the hippocampus. A remaining issue with this approach is, that the MR parameters found for fixed tissue are not directly transferable to *in vitro* measurements.

4. Can we resolve specific sub-regions within brain slices *in vitro* that are associated with a significant brain disease and monitor its pathological progression using magnetic resonance microscopy methods?

The measurements on fixed hippocampal slices show that specific sub-regions can be identified. When compared to measurement of epileptic tissue and of tissue from the contralaterally injected side of a KA mouse, it became apparent, that even settled changes induced by epileptogenesis can be identified. Especially the only partly disappearing pyramidal cell layer CA1 was not visible in the epileptic slice, but was still visible in the contralateral slice.

The protocols developed for the fixed hippocampal slices were adapted to resolve the cytoarchitecture of thinned out *in vitro* hippocampal slice cultures. Therefore 3D FLASH imaging was used to avoid the partial volume effect. With the MR incubator and the Lenz lens it was possible to identify the gross anatomical details in these thinned OHSCs. The continuous translational monitoring of epilepsy disease progression, from status epilepticus to chronic epilepsy, has not yet been evaluated. However, the hardware developed during this thesis shows promise that these kind of measurements are now possible, and these translational studies of disease progression are planned measurement studies in the future.

6.2 Implications of the results and outlook

The technology and techniques of this thesis are developed for the manufacture of MR microscopy detectors for neuroscientific research, but as they gain further maturity might be useful in a broader context. The hollow micro coils described in chapter 3 are an excellent and high sensitivity tool for magnetic resonance microscopy of small samples (i.e. neuronal cells and cell clusters). The specific manufacturing method of wire bonding a solenoidal coil at high accuracy allows for micro coils with interwinding spacings, which is not easily achievable with other techniques. There are MR signal enhancement methods,

specifically dynamic nuclear polarisation (DNP), that require a microwave signal to be interspersed with the r.f. signal to transfer polarisation of electrons to MR active nuclei [174, 254]. DNP has the potential to increase MR signal significantly, especially in combination with magic angle spinning (MAS) [255]. However, a closely wound micro coil reflects an impinging microwave necessary for this technique, which is not the case for the hollow micro coils as manufactured in this thesis. In the optimum case, even the embedding material can be used, to focus the microwave into the sample (see fig. 6.1), thus priming the hollow micro coils of this thesis a promising tool for DNP and MAS.
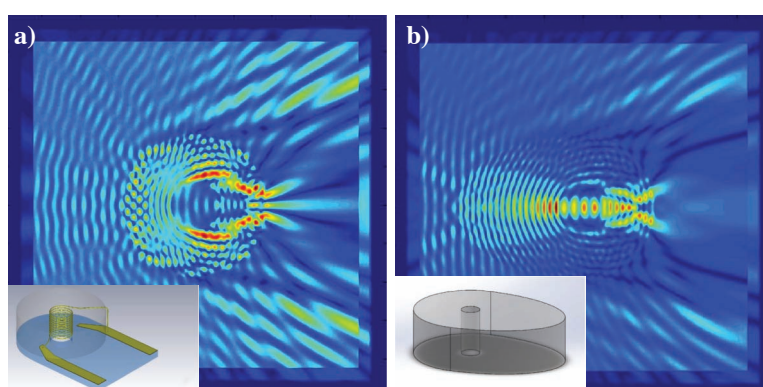

Fig. 6.1 COMSOL simulation of an impinging microwave at 500 GHz. While the current design (a) of the hollow micro coils embedding material reflects the microwave, a redesign (b) focuses the microwave into the sample area. These simulations were done by Suleman Shakil, Laboratory of Simulation, University of Freiburg.

For MR spectroscopy, miniaturisation is pushed further to gain in sensitivity. Magic angle spinning, to resolve J-coupling, has been pushed to spinning speeds of more than 100 kHz [256], and it has been suggested that spinning speeds of up to 250 kHz would be useful to achieve solution-state like spectra of protonated proteins. However, the current 100 kHz spinning rotors work with rotor diameters of 0.8 mm. Smaller samples (and therefore also detection coil diameters) are necessary for higher spinning speeds. The spinning speed is then mainly limited by the outer diameter of the rotor breaking the sound barrier and thus inducing a turbulence [257]. Therefore, smaller coil diameters (low wall thicknesses) are needed to achieve high filling factors and high spinning speeds. The concept of hollow solenoidal micro coils offers one possible solution to this challenge.

The MR incubator introduced in chapter 4, if proven reliable, may significantly contribute to fundamental research in magnetic resonance imaging, elucidation of disease progression and neurotechnology. Using the developed protocols and techniques, es-

pecially virtually staining OHSC with subsequent immunhistochemical staining of the tissue, will help to gradually close the gap between the MR microscopy signal (and its change) and the actual tissue microstructure. This connection is at this stage not yet fully understood and is of great interest to the MR community [85, 258].

Since OHSC are bloodless, functional MRI (fMRI) can not be done with the classical blood oxygen level dependant (BOLD) contrast. Still, as long as the OHSC are kept viable, dendritic swelling of the neurons is induced by synaptic activity. This denritic swelling can be visualised with high resolution MR microscopy allowing for fMRI of OHSC in the abscence of draining veins [259, 260]. While neuronal activity can be provoked chemical stimulation (inhibitory or exhibitory), the localisation of the fMRI signal is confined to the actual neurons in this case. For a more detailed stimulation of the OHSC, the presented technology could be hyphenated with optogenetic methods, to investigated more specific functions [137]. If the imaging resolution is sufficiently high, in an epileptic slice it may even be possible to directly detect dendritic currents [261]. The achievable spatial for these kinds of fMRI measurements for the quantification of neuronal activity via dendritic swelling across the hippocampal network still needs to be determined.

For the implantation of brain implants, the tissue response especially for electrically active surfaces, is of major interest [262, 263]. However, the investigation of the brain tissue response is usually evaluated *in vivo.* The presented platform offers the possibility to bring brain implants into contact with OHSC and close examination of the tissue response with MR microscopy methods, especially scarring and gliosis. This will offer high resolution quantification while decreasing the need for animal experiments.

For controlling chronic epileptic seizures, electrical stimulation of the brain tissue has been suggested (closed loop neuro stimulation). In trials with the first commercialised system (*NeuroPace Inc., USA*), in half of the patient symptoms were reduced, but no patient was actually seizure free [264]. The mechanism by which the electrical stimulation interrupts epileptic seizures is unknown. It is hypothesised that the electrical stimulation upregulates GABAergic hyperpolarisation which leads to a local inhibition of the neuronal activity. Hyphenation of the MR incubator with electrophysiological stimulation would offer a promising platform to monitor metabolic (i.e. GABAergic response) and structural changes originating from repeated electrophysiological stimulation at high resolution. The insights gained from these experiments will be transferable to the *in vivo* situation, thus handing guidlines for an optimal electrical stimulation for controlling epileptic seizures.

Appendices

A

Cryogenic cooling platform with active insulation

The Lenz lenses introduced in chapter 3 and used in chapter 5 increased the SNR significantly for larger volume coils, but this increase was not at the same level when used in the cryoprobe set-up. Apart from the smaller coil diameter of the cryoprobe, another reason for the low performance of the Lenz lens is the noise introduced by the non-cooled copper conductor. One possible solution to decrease the noise contribution of the Lenz lens, would be to cool the Lenz lens conductor to cryogenic temperatures. However, as with magnetic resonance microscopy, the MR probe needs to be close to the sample, cooling the probe to cryogenic temperatures requires active insulation to avoid sample freezing. Obviously not only Lenz lenses, but other micro coils, could benefit from cryo cooling. A first test of a modular platform actively insulating an inductively coupled surface coil from an area where a biological sample can be placed is shown in fig. A.1. The platform is milled from PTFE, a temperature stable polymer with minimum thermal expansion coefficient. The modular system consists of a sample layer (i.e. for a brain slice), an insulation layer through which a heated gas flow can be lead, a layer for aligning the surface coil (or a Lenz lens) sealed off with a fluid channel to be flooded with liquid nitrogen. Intial tests showed, that with active gas heating, the sample area stabilises at 16 °C while the surface coil is cooled by liquid nitrogen. Further development of this system may increase SNR significantly for either inductively coupled probes or wired probes, but miniaturisation needs to be dealt with.
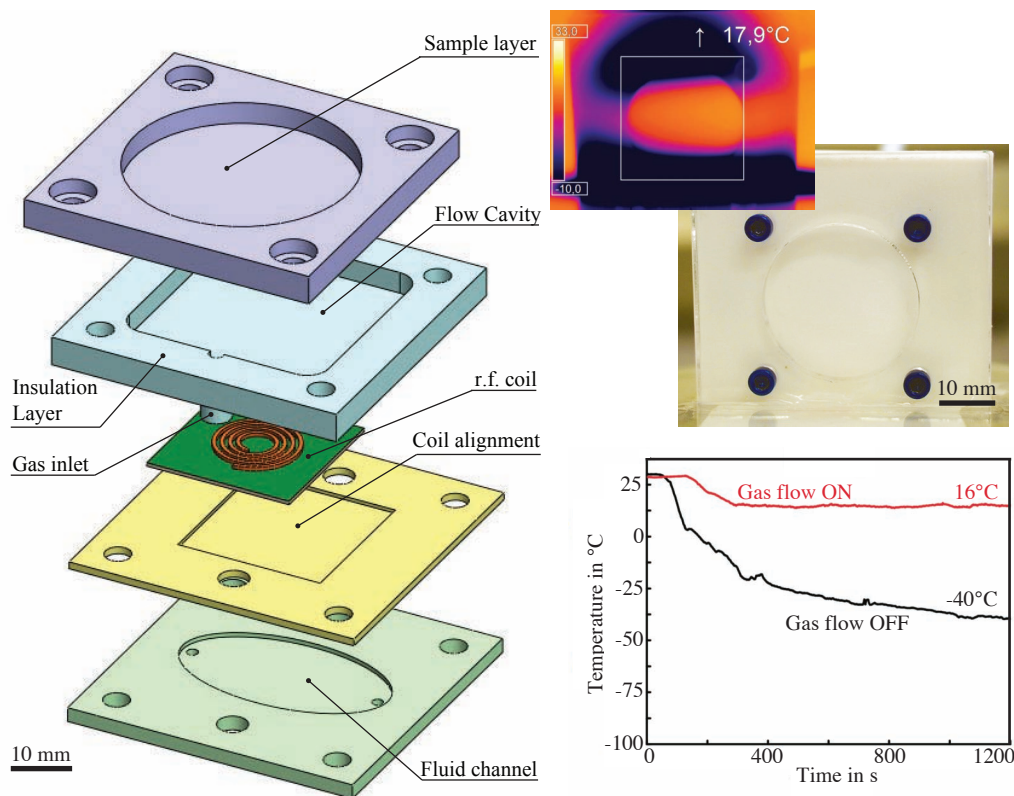
Fig. A.1 A modular platform for cryogenic cooling of an r.f. coil with active insulation. When the gas flow for active insulation is switched on, the temperature at the sample are stabilises at 16 °C. A significant part of this platform was developed in the master thesis of Agazi Tesfai [MA1].

B

Free-Standing micro coils

Chapter 3.4 describes a manufacturing procedure using dissolvable posts for hollow micro coils with high filling factors, whose windings are stabilised by an external polymer cast. Aside from susceptibility matching, this polymer cast protects the coil from mechanical vibration and deformation. But what if one wants to use the micro coil for its sensitivity towards mechanical vibration and deformation?

If, after wire bonding, the micro coils are not embedded into the protective polymer cast, but the dissovable posts are removed a solenoidal free standing micro coil or micro spring can be formed. Free standing micro coils were manufactured with two processes. (i) By wire bonding a coil around a post, which is dissolved afterwards (fig. B.1 a), b)). The second procedure (ii) was to wire bond the micro coils and subsequently detaching both wirebond. These micro coils were manually transferred onto a seperate substrate (coil transplantation, fig. B.1 c)).

Free standing micro coils with a diameter of 1 mm were manufactured by both, the dissolvable post process and coil transplantation. The coils show a mechanical resonance frequency at around 410 Hz. When a direct current through the micro coil is applied, due to the induced magnetic force in the electrical conductor, the stiffness of the spring decreases. This has been measured for four coils with a vibrometer and, as shown in fig. B.2, the mechanical resonance frequency drops from 410 Hz to below 380 Hz with the application of 400 mA. In principle it should also be possible, to excite a mechanical mode by the applying alternating current to the micro coil, which was not achieved yet.

The results of this section on free–standing micro coils were partly achieved in the Master's Thesis by Prateek Gogte [MA2].
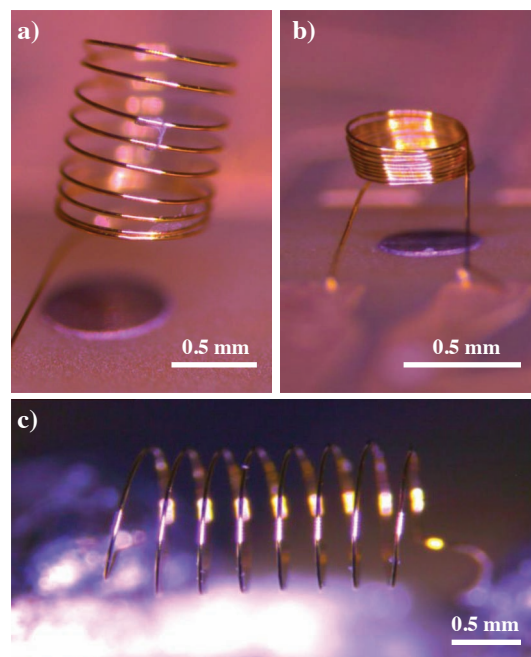
Fig. B.1 Two different free standing micro coils manufactured by wire bonding. Top: By dissolving the support post. Bottom: By coil transplantation.
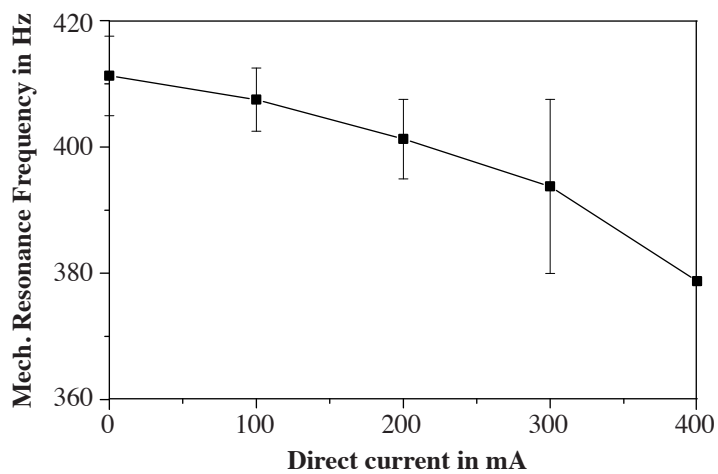

Fig. B.2 The mechanical resonance frequency of free standing micro coils drops with the application of direct current. This measurement was recorded with a vibrometer on 4 seperate free standing micro coils.

C

MRI, 3D printing and the human vocal tract

The method of 3D printing, as was used for the first implementation of the MR incubator described in chapter 4, was used for the reconstruction of MR images of the vocal tract. Therefore, human subjects (professional and amateur singers), were imaged in a 3 T clinical MRI scanner (*MAGNETOM Trio, Siemens Healthcare, Germany*), while holding a defined tone or phonation over the scan time of 13 s. Digital impressions of the subjects' teeth were generated from different methods (intraoral laser scan [265, 266], T1-weighted imaging with blueberry juice as contrast agent [267], T2-weighted RARE [268] and conventional dental impression).

After acquistion of the vocal tract and the teeth seperately, the MR data was fused with the teeth models. For the 3D printouts, a wall thickness of 2 mm assigned to the generated mesh file. The 3D prints were manufactured with a powder printer ZPrinter 450 (*3D Systems, USA*). In the 3D printout the cement-like powder is injected with binder solution from an inkjet printhead, resulting in a porous and fragile physical model. Thus, the 3D models were infiltrated with the super-glue like material Z-Bond 90 (*3D Systems, USA*). This method significantly improves mechanical strength and decreases gas permeability. The workflow for this procedure is depicted in fig. C.1

The 3D models were manufactured with the described procedure for different phonations, and their printouts are depicted in fig. C.2. The different teeth impression methods were fused with the 3D models to evaluate which teeth impression is the most accurate [RK6] and towards their influence on vocal formation [RK7].

This section on MRI and the vocal tract was partly published the two publications [RK6] and [RK7] and submitted as [RK4] with the main work done by Louisa Traser, Michael Echternach and Michael Burdurmy.
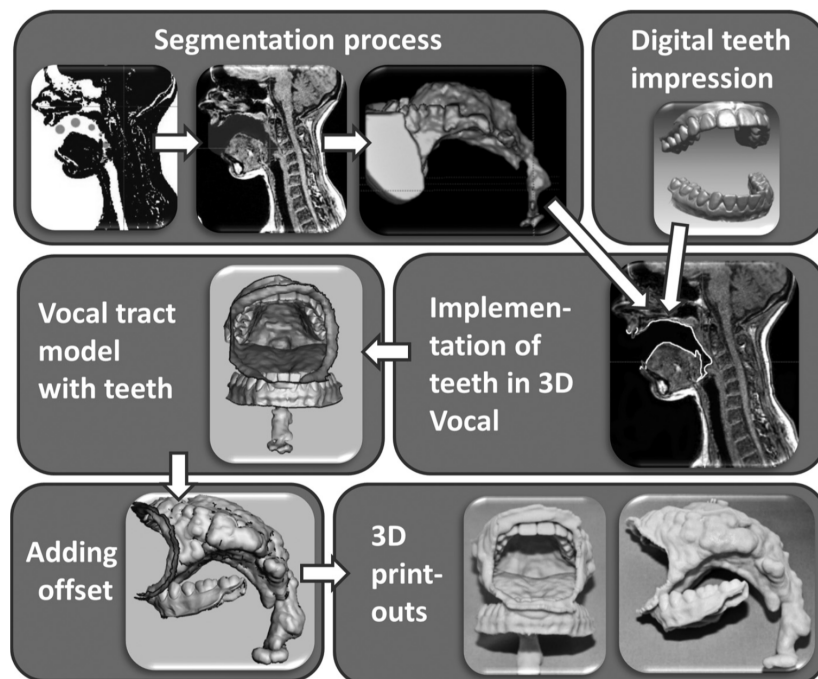
Fig. C.1 Workflow from MR image acquisition to 3D printout of a human vocal tract while phonation. Reprinted with permission from [269].

Fig. C.2 3D printouts of different phonations of the vocal tract acquired by MR imaging and printed with a powder printer.

D

Process parameters for photo resists

Table D.1 Lithography parameters using a 100 mm diameter Pyrex wafer with a 20 nm Cr, and a 150 nm Au layer. The AZ 40XT (*MicroChemicals GmbH, Germany*) was used as positive photoresist. A resist height of 20 μm was aimed for. The wafers were cleaned using a standard acetone, iso-propanol and DI-water rinse.

Step	Parameters	Comment
Prebake	15 min at 150 °C	hotplate contact
Spin Coating	10 s at 500 rpm 30 s at 3000 rpm	4 ml of AZ 40XT
Edge Bead Removal (EBR)	60 s at 0 rpm 15 s at 500 rpm 10 s at 1000 rpm	resist settling time syringe based EBR drying
Softbake	2 min at 125 °C 5 min at 125 °C 2 min at 125 °C	2 cm above hotplate hotplate contact 2 cm above hotplate
Exposure	120 s at 4.9 mW	no i-line filter
Post Exposure Bake (PEB)	100 s at 105 °C 2 min cool off	hotplate contact 2 cm above hotplate
Developer	7 min in petri-dish	AZ 726 MIF

Table D.2 Process parameters for SU-8 3005 adhesion layer with approx. 8 µm thickness.

Step	Parameters	Comment
Prebake	10 min at 120 °C	Hotplate
Plasma Clean	2 min at 600 W	O2 Plasma
Adhesion Promoter	HMDS at 100 °C	Vacuum hotplate
Spincoat	10 s at 500 rpm 30 s at 3000 rpm	4 ml SU-8 3005
Softbake	3 min at 95 °C	Hotplate
Exposure	200 mJ cm^{-2}, 100 s	i-line filter
Post Exposure Bake	1 min at 65 °C 2 min at 95 °C	Hotplate
Develop	5 min	

Table D.3 Process parameters for SU-8 2150 post layer with approx. 200 µm thickness.

Step	Parameters	Comment
Prebake	10 min at 95 °C	Hotplate
Plasma Clean	2 min at 600 W	O2 Plasma
Constant Injection	Hotplate at 60 °C	SU-8 2150
Softbake	7 min at 65 °C 8 h at 95 °C	Temperature ramp from 65 °C at 1 °C min^{-1}
Exposure	600 mJ cm^{-2}, 250 s	i-line filter
Post Exposure Bake	7 min at 65 °C 2 h at 95 °C	Temperature ramp from 65 °C at 1 °C min^{-1}
Develop	45 min 5 min 5 min	20 % Ultrasound bath fresh developer Isopropanol

E

CNC milling parameters

Table E.1 Milling for PMMA

Type	Diameter in mm	Flutes Number	Spindle in rpm	Feedrate in mm/min
flat end mill	0.5	1	15000	300
flat end mill	1	3	10000	300
flat end mill	1.5	1	12000	300
flat end mill	2	1	11000	300
flat end mill	3	1	10000	425
drill	0.55	2	5000	0
drill	3	2	5000	0

Table E.2 Milling parameters for PCBs

Type	Diameter in mm	Flutes Number	Spindle in rpm	Feedrate in mm/min
flat end mill	1	2	24000	288
flat end mill	1.5	2	24000	300
flat end mill	2	3	24000	576
drill	1	2	24000	0
drill	1.5	2	24000	0

Table E.3 Milling parameters for Aluminium

Type	Diameter in mm	Flutes Number	Spindle in rpm	Feedrate in mm/min
flat end mill	0.3	2	24000	48
flat end mill	0.5	2	24000	96
flat end mill	1	3	24000	288
flat end mill	1.5	3	23979	4316
flat end mill	2	3	23999	5759
flat end mill	4	4	17427	418
flat end mill	5	4	13942	3903
drill	0.5	2	24000	0
drill	0.75	2	24000	0
drill	1	2	24000	0
drill	1.5	2	24000	0
drill	2	2	24000	0
drill	2.5	2	22918	0
drill	3	2	19098	0
drill	4	2	14323	0
drill	5	2	11459	0

Table E.4 Milling parameters for POM

Type	Diameter in mm	Flutes Number	Spindle in rpm	Feedrate in mm/min
flat end mill	0.3	2	24000	720
flat end mill	0.5	2	24000	960
flat end mill	1	3	24000	2880
flat end mill	1.5	3	21220	3819
flat end mill	2	2	15915	2546
flat end mill	3	2	10610	2546
flat end mill	4	3	7957	3819
flat end mill	5	3	6366	3819
drill	0.5	2	24000	0
drill	0.75	2	24000	0
drill	1	2	24000	0
drill	1.5	2	21220	0
drill	2	2	15915	0
drill	2.5	2	12732	0
drill	3	2	10610	0
drill	4	2	7957	0
drill	5	2	6366	0

Layout of the MRFM chips.
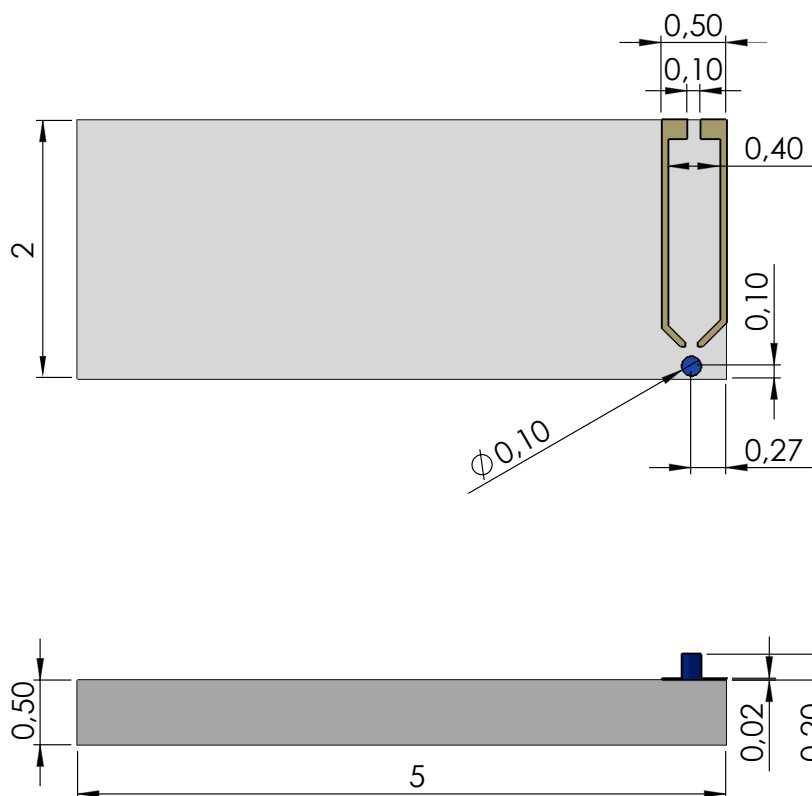

Fig. F.1 Layout of the MRFM Chips. All values are given in mm.
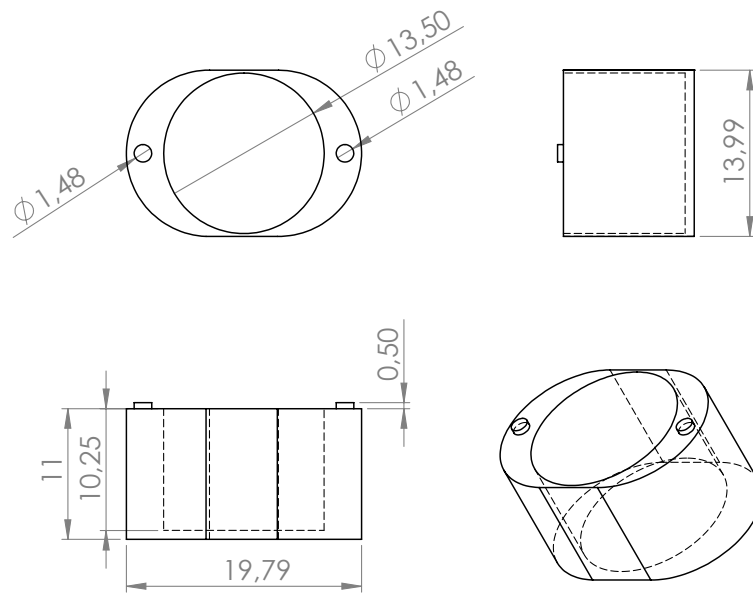
Fig. G.1 Technical Drawing of the POM insert used in the MR incubator. All values are given in mm.
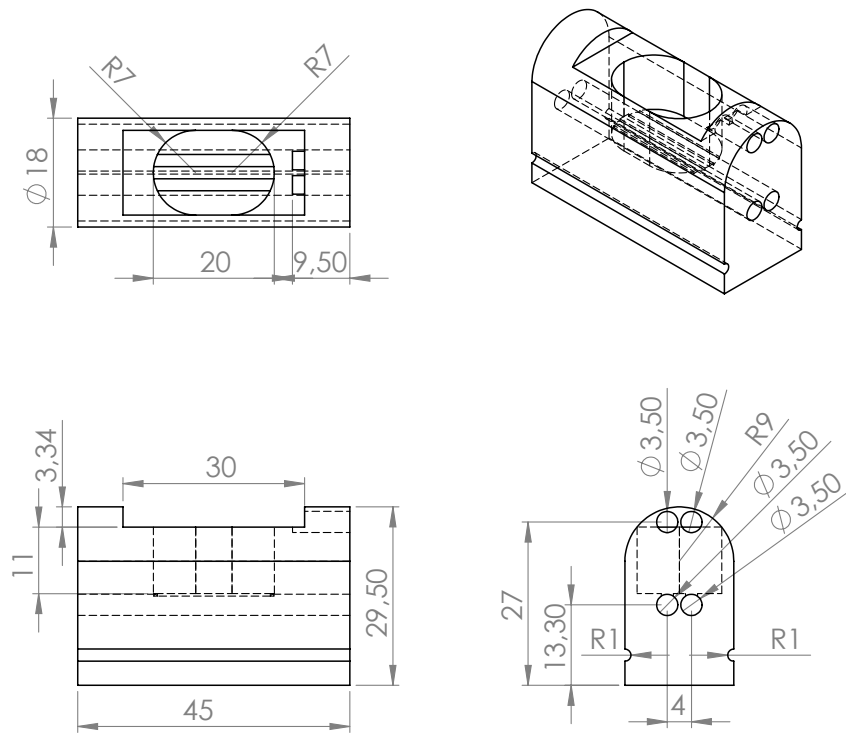
Fig. H.1 Technical Drawing of the MR compatible incubation platform. All values are given in mm.

I

MRI Parameters Overview

Table I.1 MR imaging parameters used for FLASH, RARE and tractography of fixed hippocampal slice sections.

Parameter	Fixed tissue			Acute	Lenz lens	
	FLASH	RARE	DTI	FLASH	FLASH at 9.4 T	3D FLASH at 7 T
TR	300.0 ms	2000 ms	3000 ms	300.0 ms	200 ms	29.3 ms
TE	16 ms	51 ms	39 ms	13.3 ms	3 ms	4.1 ms
Flip angle	50°	–	–	50°	30°	10°
RARE factor	–	6	–	–	–	–
Slice thickness	100 µm	100 µm	100 µm	150 µm	500 µm	75 µm
MTX	650 × 550	512 × 480	320 × 190	450 × 450	200 × 200	200 × 200
Resolution	20 × 20 µm²	20 × 24 µm²	39 × 39 µm²	33 × 33 µm²	100 × 100 µm²	75 × 75 µm²
NEX	32	32	16	32	16	2
b-value	–	–	1000 s mm^{-1}	–	–	–
# b=0 images	–	–	6	–	–	–
Segments	–	–	4	–	–	–
Directions	–	–	60	–	–	–
Scan time	1 h 28 min	1 h 25 min	3 h 31 min	1 h 12 min	8 min 0 s	23 min 28 s

References

[1]   K G Yiannopoulou and S G Papageorgiou. "Current and future treatments for Alzheimer's disease". In: *Therapeutic Advances in Neurological Disorders* 6.1 (Dec. 2012), pp. 19–33.

[2]   Pascal Vrielynck. "Current and emerging treatments for absence seizures in young patients". In: *Neuropsychiatric Disease and Treatment* 9 (July 2013), pp. 963–975.

[3]   A H V Schapira. "Present and future drug treatment for Parkinson's disease". In: *Journal of Neurology, Neurosurgery & Psychiatry* 76.11 (Nov. 2005), pp. 1472–1478.

[4]   Jérôme Yelnik et al. "Localization of stimulating electrodes in patients with Parkinson disease by using a three-dimensional atlas—magnetic resonance imaging coregistration method". In: *J Neurosurg* 99 (2003), pp. 89–99.

[5]   Michael S Okun. "Deep-Brain Stimulation for Parkinson's Disease". In: *New England Journal of Medicine* 367.16 (Oct. 2012), pp. 1529–1538.

[6]   H S Mayberg et al. "Deep Brain Stimulation for Treatment-Resistant Depression". In: *Neuron* 45 (2005), pp. 651–660.

[7]   Luc Mallet et al. "Subthalamic Nucleus Stimulation in Severe Obsessive–Compulsive Disorder". In: *New England Journal of Medicine* 359.20 (Nov. 2008), pp. 2121–2134.

[8]   F Rosenow and Hans Lüders. "Presurgical evaluation of epilepsy". In: *Brain* 124.9 (Sept. 2001), pp. 1683–1700.

[9]   M Gierthmuehlen et al. "Mapping of sheep sensory cortex with a novel microelectrocorticography grid". In: *Journal of Comparative Neurology* 522 (2014), pp. 3590–3608.

[10]   P Vemuri and C R Jack Jr. "Role of structural MRI in Alzheimer's disease". In: *Alzheimer's research & therapy* 2.23 (2010), pp. 1–10.

[11]   I Hickie et al. "Reduced hippocampal volumes and memory loss in patients with early- and late-onset depression". In: *The British Journal of Psychiatry* 186.3 (Mar. 2005), pp. 197–202.

[12]   D P Soares and M Law. "Magnetic resonance spectroscopy of the brain: review of metabolites and clinical applications". In: *Clinical radiology* (2009).

[13]   Giovanni B Frisoni et al. "The clinical use of structural MRI in Alzheimer disease". In: *Nature Reviews Neurology* 6.2 (Feb. 2010), pp. 67–77.

[14]   Samuel F Berkovic et al. "Hippocampal sclerosis in temporal lobe epilepsy demonstrated by magnetic resonance imaging". In: *Annals of Neurology* 29.2 (Feb. 1991), pp. 175–182.

[15]   I Hickie et al. "Subcortical hyperintensities on magnetic resonance imaging in patients with severe depression—A longitudinal evaluation". In: *Biological psychiatry* 42 (1997), pp. 367–374.

[16] Vlad Badilita et al. "On-chip three dimensional microcoils for MRI at the microscale". In: *Lab on a Chip* 10.11 (2010), pp. 1387–1390.

[17] M Mohmmadzadeh et al. "Characterization of a 3D MEMS fabricated micro-solenoid at 9.4T". In: *Journal of Magnetic Resonance* 208.1 (Jan. 2011), pp. 20–26.

[18] Oliver G Gruschke et al. "Lab on a chip phased-array MR multi-platform analysis system". In: *Lab on a Chip* 12.3 (2012), pp. 495–502.

[19] Herbert Ryan et al. "Contactless NMR Spectroscopy on a Chip". In: *Analytical Chemistry* 84.8 (Apr. 2012), pp. 3696–3702.

[20] A G Webb. "Radiofrequency microcoils for magnetic resonance imaging and spectroscopy". In: *Journal of Magnetic Resonance* 229 (Apr. 2013), pp. 55–66.

[21] N Spengler et al. "Micro-fabricated Helmholtz coil featuring disposable microfluidic sample inserts for applications in nuclear magnetic resonance". In: *Journal of Micromechanics and Microengineering* 24 (2014), p. 034004.

[22] Vlad Badilita et al. "Microscale nuclear magnetic resonance: a tool for soft matter research". In: *Soft Matter* 8.41 (2012), p. 10583.

[23] R C Meier et al. "Microfluidic integration of wirebonded microcoils for on-chip applications in nuclear magnetic resonance". In: *Journal of Micromechanics and Microengineering* 24 (2014), p. 045021.

[24] M Jouda, O G Gruschke, and J G Korvink. "Implementation of an in-field CMOS frequency division multiplexer for 9.4T magnetic resonance applications". In: *International Journal of Circuit Theory and Applications* (2014).

[25] Markus Weiger et al. "NMR microscopy with isotropic resolution of 3.0 μm using dedicated hardware and optimized methods". In: *Concepts in Magnetic Resonance Part B: Magnetic Resonance Engineering* 33B.2 (2008), pp. 84–93.

[26] S C Lee et al. "One Micrometer Resolution NMR Microscopy". In: *Journal of Magnetic Resonance* 150 (2001), pp. 207–213.

[27] K V Nguyen et al. "DLA based compressed sensing for high resolution MR microscopy of neuronal tissue". In: *Journal of Magnetic Resonance* 259 (2015), pp. 186–191.

[28] Irina Kharatishvili et al. "MRI changes and complement activation correlate with epileptogenicity in a mouse model of temporal lobe epilepsy". In: *Brain Structure and Function* 219.2 (Mar. 2013), pp. 683–706.

[29] A Sierra, O Gröhn, and A Pitkänen. "Imaging microstructural damage and plasticity in the hippocampus during epileptogenesis". In: *Neuroscience* 309 (2015), pp. 162–172.

[30] Sandy R Shultz et al. "Neuroimaging the Epileptogenic Process". In: *Neurotherapeutics* (Feb. 2014), pp. 1–11.

[31] Riikka Immonen et al. "MRI Biomarkers for Post-Traumatic Epileptogenesis". In: *Journal of Neurotrauma* 30.14 (July 2013), pp. 1305–1309.

[32] G A Johnson et al. "A multidimensional magnetic resonance histology atlas of the Wistar rat brain". In: *NeuroImage* 62 (2012), pp. 1848–1856.

[33] Evan Calabrese et al. "A quantitative magnetic resonance histology atlas of postnatal rat brain development with regional estimates of growth and variability". In: *NeuroImage* 71 (May 2013), pp. 196–206.

[34] Timothy M Shepherd et al. "Aldehyde fixative solutions alter the water relaxation and diffusion properties of nervous tissue". In: *Magnetic Resonance in Medicine* 62.1 (July 2009), pp. 26–34.

[35] S C Grant et al. "MR Microscopy of Multicomponent Diffusion in Single Neurons". In: *Magnetic Resonance in Medicine* (2001), pp. 1107–1112.

[36] S C Grant et al. "NMR Spectroscopy of Single Neurons". In: *Magnetic Resonance in Medicine* 44 (2000), pp. 19–22.

[37] J S Schoeniger et al. "Relaxation-Time and Diffusion NMR Microscopy of Single Neurons". In: *Journal of Magnetic Resonance* 103 (1994), pp. 261–273.

[38] Luisa Ciobanu, Andrew G Webb, and Charles H Pennington. "Magnetic resonance imaging of biological cells". In: *Progress in Nuclear Magnetic Resonance Spectroscopy* 42.3-4 (Aug. 2003), pp. 69–93.

[39] G Radecki et al. "Functional magnetic resonance microscopy at single-cell resolution in Aplysia californica". In: *Proceedings of the National Academy of Sciences*. 2014, pp. 8667–8672.

[40] B Gähwiler. "Organotypic slice cultures: a technique has come of age". In: *Trends in Neurosciences* 20.10 (Oct. 1997), pp. 471–477.

[41] Ryuta Koyama. "The use of organotypic slice cultures for the study of epileptogenesis". In: *Neuropathology* (Feb. 2013).

[42] C Humpel. "Organotypic brain slice cultures: A review". In: *Neuroscience* 305 (2015), pp. 86–98.

[43] S J Blackband et al. "MR Microscopy pf Perfused Brain Slices". In: *Magnetic Resonance in Medicine* 38 (1997), pp. 1–4.

[44] Timothy M Shepherd, Stephen J Blackband, and Edward D Wirth. "Simultaneous diffusion MRI measurements from multiple perfused rat hippocampal slices". In: *Magnetic Resonance in Medicine* 48.3 (Aug. 2002), pp. 565–569.

[45] Jeremy Flint et al. "Diffusion weighted magnetic resonance imaging of neuronal activity in the hippocampal slice model". In: *NeuroImage* 46.2 (June 2009), pp. 411–418.

[46] Jeremy J Flint et al. "Magnetic resonance microscopy of mammalian neurons". In: *NeuroImage* 46.4 (July 2009), pp. 1037–1040.

[47] Jeremy J Flint et al. "Cellular-level diffusion tensor microscopy and fiber tracking in mammalian nervous tissue with direct histological correlation". In: *NeuroImage* 52.2 (Aug. 2010), pp. 556–561.

[48] Lars Sundstrom et al. "Organotypic cultures as tools for functional screening in the CNS". In: *Drug Discovery Today* 10.14 (July 2005), pp. 993–1000.

[49] Yu Huang, Justin C Williams, and Stephen M Johnson. "Brain slice on a chip: opportunities and challenges of applying microfluidic technology to intact tissues". In: *Lab on a Chip* 12.12 (2012), pp. 2103–2117.

[50] Klaus Albus, Uwe Heinemann, and Richard Kovács. "Network activity in hippocampal slice cultures revealed by long-term in vitro recordings". In: *Journal of Neuroscience Methods* 217.1-2 (July 2013), pp. 1–8.

[51] Yossi Buskila et al. "Extending the viability of acute brain slices". In: *Scientific Reports* 4 (June 2014).

[52] David M Dorris et al. "An aerator for brain slice experiments in individual cell culture plate wells". In: *Journal of Neuroscience Methods* 238 (Dec. 2014), pp. 1–10.

[53] Adina Scott et al. "A microfluidic microelectrode array for simultaneous electrophysiology, chemical stimulation, and imaging of brain slices". In: *Lab on a Chip* 13.4 (2013), pp. 527–535.

[54] Siavash Ahrar et al. "Optical stimulation and imaging of functional brain circuitry in a segmented laminar flow chamber". In: *Lab on a Chip* 13.4 (2013), pp. 536–541.

[55] Shadi F Othman et al. "The e-Incubator: A Magnetic Resonance Imaging-Compatible Mini Incubator". In: *Tissue Engineering Part C: Methods* 21.4 (Apr. 2015), pp. 347–355.

[56] Vahid Khalilzad-Sharghi and Huihui Xu. "Design and Fabrication of an MRI-Compatible, Autonomous Incubation System". In: *Annals of Biomedical Engineering* (Mar. 2015).

[57] E Petersen, K Potter, and J Butler. "Bioreactor and probe system for magnetic resonance microimaging and spectroscopy of chondrocytes and neocartilage". In: *International Journal of Imaging Systems and Technology* 8 (1997), pp. 285–292.

[58] Satoshi Kubo et al. "A Gel-Encapsulated Bioreactor System for NMR Studies of Protein-Protein Interactions in Living Mammalian Cells". In: *Angewandte Chemie International Edition* 52.4 (Nov. 2012), pp. 1208–1211.

[59] Vicent Esteve et al. "Development of a three-dimensional cell culture system based on microfluidics for nuclear magnetic resonance and optical monitoring". In: *Biomicrofluidics* 8.6 (Nov. 2014), p. 064105.

[60] Ayten Kalfe et al. "Looking into Living Cell Systems: Planar Waveguide Microfluidic NMR Detector for in VitroMetabolomics of Tumor Spheroids". In: *Analytical Chemistry* 87.14 (July 2015), pp. 7402–7410.

[61] Kayvan R Keshari et al. "Hyperpolarized 13C spectroscopy and an NMR-compatible bioreactor system for the investigation of real-time cellular metabolism". In: *Magnetic Resonance in Medicine* 63.2 (Feb. 2010), pp. 322–329.

[62] S Richardson, B Siow, and E Panagiotaki. "Viable and fixed white matter: Diffusion magnetic resonance comparisons and contrasts at physiological temperature - Richardson - 2013 - Magnetic Resonance in Medicine - Wiley Online Library". In: *Magnetic Resonance in Medicine* 72 (2013), pp. 1151–1161.

[63] S Richardson et al. "A viable isolated tissue system: A tool for detailed MR measurements and controlled perturbation in physiologically stable tissue". In: *Magnetic Resonance in Medicine* 69.6 (July 2012), pp. 1603–1610.

[64] A Ward et al. "PLOS ONE: Noninvasive Metabolic Imaging of Engineered 3D Human Adipose Tissue in a Perfusion Bioreactor". In: *PLOS ONE* (2013).

[65] R Bai et al. "Simultaneous calcium fluorescence imaging and MR of ex vivo organotypic cortical cultures: a new test bed for functional MRI". In: *NMR in Biomedicine* 28 (2015), pp. 1726–1738.

[66] R Bai et al. "Assessing the sensitivity of diffusion MRI to detect neuronal activity directly". In: *Proceedings of the National Academy of Sciences*. 2016, pp. 1728–1737.

[67] Jeremy J Flint et al. "A Microperfusion and In-Bore Oxygenator System Designed for Magnetic Resonance Microscopy Studies on Living Tissue Explants". In: *Scientific Reports* 5 (Dec. 2015), p. 18095.

[68] Choong H Lee et al. "Investigation of the subcellular architecture of L7 neurons of Aplysia californica using magnetic resonance microscopy (MRM) at 7.8 microns". In: *Scientific Reports* 5 (2015).

[69] Vincent Malba et al. "Laser-Lathe Lithography—a Novel Method for Manufacturing Nuclear Magnetic Resonance Microcoils". In: *Biomedical Microdevices* 5.1 (2003), pp. 21–27.

[70] Malcolm H Levitt. *Spin Dynamics Basics of Nuclear Magnetic Resonance.* John Wiley & Sons, Feb. 2008.

[71] Andrew Webb. "Increasing the Sensitivity of Magnetic Resonance Spectroscopy and Imaging". In: *Analytical Chemistry* 84.1 (Jan. 2012), pp. 9–16.

[72] R Kamberger. "Masters Thesis: Inductively Coupled Micro Nuclear Magnetic Resonance Detectors". PhD thesis. Albert-Ludwigs-Universität Freiburg, 2012.

[73] Charles P Slichter. *Principles of Magnetic Resonance.* Springer Science & Business Media, 1990.

[74] D I Hoult and N S Ginsberg. "The Quantum Origins of the Free Induction Decay Signal and Spin Noise". In: *Journal of Magnetic Resonance* 148.1 (Jan. 2001), pp. 182–199.

[75] Govind B Chavhan et al. "Principles, Techniques, and Applications of T2*-based MR Imaging and Its Special Applications1". In: *RadioGraphics* 29.5 (Sept. 2009), pp. 1433–1449.

[76] P C Lauterbur. "Image Formation by Induced Local Interactions: Examples Employing Nuclear Magnetic Resonance". In: *Nature* 242.5394 (Mar. 1973), pp. 190–191.

[77] P Mansfield and P K Grannell. "NMR 'diffraction' in solids?" In: *Journal of Physics C: Solid State Physics* 6.22 (1973), p. L422.

[78] Anil Kumar, Dieter Welti, and Richard R Ernst. "NMR Fourier zeugmatography". In: *Journal of Magnetic Resonance (1969)* 18.1 (Apr. 1975), pp. 69–83.

[79] T Geva. "Magnetic Resonance Imaging: Historical Perspective - Journal of Cardiovascular Magnetic Resonance". In: *Journal of Cardiovascular Magnetic Resonance* 8.4 (2006), pp. 573–580.

[80]   Richard Bitar et al. "MR Pulse Sequences: What Every Radiologist Wants to Know but Is Afraid to Ask1". In: *RadioGraphics* 26.2 (Mar. 2006), pp. 513–537.

[81]   J Hennig, A Nauerth, and H Friedburg. "RARE imaging: A fast imaging method for clinical MR - Hennig". In: *Magnetic Resonance in Medicine* 3 (1986), pp. 823–833.

[82]   A Haase et al. "FLASH imaging: Rapid NMR imaging using low flip-angle pulses". In: *Journal of Magnetic Resonance* 67 (1986), pp. 258–266.

[83]   S Mori and J Zhang. "Principles of Diffusion Tensor Imaging and Its Applications to Basic Neuroscience Research". In: *Neuron* 51 (2006), pp. 527–539.

[84]   W Van Hecke, L Emsell, and S Sunaert. *Diffusion Tensor Imaging: A Practical Handbook*. Springer Science & Business Media. 2016.

[85]   Nikolaus Weiskopf et al. "Advances in MRI-based computational neuroanatomy: from morphometry to in-vivo histology". In: *Current Opinion in Neurology* 28.4 (Aug. 2015), pp. 313–322.

[86]   R Bammer. "Basic principles of diffusion-weighted imaging". In: *European journal of radiology* 45 (2003), pp. 169–184.

[87]   P J Basser, J Mattiello, and D LeBihan. "MR diffusion tensor spectroscopy and imaging." In: *Biophysical journal* 66 (1994), pp. 259–267.

[88]   P W Kuchel, K Nagashima, and S Velan. "Stejskal–tanner equation derived in full". In: *Concepts in Magnetic Resonance Part A* 40.5 (2012), pp. 205–214.

[89]   Nikolaus Weiskopf et al. "Quantitative multi-parameter mapping of R1, PD*, MT, and R2* at 3T: a multi-center validation". In: *Frontiers in Neuroscience* 7.95 (2013), pp. 1–11.

[90]   D Le Bihan and H Johansen-Berg. "Diffusion MRI at 25: Exploring brain tissue structure and function". In: *NeuroImage* 61 (2012), pp. 324–341.

[91]   Denis S Grebenkov. "Use, misuse, and abuse of apparent diffusion coefficients". In: *Concepts in Magnetic Resonance Part B: Magnetic Resonance Engineering* 36A.1 (Jan. 2010), pp. 24–35.

[92]   Peter B Kingsley. "Introduction to diffusion tensor imaging mathematics: Part I. Tensors, rotations, and eigenvectors". In: *Concepts in Magnetic Resonance Part B: Magnetic Resonance Engineering* 28A.2 (2006), pp. 101–122.

[93]   B Stieltjes et al. "Diffusion Tensor Imaging and Axonal Tracking in the Human Brainstem". In: *NeuroImage* 14 (2001), pp. 723–735.

[94]   M Catani et al. "Virtual in Vivo Interactive Dissection of White Matter Fasciculi in the Human Brain". In: *NeuroImage* 17 (2002), pp. 77–94.

[95]   Peter B Kingsley. "Introduction to diffusion tensor imaging mathematics: Part II. Anisotropy, diffusion-weighting factors, and gradient encoding schemes". In: *Concepts in Magnetic Resonance Part B: Magnetic Resonance Engineering* 28A.2 (2006), pp. 123–154.

[96]   P B Kingsley. "Introduction to diffusion tensor imaging mathematics: Part III. Tensor calculation, noise, simulations, and optimization - Kingsley - 2006 - Concepts in Magnetic Resonance Part A - Wiley Online Library". In: *Concepts in Magnetic Resonance Part A* (2006).

[97]   E Plenge, DHJ Poot, and M Bernsen. "Super-resolution methods in MRI: Can they improve the trade-off between resolution, signal-to-noise ratio, and acquisition time?" In: *Magnetic Resonance in Medicine* 68 (2012), pp. 1983–1993.

[98]   C Thomas et al. "Anatomical accuracy of brain connections derived from diffusion MRI tractography is inherently limited". In: *Proceedings of the National Academy of Sciences*. 2014, pp. 16574–16579.

[99]   James B Aguayo et al. "Nuclear magnetic resonance imaging of a single cell". In: *Nature* 322.6075 (July 1986), pp. 190–191.

[100]   P Selenko and G Wagner. "Looking into live cells with in-cell NMR spectroscopy". In: *Journal of structural biology* (2007).

[101]   P J M van Bentum, J W G Janssen, and A P M Kentgens. "Towards nuclear magnetic resonance -spectroscopy and -imaging". In: *The Analyst* 129.9 (2004), p. 793.

[102] Ray Freeman. "Pioneers of High-ResolutionNMR". In: *Concepts in Magnetic Resonance* 11.2 (Jan. 1999), pp. 61–70.

[103] D I Hoult and R E Richards. "The signal-to-noise ratio of the nuclear magnetic resonance experiment". In: *Journal of Magnetic Resonance* 24.1 (Oct. 1976), pp. 71–85.

[104] T L Peck, R L Magin, and P C Lauterbur. "Design and Analysis of Microcoils for NMR Microscopy". In: *Journal of Magnetic Resonance* (1995), pp. 1–11.

[105] Ching-nien Chen and D I Hoult. *Biomedical Magnetic Resonance Technology*. CRC Press, Jan. 1989.

[106] A G Webb and S C Grant. "Signal-to-noise and magnetic susceptibility trade-offs in solenoidal microcoils for NMR". In: *Journal of Magnetic Resonance* 113 (1996), pp. 88–87.

[107] Nicoleta Baxan et al. "Limit of detection of cerebral metabolites by localized NMR spectroscopy using microcoils". In: *Comptes Rendus Chimie* 11.4-5 (Apr. 2008), pp. 448–456.

[108] Axel Haase et al. "NMR probeheads forin vivo applications". In: *Concepts in Magnetic Resonance Part B: Magnetic Resonance Engineering* 12.6 (2000), pp. 361–388.

[109] Daniel D Traficante. "Impedance: What it is, and why it must be matched". In: *Concepts in Magnetic Resonance Part B: Magnetic Resonance Engineering* 1.2 (1989), pp. 73–92.

[110] Daniel D Traficante. "Maximum Power Transfer and Percent Efficiency: Which Is More Important?" In: *Concepts in Magnetic Resonance* 9.1 (Jan. 1997), pp. 13–16.

[111] National Electrical Manufacturers Association. *Determination of Two-Dimensional Geometric Distortion in Diagnostic Magnetic Resonance Images.* standards publication MS, 2008.

[112] National Electrical Manufacturers Association. Determination of Signal-to-Noise Ratio (SNR) in Diagnostic Magnetic Resonance Imaging. NEMA Standards Publication MS, 2008.

[113] Frederic H Martini, Michael J Timmons, and Robert B Tallitsch. *Anatomie.* 2012.

[114] Gerhard Aumueller et al. *Duale Reihe Anatomie.* Georg Thieme Verlag, Oct. 2014.

[115] Kenneth W Horch and Gurpreet S Dhillon. *Neuroprosthetics Theory and Practice.* World Scientific, 2004.

[116] R S Fisher et al. "Epileptic Seizures and Epilepsy: Definitions Proposed by the International League Against Epilepsy (ILAE) and the International Bureau for Epilepsy (IBE)". In: *Epilepsia* 46.4 (2005), pp. 470–472.

[117] Robert S Fisher et al. "ILAE Official Report: A practical clinical definition of epilepsy". In: *Epilepsia* 55.4 (2014), pp. 475–482.

[118] Helen E Scharfman. "The neurobiology of epilepsy". In: *Current Neurology and Neuroscience Reports* 7.4 (July 2007), pp. 348–354.

[119] Asla Pitkänen. "Therapeutic approaches to epileptogenesis-Hope on the horizon". In: *Epilepsia* 51 (July 2010), pp. 2–17.

[120] Annamaria Vezzani. "Before Epilepsy Unfolds: Finding the epileptogenesis switch". In: *Nature Medicine* 18.11 (Nov. 2012), pp. 1626–1627.

[121] Robert F III Hunt, Jeffery A Boychuk, and Bret N Smith. "Neural circuit mechanisms of post–traumatic epilepsy". In: *Frontiers in Cellular Neuroscience* 7 (2013).

[122] Patrick Kwan et al. "Definition of drug resistant epilepsy: Consensus proposal by the ad hoc Task Force of the ILAE Commission on Therapeutic Strategies". In: *Epilepsia* 51.6 (Nov. 2009), pp. 1069–1077.

[123] Massimo Avoli et al. "Cellular and molecular mechanisms of epilepsy in the human brain". In: *Progress in Neurobiology* 77.3 (Oct. 2005), pp. 166–200.

[124] A Pitkänen and K Lukasiuk. "Mechanisms of epileptogenesis and potential treatment targets". In: *The Lancet Neurology* 10 (2011), pp. 173–186.

[125] Ethan M Goldberg and Douglas A Coulter. "Mechanisms of epileptogenesis: a convergence on neural circuit dysfunction". In: *Nature Reviews Neuroscience* 14.5 (Apr. 2013), pp. 337–349.

[126] A Pitkänen and J Engel Jr. "Past and Present Definitions of Epileptogenesis and Its Biomarkers". In: *Neurotherapeutics* (2014).

[127] David W McCandless. *Epilepsy*. Animal and Human Correlations. Springer, Nov. 2011.

[128] Wei Deng, James B Aimone, and Fred H Gage. "New neurons and new memories: how does adult hippocampal neurogenesis affect learning and memory?" In: *Nature Reviews Neuroscience* 11.5 (Mar. 2010), pp. 339–350.

[129] Peter S Eriksson et al. "Neurogenesis in the adult human hippocampus". In: *Nature Medicine* 4.11 (Nov. 1998), pp. 1313–1317.

[130] J Gerlach et al. "Persistent gliosis interferes with neurogenesis in organotypic hippocampal slice cultures". In: *Frontiers in Cellular Neuroscience* 10 (2016), p. 131.

[131] David G Amaral, Helen E Scharfman, and Pierre Lavenex. "The dentate gyrus: fundamental neuroanatomical organization (dentate gyrus for dummies)". In: Elsevier, 2007, pp. 3–790.

[132] Alejandra Sierra et al. "Diffusion tensor imaging of hippocampal network plasticity". In: *Brain Structure and Function* (Dec. 2013).

[133] Stanley Jacobson and Elliott M Marcus. *Neuroanatomy for the Neuroscientist*. Springer Science & Business Media, Dec. 2011.

[134] J Noraberg, B W Kristensen, and J Zimmer. "ScienceDirect.com - Brain Research Protocols - Markers for neuronal degeneration in organotypic slice cultures". In: *Brain Research Protocols* (1999).

[135] Jean-Pierre Dollé et al. "An organotypic uniaxial strain model using microfluidics". In: *Lab on a Chip* 13.3 (2013), pp. 432–442.

[136] Richard Kovács, Ismini Papageorgiou, and Uwe Heinemann. "Slice Cultures as a Model to Study Neurovascular Coupling and Blood Brain Barrier In Vitro". In: *Cardiovascular Psychiatry and Neurology* 2011.5 (2011), pp. 1–9.

[137] My Andersson et al. "Optogenetic control of human neurons in organotypic brain cultures". In: *Scientific Reports* 6 (Apr. 2016), p. 24818.

[138] C Kang et al. "Human Organotypic Cultured Cardiac Slices: New Platform For High Throughput Preclinical Human Trials". In: *Scientific Reports* 6 (2016).

[139] G K Aghajanian and K Rasmussen. "Intracellular studies in the facial nucleus illustrating a simple new method for obtaining viable motoneurons in adult rat brain slices - Aghajanian - 2004 - Synapse - Wiley Online Library". In: *Synapse* (1989).

[140] G R Seabrook, W Howson, and M G Lacey. "Electrophysiological characterization of potent agonists and antagonists at pre- and postsynaptic GABAB receptors on neurones in rat brain slices". In: *British Journal of Pharmacology* 101.4 (1990), pp. 949–957.

[141] Trent A Basarsky et al. "Imaging Spreading Depression and Associated Intracellular Calcium Waves in Brain Slices". In: *The Journal of Neuroscience* 18.8 (1998), pp. 7189–7199.

[142] John Connor et al. "Calcium Signaling in Dendritic Spines of Hippocampal Neurons". In: *Journal of Neurobiology* (1993), pp. 1–9.

[143] John Dunlop et al. "High-throughput electrophysiology: an emerging paradigm for ion-channel screening and physiology". In: *Nature Reviews Drug Discovery* 7.4 (Apr. 2008), pp. 358–368.

[144] Shaokoon Cheng and Lynne E Bilston. "Unconfined compression of white matter". In: *Journal of Biomechanics* 40.1 (Jan. 2007), pp. 117–124.

[145] X Chai et al. "Epilepsy-Induced Motility of Differentiated Neurons". In: *Cerebral Cortex* 24.8 (July 2014), pp. 2130–2140.

[146] I E Holopainen. "Organotypic Hippocampal Slice Cultures: A Model System to Study Basic Cellular and Molecular Mechanisms of Neuronal Cell Death, Neuroprotection, and Synaptic Plasticity". In: *Neurochemical research* 30.12 (2005), pp. 1521–1528.

[147] Orrin Devinsky et al. "Glia and epilepsy: excitability and inflammation". In: *Trends in Neurosciences* (Jan. 2013), pp. 1–11.

[148] F Suzuki et al. "Morphogenetic effect of kainate on adult hippocampal neurons associated with a prolonged expression of brain-derived neurotrophic factor". In: *Neuroscience* 64.3 (Feb. 1995), pp. 665–674.

[149] J Engel. "Introduction to temporal lobe epilepsy". In: *Epilepsy research* 26 (1996), pp. 141–150.

[150] G J Harry and C Lefebvre d'Hellencourt. "Dentate Gyrus: Alterations that Occur with Hippocampal Injury". In: *Neurotoxicology* 24 (2003), pp. 343–356.

[151] J M Fritschy. "A New Animal Model of Temporal Lobe Epilepsy". In: *Epileptologie* (2004).

[152] G Panuccio et al. "In vitro ictogenesis and parahippocampal networks in a rodent model of temporal lobe epilepsy". In: *Neurobiology of Disease* 39.3 (Sept. 2010), pp. 372–380.

[153] C Heinrich et al. "Reelin Deficiency and Displacement of Mature Neurons, But Not Neurogenesis, Underlie the Formation of Granule Cell Dispersion in the Epileptic Hippocampus". In: *Journal of neuroscience . . .* 26.17 (2006), pp. 4701–4713.

[154] Philipp Janz et al. "Synaptic Remodeling of Entorhinal Input Contributes to an Aberrant Hippocampal Network in Temporal Lobe Epilepsy". In: *Cerebral Cortex* (2016), pp. 1–17.

[155] Gudrun Lang. *Histotechnik*. Praxislehrbuch für die Biomedizinische Analytik. Springer-Verlag, Nov. 2012.

[156] N Pilati et al. "A Rapid Method Combining Golgi and Nissl Staining to Study Neuronal Morphology and Cytoarchitecture". In: *Journal of Histochemistry and Cytochemistry* 56.6 (May 2008), pp. 539–550.

[157] R D Palmiter, T B Cole, and C J Quaife. "ZnT-3, a putative transporter of zinc intosynapticvesicles". In: *Proceedings of the National Academy of Sciences*. 1996, pp. 14934–14939.

[158] V V Gusel'nikova and D E Korzhevskiy. "NeuN as a neuronal nuclear antigen and neuron differentiation marker". In: *Acta Naturae* 7.2 (25) (2015).

[159] D Sakellariou, G Le Goff, and J F Jacquinot. "High-resolution, high-sensitivity NMR of nanolitre anisotropic samples by coil spinning". In: *Nature* 447.7145 (June 2007), pp. 694–697.

[160] Henk Wensink et al. "Measuring reaction kinetics in a lab-on-a-chip by microcoil NMR". In: *Lab on a Chip* 5.3 (2005), p. 280.

[161] Stefan Glöggler et al. "In vivo online magnetic resonance quantification of absolute metabolite concentrations in microdialysate". In: *Scientific Reports* 6 (Nov. 2016), p. 36080.

[162] Sergey S Zalesskiy et al. "Miniaturization of NMR Systems: Desktop Spectrometers, Microcoil Spectroscopy, and "NMR on a Chip" for Chemistry, Biochemistry, and Industry". In: *Chemical Reviews* 114.11 (Apr. 2014), pp. 5641–5694.

[163] R Kamberger et al. "Induktiv Gekoppelte Detektoren fuer multinukleare Kernspinresonanzspektroskopie: Vorlaeufige Ergebnisse ". In: *Proceedings MikroSystemTechnik Kongress 2013* (2013).

[164] C Massin et al. "Planar microcoil-based microfluidic NMR probes". In: *Journal of Magnetic Resonance* 164.2 (Oct. 2003), pp. 242–255.

[165] D L Olson et al. "High-Resolution Microcoil 1H-NMR for Mass-Limited, Nanoliter-Volume Samples". In: *Science* 270.5244 (Dec. 1995), pp. 1967–1970.

[166] Wolfgang Menz, Jürgen Mohr, and Oliver Paul. *Microsystem Technology*. John Wiley & Sons, July 2008.

[167] Marc J Madou. *Fundamentals of Microfabrication*. The Science of Miniaturization, Second Edition. CRC Press, Mar. 2002.

[168] C Massin et al. "High-Q factor RF planar microcoils for micro-scale NMR spectroscopy". In: *Sensors and Actuators A: Physical* 97 (May 2002), pp. 280–288.

[169] Sertac Eroglu et al. "NMR spiral surface microcoils: Design, fabrication, and imaging". In: *Concepts in Magnetic Resonance Part B: Magnetic Resonance Engineering* 17B.1 (2003), pp. 1–10.

[170] R R A Syms et al. "MEMS Helmholtz coils for magnetic resonance imaging". In: *Journal of Micromechanics and Microengineering* 15.7 (June 2005), S1–S9.

[171]   S Leidich, M Braun, and T Gessner. "Silicon cylinder spiral coil for nuclear magnetic resonance spectroscopy of nanoliter samples ". In: *Concepts in Magnetic Resonance Part B: Engineering* (2009).

[172]   M Woytasik et al. "Characterization of flexible RF microcoils dedicated to local MRI". In: *Microsystem Technologies* 13.11-12 (Nov. 2006), pp. 1575–1580.

[173]   M Woytasik et al. "Two- and three-dimensional microcoil fabrication process for three-axis magnetic sensors on flexible substrates". In: *Sensors and Actuators A: Physical* 132.1 (Nov. 2006), pp. 2–7.

[174]   Eric Moore and Robert Tycko. "Micron-scale magnetic resonance imaging of both liquids and solids". In: *Journal of Magnetic Resonance* 260 (Nov. 2015), pp. 1–9.

[175]   J Anders, J Handwerker, and M Ortmanns. "A low-power high-sensitivity single-chip receiver for NMR microscopy". In: *Journal of Magnetic Resonance* 266 (2016), pp. 41–50.

[176]   Jens Anders et al. "A single-chip array of NMR receivers". In: *Journal of Magnetic Resonance* 201.2 (Dec. 2009), pp. 239–249.

[177]   M Grisi, G Gualco, and G Boero. "A broadband single-chip transceiver for multi-nuclear NMR probes". In: *Review of Scientific Instruments* (2015).

[178]   Dean L Olson, Michael E Lacey, and Jonathan V Sweedler. "High-Resolution Microcoil NMR for Analysis of Mass-Limited, Nanoliter Samples". In: *Analytical Chemistry* 70.3 (Feb. 1998), pp. 645–650.

[179]   S J Dodd et al. "Detection of Single Mammalian Cells by High-Resolution Magnetic Resonance Imaging". In: *Biophysical journal* (1999).

[180]   Mona J K Klein et al. "Process for the fabrication of hollow core solenoidal microcoils in borosilicate glass". In: *Journal of Micromechanics and Microengineering* 18.7 (2008), p. 075002.

[181]   John A Rogers et al. "Using microcontact printing to fabricate microcoils on capillaries for high resolution proton nuclear magnetic resonance on nanoliter volumes". In: *Applied Physics Letters* 70.18 (1997), p. 2464.

[182]   Vasiliki Demas et al. "Electronic characterization of lithographically patterned microcoils for high sensitivity NMR detection". In: *Journal of Magnetic Resonance* 200.1 (Sept. 2009), pp. 56–63.

[183]   Vasiliki Demas et al. "Portable, low-cost NMR with laser-lathe lithography produced microcoils". In: *Journal of Magnetic Resonance* 189.1 (Nov. 2007), pp. 121–129.

[184]   S Goto, T Matsunaga, and Y Matsuoka. "Development of High-Resolution Intraluminal and Intravascular MRI Probe Using Microfabrication on Cylindrical Substrates ". In: *IEEE MEMS* (2007).

[185]   K Kratt et al. "High aspect ratio PMMA posts and characterization method for micro coils manufactured with an automatic wire bonder". In: *Sensors and Actuators A: Physical* 156 (2009), pp. 328–333.

[186]   K Kratt et al. "A fully MEMS-compatible process for 3D high aspect ratio micro coils obtained with an automatic wire bonder". In: *Journal of Micromechanics and Microengineering* 20.1 (Dec. 2009), p. 015021.

[187]   N Spengler et al. "Heteronuclear Micro-Helmholtz Coil Facilitates μm-Range Spatial and Sub-Hz Spectral Resolution NMR of nL-Volume Samples on Customisable Microfluidic Chips - ProQuest". In: *PLOS ONE* (2016).

[188]   K Göbel et al. "Phased-array of microcoils allows MR microscopy of ex vivo human skin samples at 9.4 T ". In: *Skin Research and Technology* (2014).

[189]   L Ciobanu, D A Seeber, and C H Pennington. "3D MR microscopy with resolution 3.7μm by 3.3μm by 3.3μm". In: *Journal of Magnetic Resonance* (2002).

[190]   D A Seeber et al. "Design and testing of high sensitivity microreceiver coil apparatus for nuclear magnetic resonance and imaging". In: *Review of Scientific Instruments* 72.4 (Apr. 2001), pp. 2171–2179.

[191]   J D Trumbull et al. "Integrating microfabricated fluidic systems and NMR spectroscopy". In: *IEEE Transactions on Biomedical Engineering* 47.1 (2000), pp. 3–7.

[192] L Renaud et al. "Implantable planar rf microcoils for NMR microspectroscopy". In: *Sensors and Actuators A . . .* 99 (2002), pp. 244–248.

[193] D Rugar et al. "Single spin detection by magnetic resonance force microscopy". In: *Nature* 430.6997 (July 2004), pp. 329–332.

[194] Ivan Tobias Tomka. *Methods in Magnetic Resonance Force Microscopy*. Swiss Federal Institut of Technology. 2014.

[195] A C Fischer et al. "Unconventional applications of wire bonding create opportunities for microsystem integration". In: *Journal of Micromechanics and Microengineering* 23.8 (June 2013), p. 083001.

[196] R Kamberger et al. "Hollow microcoils made possible with external support structures manufactured with a two-solvent process". In: *Journal of Micromechanics and Microengineering* 26.6 (2016), p. 065002.

[197] J Bühler, F-P Steiner, and H Baltes. "Silicon dioxide sacrificial layer etching in surface micromachining". In: *Journal of Micromechanics and Microengineering* 7.1 (1997), R1–R13.

[198] W Lang et al. "Application of porous silicon as a sacrificial layer". In: *Sensors and Actuators A: Physical* 43.1-3 (May 1994), pp. 239–242.

[199] Bridget A Peeni et al. "Sacrificial layer microfluidic device fabrication methods". In: *ELECTROPHORESIS* 27.24 (Dec. 2006), pp. 4888–4895.

[200] Norbert Kockmann. *Micro Process Engineering*. John Wiley & Sons, Sept. 2008.

[201] A Bagolini et al. "Polyimide sacrificial layer and novel materials for post-processing surface micromachining". In: *Journal of Micromechanics and Microengineering* 12.4 (June 2002), pp. 385–389.

[202] Jasbir N Patel et al. "PDMS as a sacrificial substrate for SU-8-based biomedical and microfluidic applications". In: *Journal of Micromechanics and Microengineering* 18.9 (Aug. 2008), p. 095028.

[203] Vincent Linder et al. "Water-Soluble Sacrificial Layers for Surface Micromachining". In: *Small* 1.7 (July 2005), pp. 730–736.

[204] Nicholas Ferrell, James Woodard, and Derek Hansford. "Fabrication of polymer microstructures for MEMS: sacrificial layer micromolding and patterned substrate micromolding". In: *Biomedical Microdevices* 9.6 (June 2007), pp. 815–821.

[205] O G Gruschke et al. "Water-soluble sacrificial layer enables ultra low-cost LOC integration of magnetic resonance microcoils with 100 per cent filling factor". In: *2013 Transducers & Eurosensors XXVII: The 17th International Conference on Solid-State Sensors, Actuators and Microsystems (TRANSDUCERS & EUROSENSORS XXVII)*. IEEE, 2013, pp. 132–134.

[206] A Moazenzadeh et al. "Analysis of packaging effects on wire bonder made microtransformer chips". In: *Journal of Physics: Conference Series* 476.1 (2013), p. 012110.

[207] L O Sillerud, A F McDowell, and N L Adolphi. "1H NMR Detection of superparamagnetic nanoparticles at 1T using a microcoil and novel tuning circuit". In: *Journal of Magnetic Resonance* 181 (2006), pp. 181–190.

[208] Herbert Ryan, Alison Smith, and Marcel Utz. "Structural shimming for high-resolution nuclear magnetic resonance spectroscopy in lab-on-a-chip devices". In: *Lab on a Chip* 14 (2014), pp. 1678–1685.

[209] D I Hoult and B Tomanek. "Use of mutually inductive coupling in probe design". In: *Concepts in Magnetic Resonance Part B: Magnetic Resonance Engineering* 15.4 (Dec. 2002), pp. 262–285.

[210] Philip L Kuhns et al. "Inductive coupling and tuning in NMR probes; Applications". In: *Journal of Magnetic Resonance (1969)* 78.1 (June 1988), pp. 69–76.

[211] Mehmet Bilgen, Ibrahim Elshafiey, and Ponnada A Narayana. "In Vivo Magnetic Resonance Microscopy of Rat Spinal Cord at 7 T Using Implantable RF Coils". In: *Magnetic Resonance in Medicine* 46 (2001), pp. 1250–1253.

[212] Harald H Quick et al. "Inductively coupled stent antennas in MRI". In: *Magnetic Resonance in Medicine* 48.5 (Nov. 2002), pp. 781–790.

[213] Marcel Utz and Reza Monazami. "Nuclear magnetic resonance in microfluidic environments using inductively coupled radiofrequency resonators". In: *Journal of Magnetic Resonance* 198.1 (May 2009), pp. 132–136.

[214] M D Schnall et al. "Wireless implanted magnetic resonance probes for in vivo NMR". In: *Journal of Magnetic Resonance (1969)* 68.1 (June 1986), pp. 161–167.

[215] J Schoenmaker, K R Pirota, and J C Teixeira. "Magnetic flux amplification by Lenz lenses". In: *Review of Scientific Instruments* 84.085120 (2013).

[216] Nils Spengler et al. "Magnetic Lenz lenses increase the limit-of-detection in nuclear magnetic resonance". In: *arXiv.org* (June 2016).

[217] Nils Spengler. "Modular MicroNMR Probe". PhD thesis. University of Freiburg, 2015.

[218] C Birkl, C Langkammer, and N Golob Schwarzl. "Effects of formalin fixation and temperature on MR relaxation times in the human brain". In: *NMR in Biomedicine* (2016).

[219] Armin Purea and Andrew G Webb. "Reversible and irreversible effects of chemical fixation on the NMR properties of single cells". In: *Magnetic Resonance in Medicine* 56.4 (2006), pp. 927–931.

[220] Klaus Schmierer et al. "Quantitative magnetic resonance of postmortem multiple sclerosis brain before and after fixation". In: *Magnetic Resonance in Medicine* 59.2 (2008), pp. 268–277.

[221] Young-tae Kim et al. "Neuro-optical microfluidic platform to study injury and regeneration of single axons". In: *Lab on a Chip* 9.17 (2009), p. 2576.

[222] YoonYoung Yi et al. "Central Nervous System and its Disease Models on a Chip". In: *Trends in Biotechnology* 33.12 (Dec. 2015), pp. 762–776.

[223] J Liu et al. "Perfused drop microfluidic device for brain slice culture-based drug discovery - Springer". In: *Biomedical Microdevices* (2016).

[224] N J Killian, V N Vernekar, and S M Potter. "A Device for Long-Term Perfusion, Imaging, and Electrical Interfacing of Brain Tissue In vitro". In: *Frontiers in Neuroscience* 10 (2016), p. 135.

[225] Ville Jokinen et al. "A microfluidic chip for axonal isolation and electrophysiological measurements". In: *Journal of Neuroscience Methods* 212.2 (Jan. 2013), pp. 276–282.

[226] H Xu, S F Othman, and R L Magin. "Monitoring Tissue Engineering Using Magnetic Resonance Imaging". In: *Journal of bioscience and bioengineering* (2008).

[227] Huihui Xu et al. "Magnetic resonance microscopy for monitoring osteogenesis in tissue-engineered construct in vitro". In: *Physics in Medicine and Biology* 51.3 (Jan. 2006), pp. 719–732.

[228] R D Abbott et al. "Long term perfusion system supporting adipogenesis". In: *Methods* (2015).

[229] I E Chesnick et al. "Evaluation of bioreactor-cultivated bone by magnetic resonance microscopy and FTIR microspectroscopy". In: *Bone* (2007).

[230] G Eidmann et al. "The NMR MOUSE, a Mobile Universal Surface Explorer". In: *Journal of Magnetic Resonance, Series A* 122.1 (Sept. 1996), pp. 104–109.

[231] B Blümich et al. "The NMR-mouse: construction, excitation, and applications". In: *Magnetic Resonance Imaging* 16.5 (1998), pp. 479–484.

[232] A De Simoni and M Y Lily. "Preparation of organotypic hippocampal slice cultures: interface method : Abstract : Nature Protocols". In: *Nature Protocols* (2006).

[233] L Stoppini, P A Buchs, and D Muller. "ScienceDirect.com - Journal of Neuroscience Methods - A simple method for organotypic cultures of nervous tissue". In: *Journal of Neuroscience Methods* (1991).

[234] Nadine Gogolla et al. "Long-term live imaging of neuronal circuits in organotypic hippocampal slice cultures". In: *Nature Protocols* 1.3 (Sept. 2006), pp. 1223–1226.

[235] Nadine Gogolla et al. "Preparation of organotypic hippocampal slice cultures for long-term live imaging". In: *Nature Protocols* 1.3 (Sept. 2006), pp. 1165–1171.

[236] Matthias C Wapler et al. "Magnetic properties of materials for MR engineering, micro-MR and beyond". In: *Journal of Magnetic Resonance* 242 (Mar. 2014), pp. 233–242.

[237] John F Schenck. "The role of magnetic susceptibility in magnetic resonance imaging: MRI magnetic compatibility of the first and second kinds". In: *Medical Physics* 23.6 (1996), pp. 1–36.

[238] D Li et al. "Reperfusion accelerates acute neuronal death induced by simulated ischemia". In: *Experimental neurology* (2007).

[239] B Morrison et al. "Traumatic injury induces differential expression of cell death genes in organotypic brain slice cultures determined by complementary DNA array hybridization". In: *Neuroscience* 96 (2000), pp. 131–139.

[240] Pamela W Schaefer et al. "Assessing Tissue Viability with MR Diffusion and Perfusion Imaging". In: *American Journal of Neuroradiology* 24 (2003), pp. 436–443.

[241] G A Johnson et al. "High-throughput morphologic phenotyping of the mouse brain with magnetic resonance histology". In: *NeuroImage* (2007).

[242] Johnson GA et al. "Histology by magnetic resonance microscopy." In: *Magnetic resonance quarterly* 9.1 (Jan. 1993), pp. 1–30.

[243] J J Flint, B Hansen, and S J Blackband. "Diffusion tensor microscopy data (15.6μm in-plane) of white matter tracts in the human, pig, and rat spinal cord with corresponding tissue histology". In: *Data in Brief* (2016).

[244] Evan Calabrese et al. "A Diffusion MRI Tractography Connectome of the Mouse Brain and Comparison with Neuronal Tracer Data". In: *Cerebral Cortex* (2015), pp. 1–10.

[245] L S Cahill et al. "Preparation of fixed mouse brains for MRI". In: *NeuroImage* (2012).

[246] R J Dawe et al. "Postmortem MRI of human brain hemispheres: T2 relaxation times during formaldehyde fixation". In: *Magnetic Resonance in Medicine* 61 (2009), pp. 810–818.

[247] Sara van Duijn et al. "MRI artifacts in human brain tissue after prolonged formalin storage". In: *Magnetic Resonance in Medicine* 65.6 (2011), pp. 1750–1758.

[248] Jason P Lerch et al. "Wanted dead or alive? The tradeoff between in-vivo versus ex-vivo MR brain imaging in the mouse". In: *Frontiers in Neuroinformatics* 6 (2012).

[249] I Oguz et al. "PLOS ONE: Comparison of Magnetic Resonance Imaging in Live vs. Post Mortem Rat Brains". In: *PLOS ONE* (2013).

[250] H E D'Arceuil, S Westmoreland, and A J de Crespigny. "An approach to high resolution diffusion tensor imaging in fixed primate brain". In: *NeuroImage* (2007).

[251] Timothy M Shepherd et al. "Postmortem interval alters the water relaxation and diffusion properties of rat nervous tissue — Implications for MRI studies of human autopsy samples". In: *NeuroImage* 44.3 (Feb. 2009), pp. 820–826.

[252] A E de Guzman et al. "Variations in post-perfusion immersion fixation and storage alter MRI measurements of mouse brain morphometry". In: *NeuroImage* (2016).

[253] Timothy M Shepherd et al. "MR microscopy of rat hippocampal slice cultures: A novel model for studying cellular processes and chronic perturbations to tissue microstructure". In: *NeuroImage* 30.3 (Apr. 2006), pp. 780–786.

[254] Jung Ho Lee, Yusuke Okuno, and Silvia Cavagnero. "Sensitivity enhancement in solution NMR: Emerging ideas and new frontiers". In: *Journal of Magnetic Resonance* 241 (Apr. 2014), pp. 18–31.

[255] E A Nanni et al. "Microwave field distribution in a magic angle spinning dynamic nuclear polarization NMR probe". In: *Journal of Magnetic Resonance* 210 (2011), pp. 16–23.

[256] C D Paepe et al. *Structure of viral nucleocapsid by solid-state NMR at 100 kHz magic-angle spinning.* 41st FEBS Congress on Molecular and Systems Biology for a Better Life, 2016.

[257] A Boekmann, M Ernst, and B H Meier. "Spinning proteins, the faster, the better?" In: *Journal of Magnetic Resonance* (2015).

[258] D Le Bihan et al. "Diffusion tensor imaging: Concepts and applications". In: *Journal of Magnetic Resonance Imaging* 13 (2001), pp. 534–546.

[259] Alan Jasanoff. "Bloodless fMRI". In: *Trends in Neurosciences* 30.11 (Nov. 2007), pp. 603–610.

[260]   Denis Le Bihan and Mami Iima. "Diffusion Magnetic Resonance Imaging: What Water Tells Us about Biological Tissues". In: *PLOS Biol* 13.7 (2015), e1002203.

[261]   William I Jay et al. "Is it possible to detect dendrite currents using presently available magnetic resonance imaging techniques?" In: *Medical & Biological Engineering & Computing* 50.7 (Mar. 2012), pp. 651–657.

[262]   R Biran, D C Martin, and P A Tresco. "Neuronal cell loss accompanies the brain tissue response to chronically implanted silicon microelectrode arrays". In: *Experimental neurology* (2005).

[263]   V S Polikov, P A Tresco, and W M Reichert. "Response of brain tissue to chronically implanted neural electrodes". In: *Journal of Neuroscience Methods* (2005).

[264]   Barbara Jobst and George Thomas. "Critical review of the responsive neurostimulator system for epilepsy". In: *Medical Devices: Evidence and Research* 8 (Oct. 2015), p. 405.

[265]   N S Birnbaum and H B Aaronson. "Dental impressions using 3D digital scanners: virtual becomes reality". In: *Compend Contin Educ Dent* (2008).

[266]   T V Flügge et al. "Precision of intraoral digital dental impressions with iTero and extraoral digitization with the iTero and a model scanner". In: *American Journal of Orthodontics and Dentohacial Orthopedics* 144.3 (2013), pp. 471–478.

[267]   K Hiraishi et al. "Blueberry juice: preliminary evaluation as an oral contrast agent in gastrointestinal MR imaging." In: *Radiology* 194.1 (Jan. 1995), pp. 119–123.

[268]   Jan-Bernd Hövener et al. "Dental MRI: Imaging of soft and solid components without ionizing radiation". In: *Journal of Magnetic Resonance Imaging* 36.4 (2012), pp. 841–846.

[269]   Matthias Echternach et al. "Articulation and vocal tract acoustics at soprano subject's high fundamental frequencies". In: *The Journal of the Acoustical Society of America* 137.5 (May 2015), pp. 2586–2595.

Journal Articles

[RK1] **R. Kamberger**, K. Goebel-Guéniot, J. Gerlach, O.G. Gruschke, J. Hennig, P. LeVan, C. Haas, J.G. Korvink; *Method for MR imaging of tissue cultured with the interface culturing method using Lenz lenses*, Magnetic Resonance Imaging, in preparation

[RK2] K. Goebel-Guéniot, J. Gerlach, **R. Kamberger**, D. von Elverfeldt, J. Hennig, J.G. Korvink, C. Haas, P. LeVan; *Direct histological validation of micro-MR of healthy and pathological mouse brain microstructure*, NeuroImage, in preparation

[RK3] M. Jouda, **R. Kamberger**, J. Leupold, N. Spengler, J. Hennig, J.G. Korvink and O.G. Gruschke; *Zooming in: Is resonant inductive coupling the best we can do in magnetic resonance?*, Journal of Magnetic Resonance, in preparation

[RK4] L. Traser, P. Birkholz, T. Flügge, **R. Kamberger**, M. Burdumy, B. Richter, J.G. Korvink and M. Echternach; *Relevance of teeth implementation in three dimensional vocal tract models*, Journal of Speech, Language, and Hearing Research, in press

[RK5] **R. Kamberger**, A. Moazenzadeh, J.G. Korvink and O.G. Gruschke; *Hollow microcoils made possible with external support structures manufactured with a two-solvent process.*, Journal of Micromechanics and Microengineering, 26, 8 pp, 065002, 2016

[RK6] L. Traser, T. Fluegge, M. Burdumy, **R. Kamberger**, B. Richter, F. Hassepass, J.G. Korvink, M. Echternach; *A Comparison of Different Methods to Generate Tooth Surface Models Without Applying Ionizing Radiation for Digital Three-Dimensional Image Fusion With MRI Based Data of the Head and Neck Region*, Journal of Computer Assisted Tomography, 39(6), pp. 882-889, 2015

[RK7] M. Echternach, P. Birkholz, L. Traser, T. Fluegge, **R. Kamberger**, F. Burk, M. Burdumy, B. Richter; *Articulation and vocal tract acoustics at soprano subject's high fundamental frequencies*, Journal of the Acoustical Society of America, 137 (5), pp. 2586-2595, 2015

Conference Contributions

[RK8] **R. Kamberger**, O.G. Gruschke, J.G. Korvink; *MR Microscopy using Lenz Lenses*, ESMRMB Congress 2016, Vienna, Austria.

[RK9] K. Goebel-Guéniot, J. Gerlach, **R. Kamberger**. J. Leupold, D. von Elverfeldt, J.G. Korvink, J. Hennig, C. Haas, P LeVan; *Insights into cellular hippocampal networks using Magnetic Resonance Microscopy at 7 T.*, WMIC 2016, New York, USA.

[RK10] J. Anders, J. Handwerker, M. Ortmanns, **R. Kamberger**, J.G. Korvink, O.G. Gruschke; *Arrays od IC-assisted 3D-microcoils for wideband NMR spectroscopy.*, EUROMAR 2016, Aarhus, Denmark

[RK11] **R. Kamberger**, K. Goebel, J. Gerlach, O.G. Gruschke, P. LeVan, J. Leupold, D. von Elverfeldt, J. Hennig, C. Haas, J.G. Korvink; *Magnetresonanz-kompatibler Mini-Inkubator für die Untersuchung von Epileptogenese in vitro.*,Mikrosystemtechnik Kongress 2015, Karlsruhe

[RK12] K. Goebel, **R. Kamberger**, J. Gerlach, J. Leupold, D. von Elverfeldt, J.G. Korvink, C. Haas, J. Hennig, P. LeVan; *Investigation of cellular-level alterations in a hippocampal slice model using MR microscopy*, MoBi Conference 2015, Freiburg, Germany

[RK13] **R. Kamberger**, K. Goebel, J. Gerlach, O.G. Gruschke, P. LeVan, J. Leupold, D. von Elverfeldt, J. Hennig, C. Haas, J.G. Korvink; *Merging Brain Slice Culturing and Magnetic Resonance Microscopy*, ICMRM 2015, Munich, Germany

[RK14] K. Goebel, J. Gerlach, **R. Kamberger**, J. Leupold, D. von Elverfeldt, J.G. Korvink, C. Haas, J. Hennig, P. LeVan; *Cellular-level Alterations in Epileptogenesis - MR Microscopy of Organotypic Hippocampal Slice Cultures*, ICMRM 2015, Munich, Germany

[RK15] **R. Kamberger**, K. Goebel, J. Gerlach, O.G. Gruschke, P. LeVan, J. Leupold, D. von Elverfeldt, J. Hennig, C. Haas, J.G. Korvink; *MR-Compatible Mini-Incubator for in vitro studies of epileptogenesis in organotypic hippocampal slice cultures.*, EUROMAR 2015, Prag, Tschechien

[RK16] K. Göbel, J. Gerlach, **R. Kamberger**, J. Leupold, D. von Elverfeldt, C. Haas, J.G. Korvink, J. Hennig, P. LeVan; *Micro-MR correlates of cellular-level alterations in epileptogenesis*, ISMRM 2015, Toronto, Canada

[RK17] K. Göbel, J. Leupold, B. Dhital, P. LeVan, M. Reisert, J. Gerlach, **R. Kamberger**, C. Haas, J. Hennig, D. von Elverfeldt, J.G. Korvink; *MR Microscopy and DTI of Organotypic Hippocampal Slice Cultures*, ISMRM 2014, Milano, Italy

[RK18] **R. Kamberger**, O.G. Gruschke, K. Göbel, J.B. Hoevener, D. Elverfeldt, M. Utz und J.G. Korvink; *Induktiv Gekoppelte Detektoren fuer multinukleare Kernspinresonanzspektroskopie: Vorlaeufige Ergebnisse*, Mikrosystemtechnik Kongress 2013, Aachen

[RK19] O.G. Gruschke, **R. Kamberger**, J. Hoefflin, J.G. Korvink; *Wasser-loesliche Opferschicht ermooeglicht die low-cost Herstellung von Mikrospulen mit einem Fuellgrad von 100 %.* Mikrosystemtechnik Kongress 2013, Aachen

[RK20] K. Goebel, **R. Kamberger**, J. Gerlach, O.G. Gruschke, J. Leupold, P. LeVan, D. von Elverfeldt, J.G. Korvink, C. Haas, J. Hennig; *MR Microscopy of Organotypic Hippocampal Slice Cultures: A First Look on the Anatomy*, 16th Ann. Meet. Ger. Chapter Int. Soc. Magn. Reson. Med. 2013, Freiburg

[RK21] K. Goebel, **R. Kamberger**, J. Gerlach, O.G. Gruschke, J. Leupold, P. LeVan, D. von Elverfeldt, J.G. Korvink, C. Haas, J. Hennig; *MR Microscopy of Organotypic Hippocampal Slice Cultures: First Steps to an In Vitro Approach for Experimental Epilepsy Research*, 12th International Conference on MR Microscopy, 2013, Cambridge, UK

[RK22] O.G. Gruschke, **R. Kamberger**, J. Hoefflin, J.G. Korvink; *Water-soluble sacrificial layer enables ultra low-cost loc integration of magnetic resonance microcoils with 100% filling factor*, Solid-State Sensors, Actuators and Microsystems Conference (TRANSDUCERS), 17th International, Barcelona, Spain, 2013.

[RK23] **R. Kamberger**, O.G. Gruschke, J. Hoefflin, J.G. Korvink; *Hollow Solenoidal Microcoils for Plug-and-Play Exchange of Sample Capillaries*, Experimental Nuclear Magnetic Resonance Conference, 2013, 54th ENC, Pacific Grove, CA, USA

Supervised Master's Theses

[MA2] Prateek Gogte, *Free standing solenoidal micro-coil with adjustable stiffness*, Master's Thesis, University of Freiburg, IMTEK - Laboratory of Microactuators, 2016

[MA1] Agazi Tesfai, *Cryogenically cooled detector coil for NMR*, Master's Thesis, University of Freiburg, IMTEK - Laboratory of Simulation, 2015

Acknowledgements

Now that this life chapter is coming to an end and new adventures are waiting, I want to thank a whole lot of people, which one should definitely do more often.

First I thank my PhD thesis adviser (or Doktorvater) Jan Korvink. I am really grateful for the opportunity you have given me, and your inexhaustible pool of ideas always pushed me to be curious. Thank you for creating a fruitful and cooperative atmosphere in the workgroup, that at all times is open to criticism - this is not at all the rule in every work group. And thank you for the wisdom of "don't compete, cooperate", "better ask for forgiveness than permission" and "if we don't try, we will never know".

I am truly thankful to Oliver Gruschke, who helped me tremendously throughout my whole thesis, from bouncing ideas back and forth, scientific and non-scientific discussions, hours of manufacturing and measurement sessions, and of course moral support. Over the years you have become a genuine friend to me. Thank you.

Thank you to all my collegues in the work group. Erwin, Mazin, Patrick, Jens and Dario I have enjoyed bouncing ideas (and idiotic conversations) back and forth with you, it was always (mostly) joyous. Of course this also counts for all other members of the work group (Swati, Nils, Andreas, Markus, Sebastian, Neil, Nan, Natalia, Mued, Suleman, Thorsten, and all the others that I hopefully have not forgotten).

Thank you Gaby. To me, you are the soul of Imtek, since you followed me through the workgroups! I loved all idiotic and sincere discussions we have had.

I also want to thank my master students, Agazi and Prateek. It was a lot of fun to guide you through your theses, and I hope I was able to teach you at least some things.

Through my studies and student jobs I also have a special bond to the Microactuators lab. Roland, Moritz, Mikel and Angi, thank you for all the fun through the years, I always enjoyed coming to your lab. Of course, also thank you Ulrike Wallrabe, for letting me into you lab, and always supporting my work.

Another special thank you goes to Katharina and Johannes, my MAGRITE colleagues. I really enjoyed working with you, through all the hours of measurements at the MR scanner, all the little and extensive explanatory session on MR and Neurobiology, and the BrainLinks meeting and talks we went through together.

I also want to thank a whole bunch of people of the Medical Physics group at the University hospital. Jochen, Pierre, Dominik, Moritz and Annette thank you for various hours of MR measurements, MR support and explanations! I have also enjoyed working with Michael and Sebastian, especially on 3D printing related projects.

Through the BrainLinks-BrainTools cluster, I have endured days of scientific and soft-skill talks and courses. These courses, and the obligatory beers that came with them,